



LUT University
LUT School of Energy Systems
Energy Technology

Development and application of a one-dimensional model for entrained flow calcium looping process

Work supervisor: D.Sc. (Tech.) Jouni Ritvanen
Work inspector: D.Sc. (Tech.) Kari Myöhänen
Lappeenranta 02.09.2019
Georgios Sakas

Abstract

LUT University
LUT School of Energy Systems
Energy Technology

Georgios Sakas

Development and application of a one-dimensional model for entrained flow calcium looping process.

Master's Thesis
2019
102 pages, 59 figures, 11 tables and 0 appendices.

Examiners: D.Sc. (Tech.) Jouni Ritvanen
D.Sc. (Tech.) Kari Myöhänen

Keywords: Entrained flow reactor, carbonator, calciner, oxyfuel, pneumatic transport.

The utilization of fossil fuels like coal, oil and gas for power production has steadily increased the amount of CO₂ in the Earth's atmosphere, with negative consequences in the climate. Thus, the scientific community indicated the importance of developing efficient carbon capture systems (CCS). In addition, the second-generation CCS of calcium looping process (CaL), through the years has been proven efficient enough and worth for further studies.

The objective of this report aims in developing an entrained flow 1D-Model for the CaL, where the reactors are interconnected to each other, with dynamic balance exchange of solids flow, and further utilization of it in the cement production line.

The work resulted to successful simulation of the pneumatic conveying for fully entrained flow with accurate gas and mass concentration profiles across the length of the reactors. In addition, potential air leak in the end of the carbonator indicated slight reduction of the total temperature in the reactor and decline of the overall CO₂ capture efficiency. Added, the choking velocity values predicted were reasonable and proved the safe operation of the system under the pneumatic transport regime. Furthermore, the maximum sorbent capacity and solid internal recirculation of the material back in the carbonator proved to have a sensitive role regarding the efficiency of the CaL process.

This work was done in LUT University as part of the CLEANER project.

Acknowledgements

This work was carried out in LUT University as a part of the CLEAN clinKER production by calcium looping (CLEANKER) project. This project has received funding from the European Union's Horizon 2020 research and innovation programme under grant agreement No 764816.

I wish to express my sincere gratitude to my supervisor D.Sc. (Tech.) Jouni Ritvanen, who was there every time I needed guidance regarding any technical issues with the model.

I sincerely thank D.Sc. (Tech.) Kari Myöhänen for his excellent feedback regarding the theoretical background of the CaL process and the CLEANKER project.

I also thank M.Sc. (Tech.) Antti Pitkaoja for his tips and guidance on how to effectively carry out my research plan during the five months of working together in the same office.

Table of Contents

1	INTRODUCTION.....	6
2	CALCIUM LOOPING PROCESS	8
2.1	Calcium Looping Process Approach.....	8
2.1.1	Carbonator.....	9
2.1.2	Calciner	12
2.2	Raw Material Behavior in CaL	14
2.3	Second Generation CCS cases	16
2.3.1	Second-Generation Post-combustion Processes.....	16
2.3.2	Second Generation Oxyfuel Processes.....	17
2.3.3	Second-Generation Pre-combustion Processes	18
2.3.4	Comparison of Second-Generation Processes with CaL.....	18
3	FLUIDIZATION THEORY.....	20
3.1	Introduction to Fluidization.....	20
3.2	Regime Mapping	21
3.3	Fast Fluidization.....	22
3.3.1	Alteration to Fast Fluidization.....	24
3.3.2	Vertical Density Profile at Fast Fluidization	24
3.3.3	Slip Velocity at Fast Fluidization	26
3.4	Pneumatic Transport Regime	27
3.4.1	Particle Distribution in Pneumatic Vertical Conveying	28
3.4.2	Slip Velocity in Pneumatic Transport	29
3.4.3	Choking and Entrainment: Choking Classification.....	32
3.4.4	Choking and Entrainment: Determine Choking Velocity	34
3.4.5	Density Profile at Pneumatic Transport	36
4.	CURRENT STATE OF CALCIUM LOOPING MODELLING	37
4.1	CaL Model by Shimizu et al. (1999).....	38
4.2	CaL Model by Alonso et al. (2009).....	40
4.3	CaL Model by Romano(2012).	42
4.4	CaL Model by Jaakko Ylätalo et al. (2012-2014)	45
4.4.1	Article Published on 1D CaL Model, by J. Ylätalo et al. (2012)	45
4.4.2	Article Published for the Oxy Combustion Calciner Model, by J. Ylätalo et. al. (2013).....	47
4.4.3	Article Published for a Model-based Scale-up Study of the CaL by J. Ylätalo et. al. (2014)	50

4.4	CaL Model by Spinelli et al. (2018).....	51
4.5	Acknowledgements Upon Current State of CaL Modelling	54
5.	DESCRIPTION OF THE ONE-DIMENSIONAL MODEL FOR ENTRAINED FLOW CALCIUM LOOPING PROCESS	55
5.1	CLEANER Process Description.....	55
5.2	Overall Model Framework	58
5.3	Discretization of Reactor Model	59
5.4	Mass Balance	60
5.5	Gas Mass Balance	62
5.6	Energy Balance	64
5.7	Combustion – Gasification.....	64
5.8	Sorbent reactions	66
5.9	Boundary Conditions.....	68
6.	CALCULATIONS.....	70
6.1	Model Verification	70
6.2	1D Model Results.....	73
6.2.1	Temperature Profile.....	74
6.2.2	Solids Concentration Profile	75
6.2.3	Carbonation-Calcination Reactions Rate	77
6.2.4	Fluidizing Gas Velocity	79
6.2.5	Solids (CaCO ₃ , CaO) Profile.....	82
6.2.6	Flue Gas Profiles (CO ₂ , O ₂ , H ₂ O, N ₂).....	84
6.3	Sensitive Analysis in Kinetic Coefficient of Carbonation.	85
6.4	Pilot Plant Operation with Air Leakage and without	87
6.4.1	Temperature Differences.....	87
6.4.2	CO ₂ Capture Efficiency.....	88
6.5	Choking Velocity	89
6.6	Comparison Between the Four Different Cases.	93
7.	DISCUSSION	95
8.	CONCLUSION.....	97
	REFERENCES.....	98

Nomenclature

Ar	Archimedes number	[$-$]
a	empirical coefficient	[$-$]
b	empirical coefficient	[$-$]
c	empirical coefficient	[$-$]
d	empirical coefficient	[$-$]
A	cross sectional area	[m^2]
C	molar concentration	[mol/m^3]
F	fraction	[$-$]
E	efficiency	[$-$]
G	mass flux	[$\text{kg}/\text{m}^2\text{s}$]
H	Enthalpy	[J/kg]
k	kinetic coefficient	[$1/\text{s}$]
M	molar mass	[kg/mol]
m	mass	[kg]
N	number of cycles	[$-$]
p_∞	atmospheric pressure	[Pa]
p	pressure	[Pa]
q	heat flux	[W]
q_m	mass flow	[kg/s]
r	reaction rate	[$\text{mol}/(\text{m}^3\text{s})$]
S	available surface area for reaction	[m^2]
T	temperature	[$^\circ\text{C}$]
u	velocity	[m/s]
u_s	slip velocity	[m/s]
u_t	terminal velocity	[m/s]
u_{ch}	choking velocity	[m/s]
V	volume	[m^3]
W	mass fraction	[$-$]

X_{max}	sorbent capacity	[$-$]
X	conversion degree	[$-$]

Subscripts

av	average
c	reactor core
$calc$	calcination
$carb$	carbonation
$conv$	convective flow
$chem$	chemical
dp	particle mean diameter
$desu$	desulphation
dir	direct sulphation
$disp$	dispersion
eq	equilibrium
g	gas
in	inlet
max	maximum
out	outlet
r	residual
s	solid
$sulf$	indirect sulphation
tot	total
vol	volatile
wgs	water-gas shift
wl	wall layer

Greek Letters

Δ	difference
ε	voidage fraction

ρ	density	[kg/m ³]
η	efficiency	[-]
ψ	structural parameter	[-]
Σ	sum	

Abbreviations

1D	one-dimensional
3D	three-dimensional
ASU	air separation unit
BFB	bubbling fluidized bed
CaL	calcium looping process
CFB	circulating fluidized bed
CCS	carbon capture storage
CV	control volume
CFD	computational fluid dynamics
LHV	lower heating value
NO _x	nitrogen oxide species
ODE	ordinary differential equation
PCFB	pressurized circulating fluidized bed
SO _x	sulfur oxide species
TGA	thermogravimetric analyzer
TDH	transport disengaging height

1 INTRODUCTION

The effects and impacts of the carbon dioxide growth on the earth's atmosphere are well known in the scientific community nearly 100 years. Various researchers through the years reported the importance of carbon dioxide accumulation in the atmosphere and how sensitive is the global temperature in the transition of it. The anthropogenic emissions the last 50 years, especially after the introduction of fossil fuel as the main driver of electricity production, are abruptly increasing while shocking and stressing the climate of the earth. In 2015, the Paris agreement was signed by 195 countries, all contributing to gradual decrease of CO₂ emissions until 2025. Power production contributes in a large extent on the problem. Cutting down emissions from power plants indicated as important contributor. Reduction of CO₂ emissions from fossil fuel power plants and especially coal-fired, was pointed out as one of the main indicators to achieve the European Union's goal.

Carbon capture and storage technologies (CCS) are considered as one of the most realistic and practical choices to balance the CO₂ levels in the atmosphere (Zheng, 2011,1). CCS are defined as the energy systems where carbon dioxide is removed from emission gases, transported and stored in remote areas from the atmosphere, like the deep sea or underground. The United Nations Intergovernmental Panel on Climate Change (IPCC) indicated that CCS has the prospective to lower the economic stress of the transition into clean coal technology and the flexibility to achieve high numbers of CO₂ reduction (IPCC, 2005).

Three major CCS technologies are identified and extended into industrial scale level, post-combustion, pre-combustion and oxyfuel-combustion. In the post-combustion capture, chemical solvents like amine or ammonia are cleansing the resulting CO₂ out of the combusted flue gas, a process similar to SO_x and NO_x treatment. Post-combustion's flexibility and adaption into existing plant, by adding unit operations, makes it a very attractive option. For the pre-combustion capture, solid fuel is gasified with oxygen to produce a flue gas consisting mainly of carbon monoxide and water vapor, this will activate the water-gas loop reaction and in consequence creation of hydrogen (H₂) and CO₂. Physical sorbents will then capture the resulting CO₂. Lastly, oxyfuel-combustion, where pure oxygen utilization for fuel combustion is implemented, to achieve rich CO₂

flue gas. The rich gas is already practicable for transport and storage, after water condensation and impurities clean up.

Technical and economic challenges associated with the three technologies identified above, led to construction of second-generation capture technologies. Solid looping technologies like calcium or chemical looping are currently leading the process. Calcium looping process is a post-combustion capture procedure with abate economical expenses for oxygen separation in oxy-fuel combustion systems, associated with the air separation unit (ASU). Calcium looping consists of two fluidized beds linked and co-operating together through loops to capture CO₂ with lime. The process requires a much smaller ASU system, which makes it less expensive and attractive option, with the use of flue gas produced from an existing plant like cement industries.

Practical and feasible experiments upon calcium looping process requires economical capability of constructing an interconnected fluidized bed system. The economical point of view is challenging and limiting the prototypes research. Currently, modelling is a valuable source and tool to optimize and analyze complicated operational modes. The capability of today's energy systems modelling is accelerating the technology research, as it can serve as a decent prototype figure. One to three dimensional complex models can be built to analyze the dynamic operation and efficiency of a system like calcium looping process and decrease the need of prototype manufacture.

The proposed thesis aims at the development of a 1D case model for the CLEANER-process. The model is clarified to have interconnected calciner and carbonator reactors, exchanging solids in balance. Furthermore, the specific process/project intention is to develop a carbon capture system for the cement production line, which is based on a calcium looping process. In addition, the developed model will further be implemented and applied in the Vernasca pilot studies. Concluding, the main study from the specific 1D model is to provide accurate CO₂, CaCO₃ and CaO concentration profiles across the length of the reactors and determine whether or not the pneumatic transport regime is maintained by calculating the choking accumulation type 'A' velocity.

2 CALCIUM LOOPING PROCESS

2.1 Calcium Looping Process Approach

The concept of capturing CO₂ by utilizing lime in CCS system was recently introduced and researches initiated after the increasing need of developing more efficient carbon capture technologies. Shimizu et al. (1999) first introduced the post-combustion looping. This process can exploit a twin fluidized bed system through carbonation-calcination looping to capture carbon dioxide and sulphur dioxide from a stationary flue gas source like cement plants. As shown in Figure 2.1 adapted from J.M. Valverde (2013), flue gas from fixed source is introduced in the carbonator at 600 degrees Celsius. The CO₂ is captured inside the carbonator, by spatial carbonation (CaO+CO₂→CaCO₃) and fast kinetic reactions in short residence time. The diffused calcium carbonate solids are then transported into a second fluidized bed calciner, where in more than 900 degrees Celsius the calcination reaction (CaCO₃→CaO+CO₂) is proceeding, releasing a highly rich in CO₂ flue gas, which can then be sequestered (transport and store of carbon dioxide). The required heat for the calcination reaction is achieved by burning fuel in the calciner under enriched in oxygen air flow, in order to avoid CO₂ dilution and produce pure carbon dioxide flue gas. The heat difference between the reactors is achieved by external heat exchangers, attached in the loop seal.

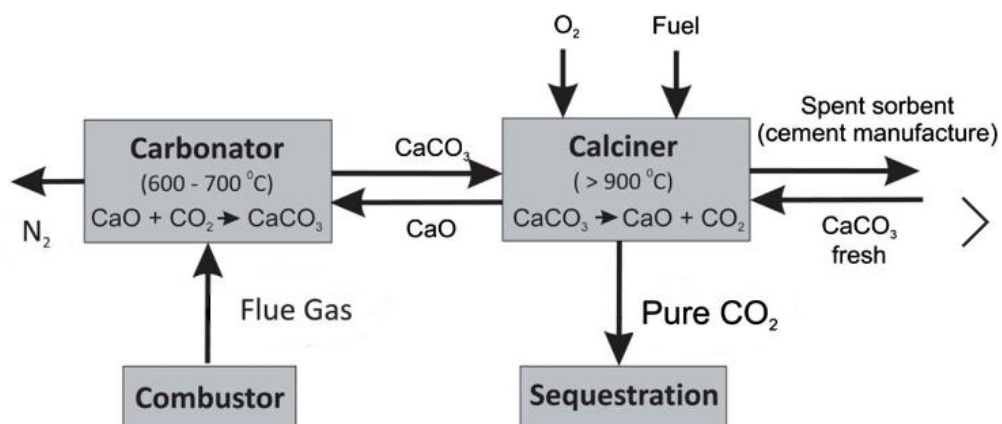
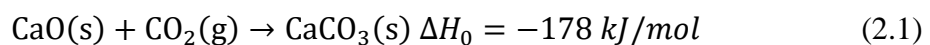


Figure 2.1. General CaL process, adapted from J.M. Valverde (2013).

The production of oxygen through ASU is crucial because of the economical expenses associated with it in the oxy-combustion process. The post-combustion looping process from fixed source can reduce the amount of oxygen needed. The exothermic heat produced in carbonation reaction is enough to almost counter and balance the power generation from a combustor. However, the additional limestone flows and construction units are added to the overall cost and accordingly the economic expectation is balanced with the oxy-combustion unit. Therefore, the calcium looping process is only more efficient when retrofitted to a static flue gas source like cement kilns.

2.1.1 Carbonator

The carbonator reactor captures CO₂ utilizing the exothermic carbonation reaction, as shown in Equation 2.1. Shimizu et al. (1999) proposed fluidized beds as effective carbonator reactors due to their ability to handle high solid inventory with good solid-gas contact. Entrainment flow in high superficial gas velocity allows decent individual contact and reaction between gas and solid. In the framework of this thesis, gooseneck circulating fluidized bed (CFB) type operating in entrainment flow and pneumatic transport line is employed. Spinelli et al. (2018) with their work on calcium looping process and specifically on CO₂ capture efficiency in the carbonator, stated that high efficiencies can be yield in gooseneck type carbonator for industrial scale (length up to 140m pipe), by proper combination of sorbent capacity (X_{max}) and solid to gas ratio, which are the most important criteria for the carbonator efficiency. The fluid dynamic analysis to verify the flow stability in the gooseneck type reactor is done in this work. Below, in Figure 2.2 a general layout of a circulated fluidized carbonator for further discussion of the purpose of carbonator reactor, and the exothermic, heterogenous carbonation reaction are being demonstrated.



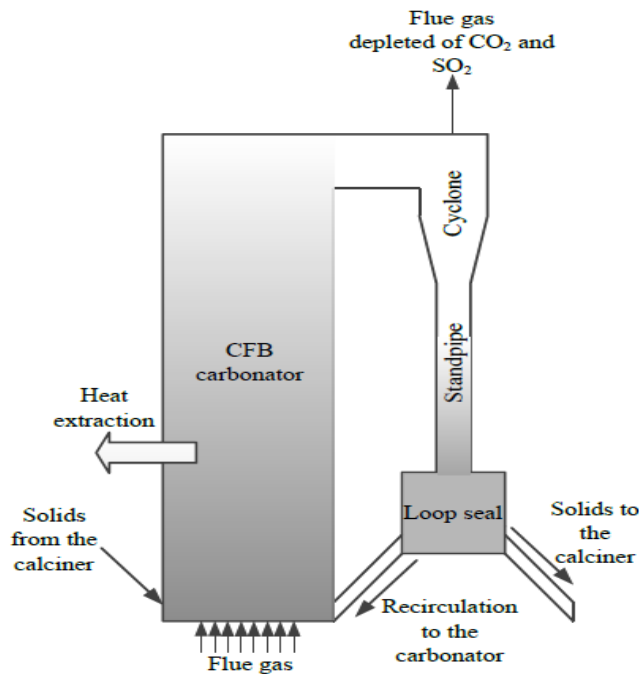


Figure 2.2. The blueprint of a general CFB carbonator reactor, adapted from Ylätalo J. (2013, 19)

Solids from calciner, recirculated solids from carbonator and flue gas from a static source (Cement kiln) are mixed and fed in the carbonator inlet. The carbonation reaction (Equation 2.1) takes place inside the reactor riser at approximately 650 degrees Celsius based on the equilibrium curve of carbonation-calcination adapted from Silcox et al. (1989). The reaction will release heat to the vessel due to the exothermic process. The heat must be continuously removed from the system, to maintain an equivalent temperature fitting the equilibrium curve, shown in Figure 2.3. The solids after the carbonation will be transported into the cyclones, where gas-solid separation is occurring. The remaining solids are volumetrically separated in the loop seal and distributed into recirculated solids for enhanced thermodynamic efficiency, and into solids that are transferred through the loop seals in the calciner for the next reaction loop. In addition, the remaining flue gas which consists of poor concentration of SO_2 and CO_2 and can be further filtered and disposed in the atmosphere.

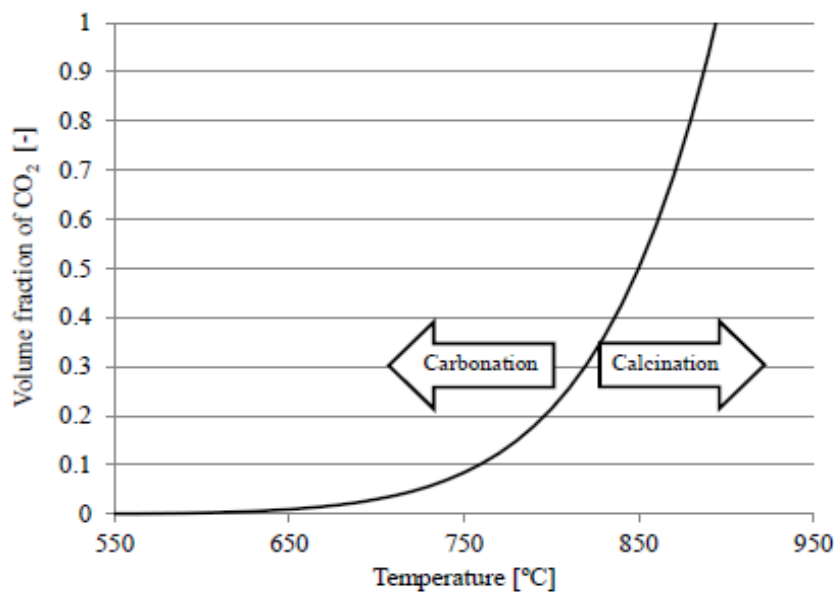


Figure 2.3. The equilibrium curve of carbonation-calcination from Silcox et al. (1989), adapted from Ylätalo (2013, 20)

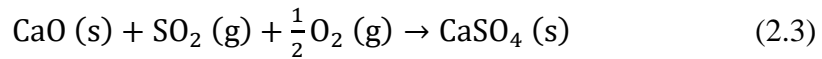
The proper selection of the inlet temperature is done by counterbalancing reaction equilibrium and reaction kinetics. Reaction kinetics are more dynamic in higher temperatures, although the reaction equilibrium of carbonation is being favored in temperature below 750 °C. As observed from the Figure 2.3, a reaction temperature of 690 °C can yield approximately 95% efficiency in capturing CO₂ inside the carbonator, or an equivalent 5 vol-% of concentration in CO₂. The max theoretically concentration formed from the equilibrium curve (Figure 2.3) is at about 1% and temperature of 650 °C. This means that the lime in the carbonator will absorb the 99% of the upcoming carbon dioxide. The schematic reaction map demonstrated above, was created as a function of Equation 2.2 proposed by Silcox et al. (1989).

$$\frac{p_{eq,CO_2}}{p_\infty} = 4.137 \cdot 10^7 \cdot e^{-\frac{20747}{T^*}} \quad (2.2)$$

Where p_∞ is atmospheric pressure [Pa], T^* ambient absolute temperature in Kelvins and p_{eq,CO_2} is the equilibrium partial pressure of CO₂ in [Pa].

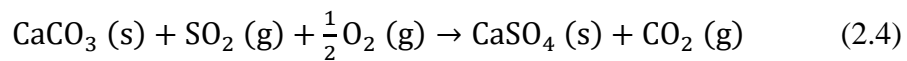
The carbonator, added to carbon dioxide capture, will as well desulphurize the flue gas from sulphur dioxide. Sanchez-Biezma et al., (2013) with their experiment in a 1.7 MWt pilot facility stated that the calcium looping process can yield up to 95% efficiency in capturing SO₂ under normal operating conditions. The reactions occurring to achieve sulphur capturing are not 100% clear, as the procedure gets too complex after some point, from the continuously loop reactions inside the reactor. However, the majority of these reactions inside a calcium looping process is done by sulphation, as shown in Equation 2.3. In addition, direct sulphation (Equation 2.4) could contribute, however is yet unclear for the process of calcium looping.

Sulphation:



$$\Delta H_0 = -502.1 \frac{\text{kJ}}{\text{mol}}$$

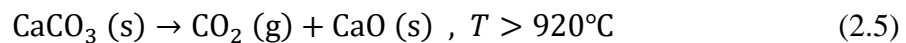
Direct Sulphation:



$$\Delta H_0 = -323.8 \frac{\text{kJ}}{\text{mol}}$$

2.1.2 Calciner

The calcination reaction, shown in Equation 2.5, is mainly occurring in temperature range of 920°C - 950°C, to fit the equilibrium curve demonstrated and adapted from Silcox et al. (1989).



The motivation upon calcination is to achieve high concentrated CO₂ flue gas for further transport and storage (sequestration). Upcoming CaCO₃ from carbonator, is calcined in high temperatures to produce solids of CaO and rich gas of CO₂. The resulting flue gas can either be rich carbon dioxide or mixture of H₂O and CO₂. The calcination high temperatures are achieved by burning fossil fuel (coal, heavy oil) in oxyfuel-combustion process. The selected oxy-fuel combustion can produce high CO₂ concentrated flue gas mixture with high concentration in water. The hydrogen concentration typically at 10% inside a fossil fuel from proximate analysis is reacting with O₂ to produce the high concentration in H₂O. Although, the resulting water does not serve as significant problem due to efficient ability of condensation after the calciner reactor. A volume percentage of the rich in carbon dioxide flue gas, recirculates in the calciner, mixed with the oxidant. The mixture first serves as a control method of the oxygen concentration at reasonable level and secondary as preheating of the oxidant before entering the calciner, for further thermodynamic efficiency increase. A typical blueprint of a CFB calciner reactor in calcium looping process is adapted from Ylätalo (2013), to schematically support the theory and explanation mentioned in the paragraph.

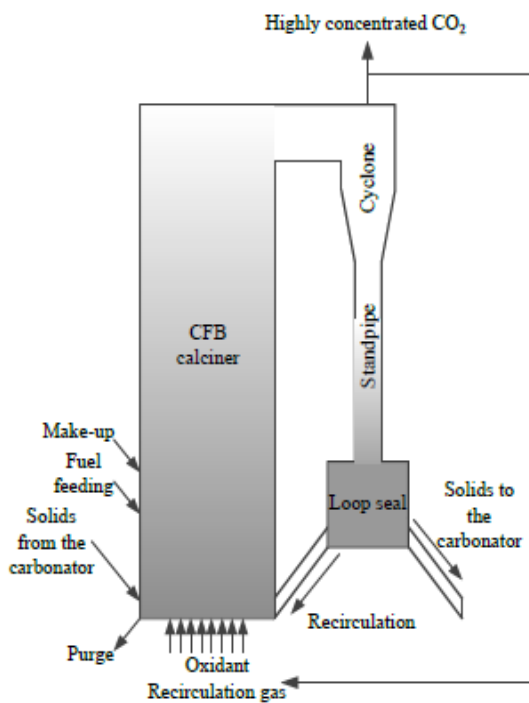


Figure 2.4. Typical Blueprint of CFB reactor in calcium looping process, adapted from Ylätalo (2013, 22)

In a typical CFB calciner layout for calcium looping process, sorbent (lime) make-up continuous introduction and purging of it, is on the main importance. Sintering and deactivation of the particles, caused by calcination-carbonation loops, results in decreasing capture efficiencies. The phenomenon of sintering and calcination-carbonation loops are explained in next chapter.

2.2 Raw Material Behavior in CaL

The physical and chemical properties of the raw material (lime) are exhibiting drastic changes under the periodic carbonation and calcination loop. Ylätalo (2013) after reviewing various researchers, stated that the general understanding is that the lime is losing the ability to capture CO₂ after each calcination step. The porous structure of the lime particle is sintering every time the particle undergoes one high temperature calcination step. In addition, the carbonation reaction will alternate from fast dynamically controlled reaction into a diffusive, which will affect the whole efficiency of the post-combustion capture.

Grasa and Abanades (2006), with their experiment done in a thermogravimetric analyzer (TGA) constructed for long periodic cycles of calcination-carbonation, stated and proved for a various range of different types of limestone (dolomite, Gotland limestone, limestone), that the activity and ability of the limestone to capture carbon dioxide will decay even from the first loop. A semiempirical correlation characterizing decay in activity was assembled by Grasa and Abanades. Adapting Wang and Anthony's (2005) Equation 2.6, formulated a new proper correlation for long cycled particles, Equation 2.7, which was used to derive the sorbent capture capacity in number of cycles, as shown in Figure 2.5.

$$X_N = \frac{1}{1 + kN} \quad (2.6)$$

$$X_N = \frac{1}{\frac{1}{1 - X_r} + kN} + X_r \quad (2.7)$$

Where k represents the deactivation constant [-], X_r the residual activity in molar fractions and N the number of cycles.

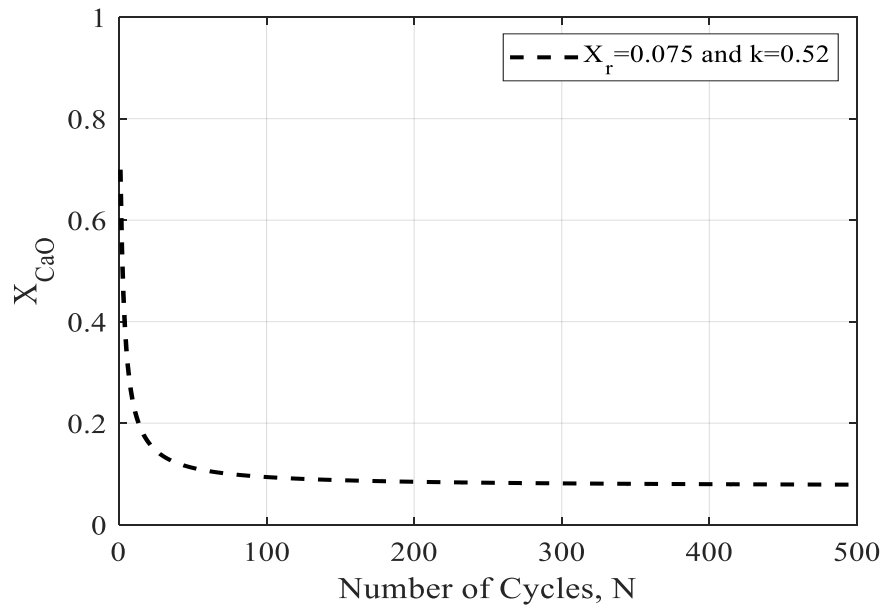


Figure 2.5. Sorbent Conversion decay vs number of cycles

Grasa and Abanades after comparison of their experiments with simulation results using Equation 2.7, stated that there is a decent agreement between the outcomes from the two sources when deactivation constant is equal to $k=0.52$ and residual activity $X_r=0.075$. From Figure 2.5, abrupt decay of the carrying capacity of solids is observed in the first 20 cycles, and stabilization of it at around 0.1 after 50 cycles. Ylätalo (2013), stated that in the first cycle, 1 mole of calcium oxide is needed to capture one mole of carbon dioxide, after 20 cycles that 1 mole of CO₂ requires 10 moles of CaO to be captured. Pfeifer (2013), affirmed that the decay in reactivity is caused by three major phenomena. Decline of the active surface area, undesired sulphation reactions and formation of calcium hydroxide (Ca(OH)₂), and casualty of material during fragmentation of particles.

2.3 Second Generation CCS cases

The high efficiency of the three major first generation carbon capture technologies, but deficiency on commercializing the technologies mainly due to economic disability, motivated companies, governments and researchers to look for alternative advanced options. Second generation CCS technologies innovation of post-combustion, pre-combustion and oxyfuel-combustion processes were initiated to compensate the disadvantages.

2.3.1 Second-Generation Post-combustion Processes

Carbonate looping technique and use of membrane processes are recently qualified for decent technological innovations regarding the post combustion carbon capture. The use of membrane to capture CO₂/N₂ is gaining popularity as the calcium looping process struggles to obtain commercialization due to expensive material utilization, extensive waste disposal tariff and high operational energy demand (Zhao L., 2009). On the other hand, use of membrane on its own does not yield the desirable carbon capture ratio of 95% for further sequestration.

Membrane Technology and Research, Inc. (MTR), acknowledging that the technology's carbon capture efficiency is relatively low. They launched a hybrid capture system as shown in Figure 2.6. The system consists of two rational membranes. The first one separates the upcoming flue gas from carbon dioxide for sequestration purposes. Continuously the next membrane serves as CO₂ recirculation to increase the purity of it inside the boiler. The whole process aims in reducing operational costs, material costs and energy consumption compared to leading calcium looping process.

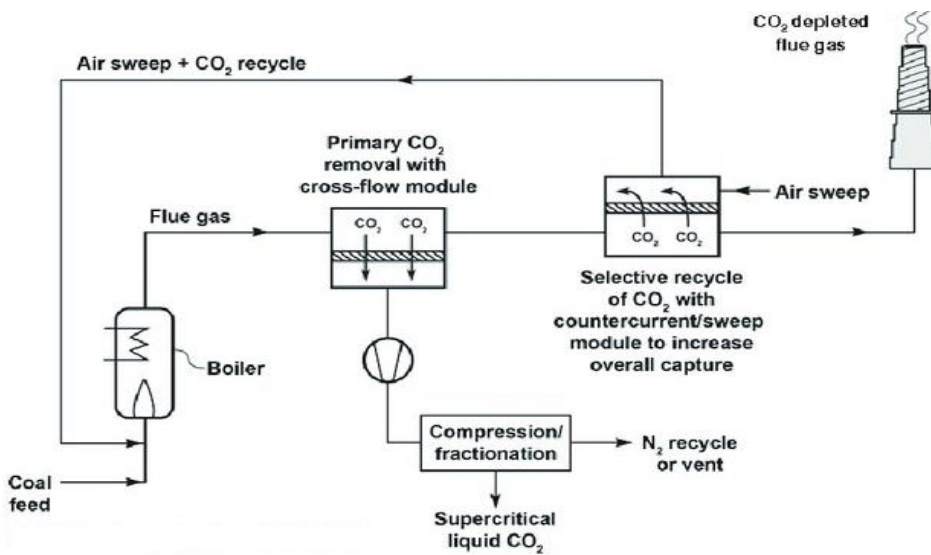


Figure 2.6. All membrane post combustion CO₂ capture process, adapted from Freeman B. (2014)

2.3.2 Second Generation Oxyfuel Processes

Chemical looping is considered as the prevail technology for second generation oxyfuel process. The technology itself and energy systems utilization are similar to calcium looping process. Two fluidized beds are cooperating for carbon capture storage. As shown in Figure 2.7 a combustion reactor separates the metal oxide from the oxygen, with endothermic reactions. In consequence the reduced metal oxide, regenerates at a second reactor, with treatment of exothermic reactions and utilization of atmospheric oxygen to produce a heat flow of 1200 °C. The heat flow is further used to generate heat. Although the process has several benefits similar to CaL, researchers struggle to achieve decent reactivity of the metal oxide while undergoing the looping process. (Markewitz P., 2014)

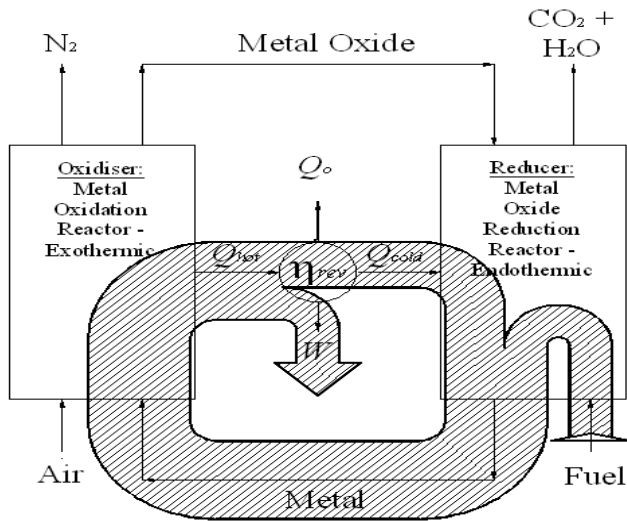


Figure 2.7. Sankey diagram of energy fluxes in a Chemical looping process.

2.3.3 Second-Generation Pre-combustion Processes

In a pre-combustion carbon capture, coal or other alternatives are partially oxidized in high temperature and high pressure of approximately 30 bar to produce a raw gas of CO, H₂, CO₂, increasing the carbon dioxide concentration for further sequestration. Due to positive pressure conditions, membranes could be utilized in the cases as a next generation pre-combustion, supplanting the natural scrubbing in the long term. Scherer and Franz (2011), stated that H₂ or CO₂-selective membranes exploit can yield less percentage efficiency loss compared to physical scrubbing. However, membrane types are under research and development state, upon their selectivity, permeability and stability, making them hard to utilize at the current carbon capture technological features.

2.3.4 Comparison of Second-Generation Processes with CaL

The economic consequences of removing the carbon dioxide from the atmosphere is becoming obvious. Each one of the carbon capture technologies will yield expenses in heat, power and operational costs of the power plant. Political laws and government tariffs are to determine which carbon capture technology will prevail in the future.

Applying a CCS system in a power plant mainly resolute from the existing physical case of the plant and infrastructure.

The post-combustion calcium looping process has several advantages compared to other second-generation technologies. Utilization of limestone, circulating fluidized beds and oxy-combustion are familiar terms in the energy sector, which makes them easy to handle and process. In addition, as the knowledge upon the technology is spread, future problems associated with it, can be avoided. A second advantage is that the natural limestone is considered as an abundant resource, makes it a cheap and suitable sorbent. In consequence, the utilization of natural limestone for carbon capture allows the synergy with other energy systems like cement kilns.

On the other hand, post-combustion calcium looping process is associated with high investments costs. The construction cost of a twin fluidized bed is equal to a conventional power plant, which puts pressure on governmental contribution and financing. The unit will require continuous limestone flow, which in consequence demands a new and decent logistics plan. Concluding, fragmentation phenomenon of the particles is not yet well researched and its consequence in the thermal design and control of solid circulation are currently doubtful. (Ylätalo, 2013)

3 FLUIDIZATION THEORY

The motivation upon this chapter is to describe the general and detailed knowledge used in the entrainment flow frame model developed for this work. The chapter starts with an overview of fluidization theory (chapter 3.1), and furthermore fluidization specific regimes are described (3.2). Continuously, in chapters 3.3 and 3.4 detailed theory analysis about the assumptions taken for this work is being done. On the main interest are slip velocity and its relation to terminal, vertical density profile and choking in high velocity fluidization.

Fritz Winkler in 1921 invented the fluidization phenomenon. However, the idea to promote and develop the process to produce hot gas steam, by combusting coal, it was first introduced in 1960 by Douglas Elliot.

Fluidized beds can mainly be classified into three main categories, bubbling fluidized beds (BFB), circulating fluidized beds (CFB) and pressurized circulating fluidized beds (PCFB). This chapter will mainly focus on CFB regimes of fast fluidization and pneumatic transport.

3.1 Introduction to Fluidization

The phenomenon of fluidization is described as the operation where the solid particles are behaving liquidlike through suspension in gas (Kunii and Levenspiel, 1991). While the particles are exposed to this condition, their gravitational pull is being countered by the gas drag force, which will make them suspend in air or even move upwards (entrainment) in high enough superficial gas velocities (Basu, 1991). This phenomenon has some unique features which are diverging for different gas/solid velocities or solids feed in varying energy systems. The general unique energy processes that can be characterized from fluidization are the so-called fluidized beds and their regimes. These regimes can be categorized into captive stage regimes (fixed, bubbling, slugging, turbulent), where there is no mitigation or circulation of solids outside of the vessel, and secondly into transport stage regimes (fast fluidization, pneumatic transport) where the

solids are mitigating out of the vessel due to high superficial gas velocities with respect in solid ratio feed.

3.2 Regime Mapping

The fluidizing regimes phenomena elevate from lower superficial gas velocities where the terminal velocity or, the maximum velocity an individual particle can obtain in falling due to gravitational pull, is high enough to hold the particles in a dense bottom phase, without any carryover of particles, as shown in Figure 3.1, which signifies the fixed bed. Furthermore, as the gas velocity reaches the minimum fluidization velocity point, a vigorous vibration and movement of finer solids is occurring due to higher drag friction between the gas and particles, classifying the transition from fixed bed to moving bed regime or smooth fluidization. For Group D particles of Geldart classification, bubbles start to form as minimum fluidization velocity is introduced, as for finer Group A particles, bubbles are initiating at higher gas velocities known as minimum bubbling velocity (Basu 1991, Kunii and Levenspiel 1991, D. Geldart 1986)

At higher fluidization velocities or increased bed height, depending on the cross section of the bed, slugging may occur. Geldart 1986, stated that if the maximum bubble diameter is greater than 0.6 times the diameter of the bed, slugging formation in the bed can be stable. However, slugging is a rare phenomenon in conventional fluidized beds, because the diameter or the corresponding perimeter of the beds is just too much for full slugging across the horizontal height ever happening. Although, slugging phenomenon is usually observed at many experiments from different investigators in the field, because the pilot vessel diameters are usually small enough for slugging to occur.

Furthermore, as the fluidizing velocity increases beyond the maximum bubble velocity or minimum fluidized velocity depending on the mean diameter size of the particles, the bubbles start to become more vigorous and violent until rapid break up of them is transpiring. The rapid collapse of the bubbles marks the transition from bubbling regime into turbulent. The transition is gradually happening between two velocities, where at first the bubbles at the upper section of the bed start to slowly collapse, initiating entrainment of solid agglomerates. As the velocity is further increasing the phenomena

is becoming faster and gradually moving downwards in the bed height, as shown in Figure 2.1. (Kunii and Levenspiel 1991, D. Geldart 1986, Basu and Scott A. Fraser 1991).

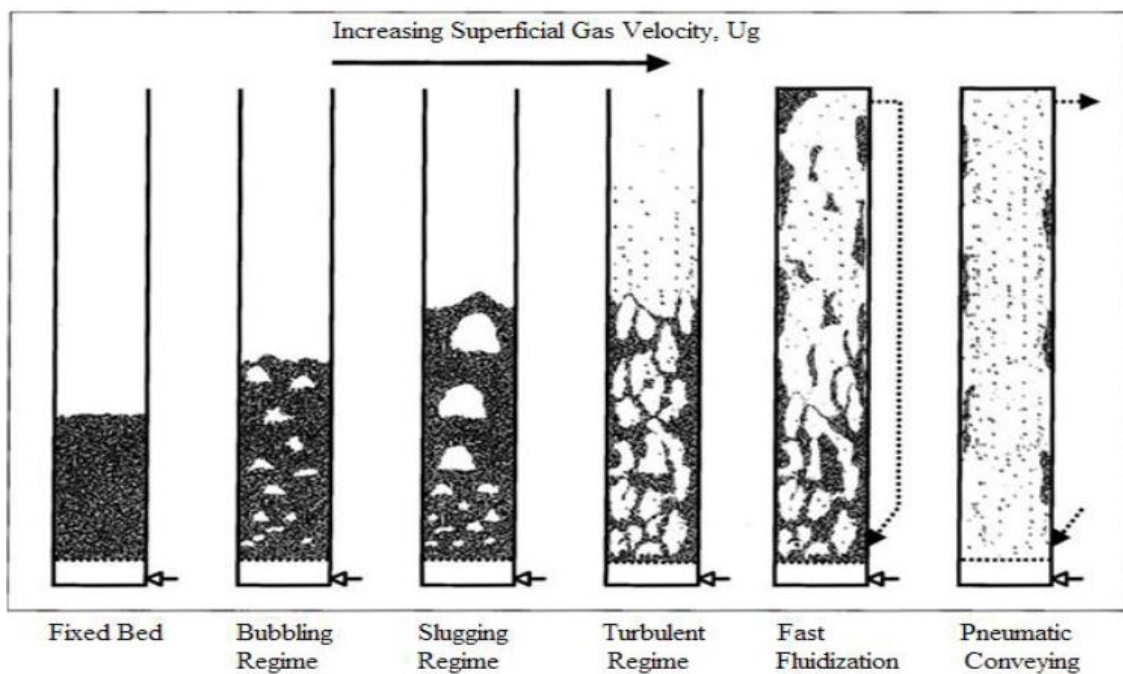


Figure 3.1. Fluidization regimes (Crowe,2006)

Fast fluidization, pneumatic conveying regimes in circulating fluidized beds (CFB), entrainment of solids and choking in high fluidization velocities are on the main interest of the research and model. A corresponding detailed analysis is performed for each one of them in the next sections.

3.3 Fast Fluidization

The definition and term of fast bed was first introduced by Yerushalmi et al, 1976. They described a regime situated between turbulent and pneumatic transport, initiated by the transport velocity. The characteristics of this regime are, first high and greater superficial gas velocity compared to the individual terminal velocity of the particles, which makes the entrained solids to move out of the height of the bed. Secondly,

suspension of clustered particles moving up and down in the height of the bed in a very dilute phase of almost 98% voidage. Individual particles are travelling in a higher speed upwards compared to already grouped particles, thus some of these individual particles that are travelling behind the grouped will eventually wake in their trail, forming bigger solid agglomerates, as shown in Figure 3.2. The regime is further characterized by diversification of suspension density in horizontal and vertical direction of the bed. Concluding, fast fluidization is not only dependent on the superficial gas velocity, but solid circulation or solid feed ratio can as well impact the regime and completely change it or even transition it into another regime.

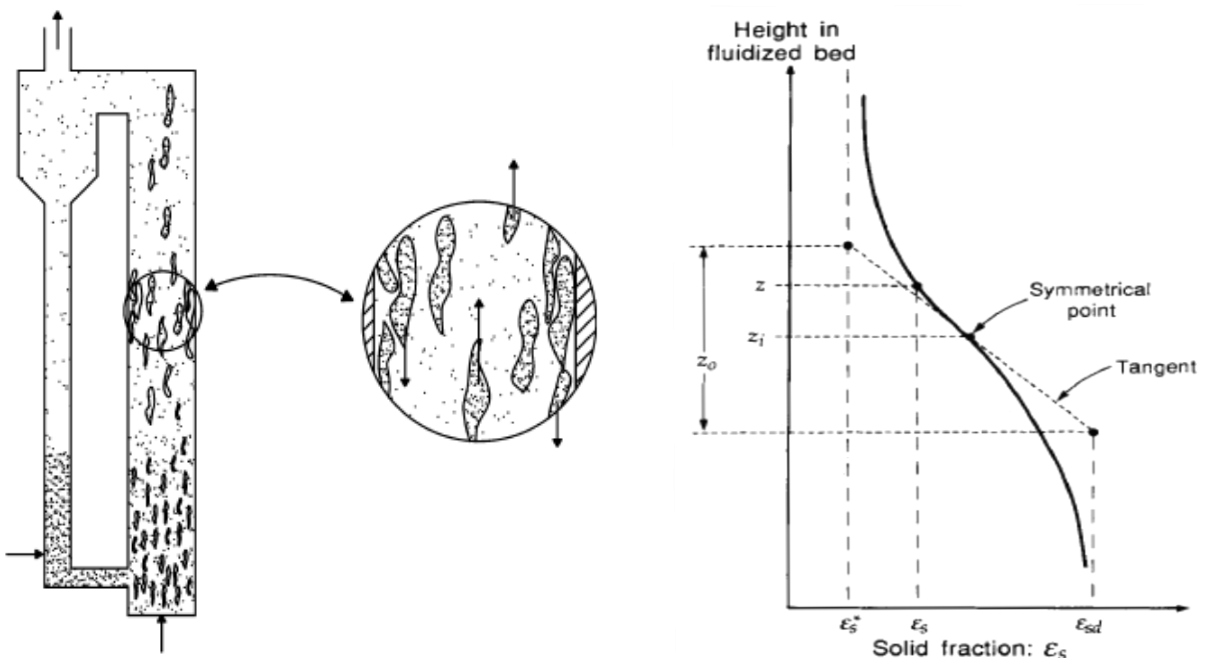


Figure 3.2: Cluster of particles moving up and down in a very dilute phase. (Basu, 1991), Li and Kwauk (1980) solid distribution curve.

In fast fluidization regime the transfer of the particles upwards in the vessel riser due to high gas velocities dragging them is very large; thus, fresh particles must be fed steadily to achieve desirable state operating conditions. In addition, a circulation system is needed in order to introduce the transferred particles again in the bottom of the bed. The circulation system is mainly consisting of cyclones separating the gas from the solids, and a downcomer transferring the solids to the bottom, as shown in Figure 2.2.

3.3.1 Alteration to Fast Fluidization

Transport velocity marks the alteration or transition from turbulent or bubbling regime into fast fluidization conditions (Geldart, 1986). When superficial gas velocity overcomes transport velocity and the solid feed is kept constant, the denser bottom phase particles are dragged upwards creating a lean phase in the upper height of the bed and a still denser one in the lower part. In this point the carryover of the particles outside of the vessel becomes sufficiently high.

However, if the solid feed ratio is not kept constant, alterations in the fast conditions will occur. When the solid feed is decreasing, the particles phase is becoming leaner across the height, particles possibility to wake and group is decreasing, and the vessel will eventually swift to pneumatic transport regime. On the other hand, if the solid feed increases, the particle phase will become denser and denser until captive stage alteration and further choking initiation, due to high accumulation of particles.

3.3.2 Vertical Density Profile at Fast Fluidization

Yerushalmi et al. (1976) with their experiment on fast fluidization regime motivated the scientific community to start investigating deeper the phenomena, and a big movement of experiments on the subject abruptly grew. Kunii and Levenspiel (1991), demonstrated an impressive collection and library of twenty-two different investigators with wide range of bed diameters, density of solid and mean particle size, all predicting an S-shape curve solid distribution across the height of the vessel, as shown in Figure 3.2. The solid volume fraction and consequently density and solid mass flux at lower part of the vessel are forming a denser phase of agglomerated particles. As the transition moves upwards in the transport disengaging height (TDH) the phase tends to diffuse. In TDH, the lighter groups or single particles are fully entrained and make it in the upper lean phase through the core of the vessel, and the heavier clusters of particles are back mixing and falling in the bottom denser phase through the walls. It is observed that in

TDH, the number of particles falling, or back mixing is gradually decreasing with height.

Although, most of fast fluidization experiments have been proven to have an S-shape voidage curve. The exact distribution and the ratio between dense and lean phases are differing for each operating mode. Kunii and Levenspiel (1991) recognized four different operating modes.

- Constant inventory of solids with changes in superficial gas velocity u_g .
- Constant mass flux of solids G_s with changes in superficial gas velocity u_g .
- Constant superficial gas velocity u_g with changes in G_s .
- Changes in both u_g and G_s .

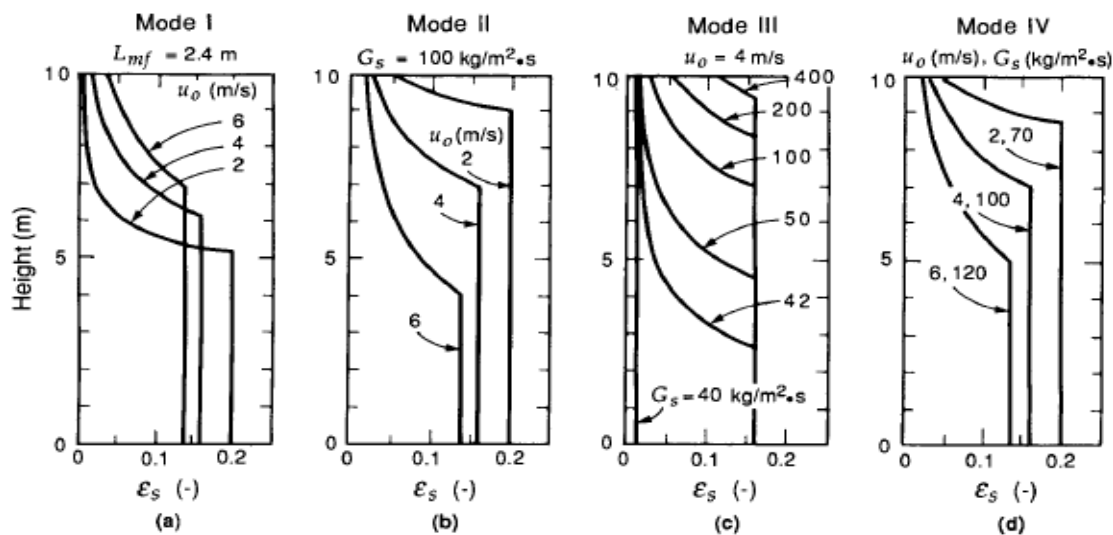


Figure 3.3. Kunii and Levenspiel (1991). Example of different distribution curves of fast fluidization in the four different operating modes. Example values: vessel diameter = 0.4 m, vessel height = 10m.

3.3.3 Slip Velocity at Fast Fluidization

(Kunii and Levenspiel 1991, D. Geldart 1986, Basu 1991). Slip velocity in a gas-solid system is defined as the difference between gas velocity and the velocity of a single particle, as shown in Figure 3.4a, which in the case is equivalent to the terminal velocity. However, when the particles cluster the slip velocity is gradually becoming greater than the terminal, as shown in Figure 3.4b. Because of particles clustering, their total weight is increasing, resulting to slower solid velocity.

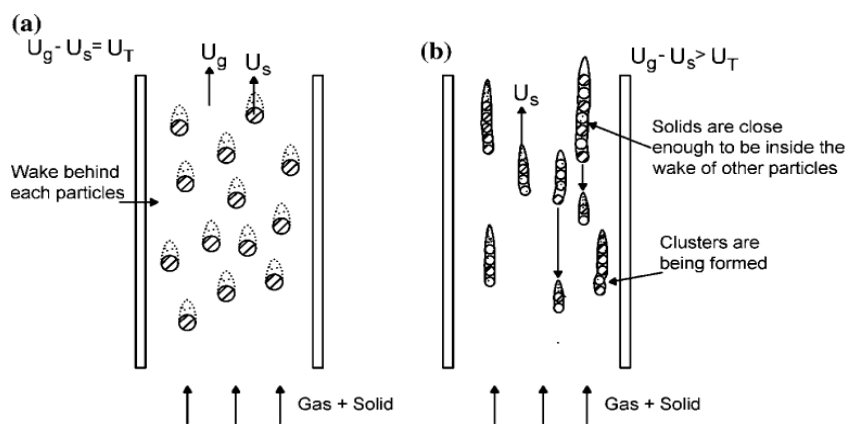


Figure 3.4. Pneumatic transport of individual particles (a), On set of Fast Fluidization and the phenomenon of particle clustering (b), and their respectively slip velocity with relation to terminal. Basu (1991).

J. Yerushalmi and A. Avidan (1978) with their detailed experiment in high-velocity fluidization observed that the slip velocity is one order of magnitude greater than the terminal in fast fluidization regime. The transition from pneumatic transport and individual particles behavior, to fast fluidization and clustering of particles in a denser phase is abruptly occurring at a limit called choking. Choking was defined as the transition from pneumatic transport to fast fluidization, with abrupt accumulation of solids and steep pressure increase. The measurement in concentration of solids was increasing logarithmically in the limit of choking. Choking and its coexistence at entrainment flow is further discussed in a next section of the Chapter 3.

3.4 Pneumatic Transport Regime

Pneumatic transport lines can simply be described as pipelines where high gas velocities are entraining or carrying over low concentration of solids. Kunii and Levenspiel (1991), defined as pneumatic transport regime, the fluidization of solids in very dilute phase, at about 99% of voidage or a representable solid-to-gas ratio less than 10 to 20. Zenz and Othmer (1956) explained in a schematic map flow the behavior of lean upflow mixtures through vertical column, as shown in Figure 3.5. Imagine a constant solid loading ratio W_1 at the bottom of the transport line, represented with line CDE. Starting from point C and gradually reducing gas velocity the frictional resistance will reduce due to increase in static head and reduction in voidage, so the system will experience pressure drop from point C to D. In the point D (On set of fast fluidization), accumulation of solids in the pipe line starts to be accountable, until further gas velocity reduction to choking velocity, where the system exhibits high and abrupt accumulation of solids in one order of magnitude according to Yerushalmi et al. (1978), resulting in abrupt steep pressure increase.

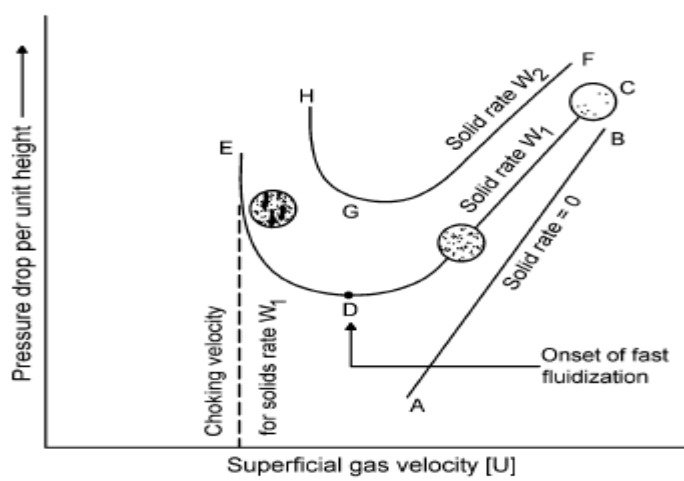


Figure 3.5. Behavior of lean phase in pneumatic transport vertical lines, adapted from Zenz and Othmer (1956)

3.4.1 Particle Distribution in Pneumatic Vertical Conveying

Various investigators through the years tried to explain and understand the particle distribution in pneumatic lines. The literature and research until now are being advanced especially after simulation introduction. However, accurate representation of particle behavior in high voidage flows is yet to be understood and results are controverting each other. How particles cluster or disperse in volume at high voidage solid-gas flows is differing for different bed experiment diameters (Ravi Sankar and Smith, 1986). The known scientific community supports that after 99% of voidage, the particles are fully dispersed in the column volume, due to sedimentation phenomenon. Other investigators like Matsen (1982) and A. Rautiainen (1999) support that clustering of particles occur even at very high voidage of 99.97% and slip velocity immediately starts to be greater than terminal, because sedimentation does not occur in solid-gas flows like in liquid-solids systems. More details in chapter 3.4.2

Although the controversy upon particle clustering, the scientific community established that full lean phase and individual particles behavior can safely be assumed. G.E. Klinzing et al. (2010) demonstrated the systems behavior with gradual increase in solid loading, as shown in Figure 3.6a-f. Table 3.1 demonstrates various investigators and their experiments upon vertical particle distribution in pneumatic conveying. They similarly observed that wall region was more concentrated with increasingly solids fraction and in consequence certain back-mixing or back-flow occurred. G.E Klinzing et al. (2010) proposed Figure 3.6 as a well representation of particle distribution in pneumatic lines with gradual increase in solid loading.

Table 3.1. Wall Region particle concentration experiments, adapted from G.E. Klinzing et al. (2010)

Investigators	Particle Diameter [μm]	Pipe Diameter [m]
Soo et al. (1964)	50	0,130
Arundel et al. (1970)	15	0,073
Zenker (1972)	42	0,041

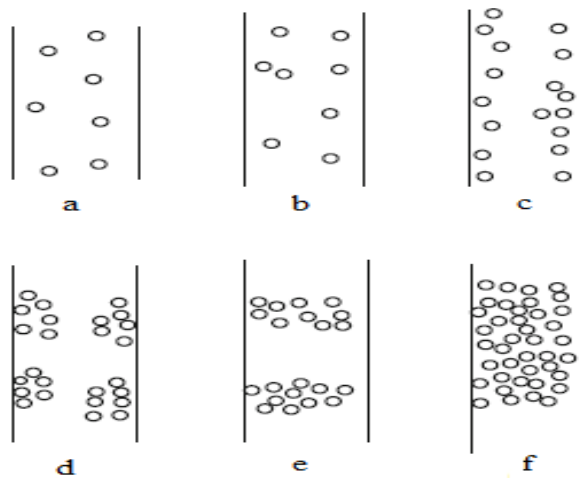


Figure 3.6. Distribution of particles in vertical pneumatic line with increasing solid feed, adapted from G.E Klinzing (2010)

3.4.2 Slip Velocity in Pneumatic Transport

As explained in chapter 3.3.3 the current situation on the theory is that slip velocity equals terminal velocity at very high voidage, because the particles tend to work individually in a fully disperse flow. The slip velocity in a situation like this can be derived by Equation 3.1 (Yerushalmi et al. 1978).

$$U_s = \frac{U_g}{\varepsilon} - U_{solid} \quad (3.1)$$

where $\varepsilon > 99\%$ resulting to:

$$U_s \approx U_g - U_{solid} = U_{terminal} \quad (3.2)$$

In chapter 3.4.1 was briefly mentioned the controversial situation upon slip velocity behavior in pneumatic transport lines. Matsen (1982) demonstrated a detailed and well imposed work on choking mechanism where he theoretically through data collection explained why sedimentation phenomenon is not occurring in solid-gas system, resulting to particle clustering even at very low volume fraction of 0.0003. Matsen assumed negligible wall friction, fully accelerated flow and uniform particles size, which assumptions matched a fluidization vessel where bed diameter is reasonably large and mean particles size small.

Wen and Hashinger (1960), Koglin (1971), Johne (1966) experimental data and results upon slip velocity behavior with gradual decrease of voidage from 1 until 0.9, as shown in Figure 3.7. Solid-gas flows were used in the Wen and Koglin experiments, where slip velocity indicated equal numbers with terminal from 0-0.0003 solid volume fraction. After 0.0003 solid volume fraction, the slip velocity started to gradual increase and become greater than terminal until the end of data. On the other hand, Johne (1966) performed the same experiment but for liquid-solid flow. The slip velocity indicated same results in the beginning of the gradual decrease of voidage, however after a point, slip velocity stopped to gradual increase and started to decrease as shown in Figure 3.6. Matsen (1982), stated and supported that the sedimentation phenomenon is not occurring in a gas-solid system in the same way as in liquid-solid system. Particles in gas-solid flow tend to cluster from 0.0003 solid volume fraction and never again fully disperse in the volume because of sedimentation. Thus, the slip velocity will start taking higher values from terminal even at very high voidage.

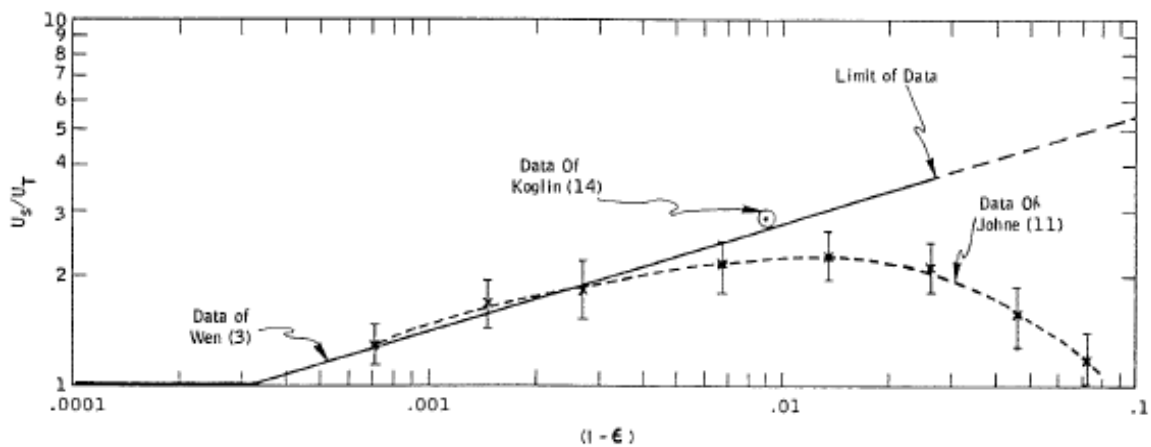


Figure 3.7. Slip velocity vs voidage experimental data and results, adapted from Matsen (1982).

Rautiainen et al. (1999) with their experimental study of 0.192m bed diameter, mean particle size of 64 μm and solid volume fraction in range of 0-0.01 upon vertical pneumatic conveying, indicated same results as Matsen (1982). Slip velocity was gradually increasing with increasing solid volume fraction after 0.0003, as shown in Figure 3.8. Resulting, in increasing slip velocity when gas velocity is decreased, or

when mass flux G_s is increasing, or with increasing solid concentration, which phenomena are well describing the upcoming choking limit of pneumatic transport.

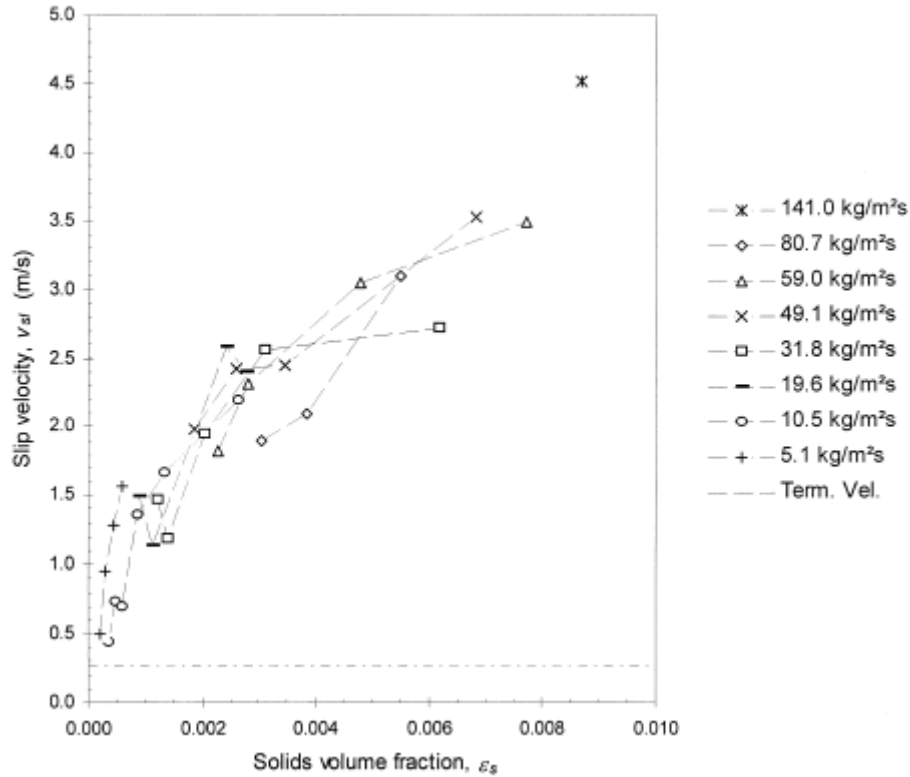


Figure 3.8. Slip velocity vs solid volume fraction Rautiainen et al. results (1999)

In the frame the entrainment flow model for the calcium looping process the determination of the slip velocity and in consequence the solid velocity in order to define the mass balance of the system is on the main importance. Matsen (1982) and Rautiainen et al. (1999) works where both well imposed and detailed explaining why slip velocity should be greater than terminal even at very low solid fraction. However, Ravi Sankar and Smith (1986), shown how solids velocity can differ with tube diameters. Effects like particle-wall friction, particle-particle interactions and particle clustering can greatly change results. Thus, the work done in the specific theory is yet to poor. More research on clustering of particles in high voidage is needed with bigger range of diameter tube and particle size. On the other hand, the prevail theory that slip velocity equals terminal at voidage greater than 99% is supported from many investigators and book authors (Kunii and Levenspiel 1991, D. Geldart 1986, P. Basu

1991, Yerushalmi et al. 1978). The main explanation is the logical thinking and physically proven that an individual particle will behave like that. Because in pneumatic lines, the particles supposed to move more individually rather than grouped, the prevail theory is a decent first approach for the entrainment flow model for calcium looping process and equation 3.1 can be utilized.

3.4.3 Choking and Entrainment: Choking Classification

Bi et al. (1993) in their attempt to distinguish the type of choking occurring in each situation, they classified the choking phenomenon into three types. Type A, or "accumulative choking", type B "blower standpipe-induced choking", and type C "classical choking". Type C choking is defined as the choking where accumulation of solids will result to dense phase and slug formation upon the column. Type B choking is resulting from the energy systems failure. Type A choking phenomenon happens, when the saturating carrying capacity of the pneumatic line is reached and further increase in the solid loading will result to accumulation of solids and alteration into a denser phase without any slugging in the column. Type A accumulative choking is of the main interest for the model done in this paper. Understanding the phenomenon of coexistence of choking in entrainment flow and determining ways to predict choking velocity is crucial for the work done in this paper.

Matsen (1982) was the first to introduce the coexistence of choking and entrainment with his theoretically work done in choking mechanisms. Based on his theory that slip velocity starts to increase and become greater than terminal even at very low solid fraction of 0.0003, he adapted the work of Wen and Hashinger (1960) and derived a schematic flow map, as shown in Figure 3.9. The resulting increasing slip velocity with gradually decrease in gas velocities or increase in solid concentration is well explaining the choking mechanism in entrained flow and pneumatic transport lines. The schematic flow in Figure 3.8 demonstrates the relation of solids velocity ($G/P_p u_t$) with gas velocity (u/u_t) and voidage (ε) as independent variable. With starting point voidage of equal to 1, as the gas velocity decreases the voidage gradually decreases until a velocity

where the gradual decrease of voidage becomes abrupt and the dilute phase alternate into denser phase. The same alteration of voidage was similar observed for increasingly solid velocities or solid load.

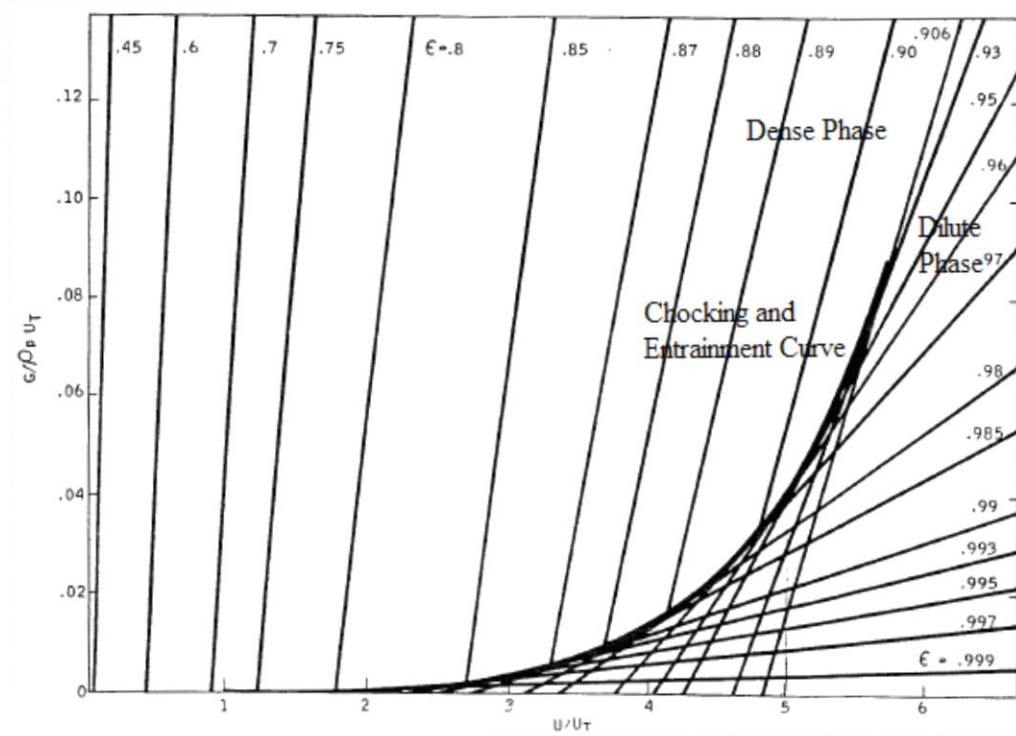


Figure 3.9. Flow Map for gas-solids upflow adapted from Matsen 1982

Yang (2004) in his revisit in choking mechanism at pneumatic transport, defined accumulative type A choking as the transition from dilute phase and pneumatic transport regime, into denser phase and fast fluidization regime. Yang adapted the comparison data of Bai et al. (1998) for different various models predicting classical type C choking and type A choking velocity and derived a map flow, as shown in Figure 3.9. Type C choking at the left side of the curve was determined using Yousfi and Gau (1974) choking model and Yang's (1983) choking model. Type A accumulative choking, at the right-hand side, was determined using Bi and Fan's (1991) model. The incipient fast fluidization boundary was derived from Yang's previous work in 1993. From Figure 3.10 the alteration from dilute phase into fast fluidization after choking velocity can be observed.

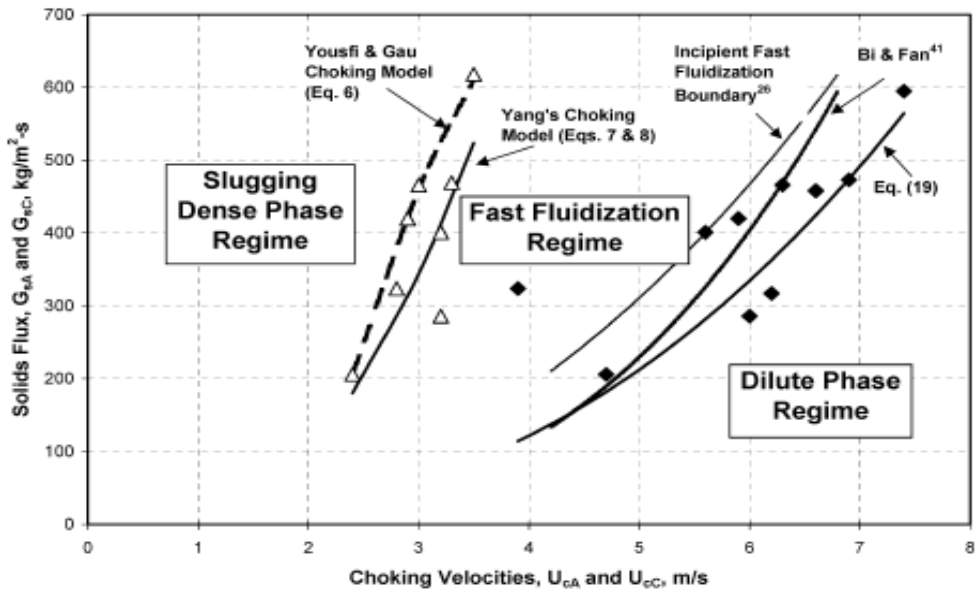


Figure 3.10. Comparison of data from Bai et al. (1998) from various models, adapted from Yang (2004).

3.4.4 Choking and Entrainment: Determine Choking Velocity

As explained in chapter 3.4.3 in the frame of this work, type A accumulative choking is on the main interest. Previous work from Deliverable 3.2 and results are reviewed and analyzed to determine appropriate methods and correlations to utilize and come up with new detailed analysis on choking velocity. Revising previous deliverable, four correlations were approved as decent to determine accumulative choking velocity, as shown in Table 3.2. Punwani et al. correlation indicated the highest values of choking velocity compared to the other three, and Case D where the solid load is the highest, pointed out the greater velocity between the cases and reasonable Punwani correlation nominated as the most accurate.

Table 3.2. Correlations for accumulative type A choking, adapted from Deliverable3.2.

Reference	Correlations	Choking Velocity ($\frac{m}{s}$)			
		Case A	Case B	Case C	Case D
Punwani et al. (1976)	$\frac{u_{ch}}{\varepsilon_{ch}} - u_t = \frac{G_x}{p_x(1-\varepsilon_{g,ch})}$ $p_g^{0.77} = \frac{2250 D (\varepsilon_{ch}^{-4.7} - 1)}{\left(\frac{u_{ch}}{\varepsilon_{ch}} - u_t\right)^2}$	5.35	5.82	5.63	6.13
Bi and Fan (1991)	$\frac{u_{ch}}{\sqrt{g d_p}} = 21.6 \left(\frac{G_x}{p_g u_{ch}} \right)^{0.542} Ar^{0.105}$	1.97	2.17	2.08	2.29
Xu et al. (2001) ($Ar < 50$)	$\frac{G_x}{p_x \mu_g} = 0.0158 \left(\frac{Ar}{100} \right)^{4.093} \left(\frac{u_{ch}-u_t}{u_t} \right)^a \left(\frac{D}{d_p} \right)^b$ $a = 2.355 - 0.00191 Ar$ $b = 1.740 - 0.441 \ln(Ar)$	1.99	2.32	2.14	2.50
Yang (2004)	$G_x = 3.8364 u_{ch}^{2.4938}$	2.54	2.85	2.71	3.04

Determine choking velocity and the safety gap of operation in dilute phase and pneumatic transport is on the main importance. Spinelli (2018), with his research in CLEANER 1D model of the carbonator, stated that the efficiency of the carbonator and CO₂ capture is highly dependent of the solid concentration and solid-to-gas ratio. Thus, implementing higher solid load or decreased gas velocity will lead to higher

residence time, and as the choking velocity allows the system to operate in dilute phase, the calcium looping process will yield larger values of efficiency.

3.4.5 Density Profile at Pneumatic Transport

In the chapter 3.3.2 the vertical density profile at fast fluidization was defined and explained why an S-shape solid distribution will prevail in the regime, supported by the most scientific community and a various collection of experiments. Kunii and Levenspiel (1991), in their entrainment model explained that TDH height will gradually decrease with increasing gas velocity, resulting finally to a fully entrained flow where all the particles are evenly distributed in the reactor. When the gas velocity is gradually increasing, less and less solid concentration will decrease in the upper section of the bed, compared to the bottom bed where the decrease in solid concentration will become greater.

Kwauk (1980), adapted that theory and he created a mathematical model where the S-shape solid distribution from fast fluidization with increasing gas velocity and alteration into pneumatic transport becomes eventually equal across the height of the reactor. Revisiting the phenomenon in 1992 with his book, stated that the approximation is still valid for a mathematical point of view but not realistically and physically 100% fully accurate.

In the frame of the entrainment flow model, density profile and in consequence voidage, solid flux distribution and pressure gradient can be assumed equal across the vessel for a first decent approach to the model. However, understanding upcoming inaccuracies are on the main importance. Inaccuracies like slightly increasing density at the bottom feed point are to be considered.

4. CURRENT STATE OF CALCIUM LOOPING MODELLING

The economical challenge and incapability of the researchers to build prototype energy systems for further physical analysis has led the community to turn into modelling and representation of these prototypes with digital studies. In addition, modelling except from being economical feasible is further providing flexibility in investigating the project. In modelling one can change any physical parameter and assumption by a simple configuration in the software, while in mock-ups a change in assumptions may even need whole reconstruction of the system.

In the frame of Calcium Looping process modelling, 1D representations by using Matlab/Simulink environment with C coding or FORTAN are widely used to model the whole coupled process dynamic behavior of the sorbent, chemical reactions and hydrodynamics between the two reactors. In addition, 3D models are implemented to solve parts of the whole process in a more realistic and accurate approach. The accuracy comes from the capability of CFD software, for dense meshes, to perform numerical solutions based on the conservation of mass, energy and momentum. However, the computational capacity at current state limits the 3D approach and a whole interconnected coupled system with both reactors operating at the same model it is not yet feasible or even if it is feasible, the time required for convergence of a system like this, would have been enormous and challenging for any researcher to achieve satisfying results.

In this chapter, fundamental previous works of Shimizu et al (1999), Alonso et al (2009), Romano C. Romano (2012), J. Ylätalo (2012-2014), Spinelli et al. (2018) and their modelling approaches on CaL process are being analyzed. The objective is to determine the current state of CaL modelling by evaluating the works from the beginning of the idea until the present situation. The inquiry will be focused on what techniques, assumptions and criteria where used from the authors to model specific important features of the system.

4.1 CaL Model by Shimizu et al. (1999).

Shimizu's et al. (1999) work was the first to propose a twin fluid-bed reactor coupled system for CO₂ absorption. One of the main objectives of their work was to prove that their new process (CaL) is more energy efficient on capturing carbon dioxide compared to the prevail process of O₂/CO₂ combustion. In general, their study and aim were to demonstrate the CaL process benefits, and not to go deep into modelling of the carbonator. For instance, the effects of coal ash and sulphur were not included in the model. However, their observations and results of the model were crucial for the future development of the process.

Their hydrodynamic model is based on the two-region, bubble and emulsion model imposed by Kunii and Levenspiel (1991), with reactor operating on BFB regime. The particle distribution is uniform and relatively large, in the order of 0.42-0.59 millimeters. The cross-sectional area is determined by the flow rate of gas and the superficial gas velocity. In addition, the conversion rate of CaO to CaCO₃ is determined by a simple model equation:

$$\frac{dX}{dt} = C_{av} k (D - X) \quad (4.1)$$

Where k is the reaction constant, D is the maximum conversion which was tuned to less than 0.3 because of the loss of activity after the first loops. The C_{av} is the average concentration of the carbon dioxide and is determined by the difference of it between the inlet and outlet, calculated as follows:

$$C_{av} = \frac{C_{in} - C_{out}}{\ln\left(\frac{C_{in}}{C_{out}}\right)} \quad (4.2)$$

The results of the conversion rate are demonstrated in Figure 4.1, where it was observed that after each carbonation-calcination cycle, the conversion of CaO to CaCO₃ is decaying.

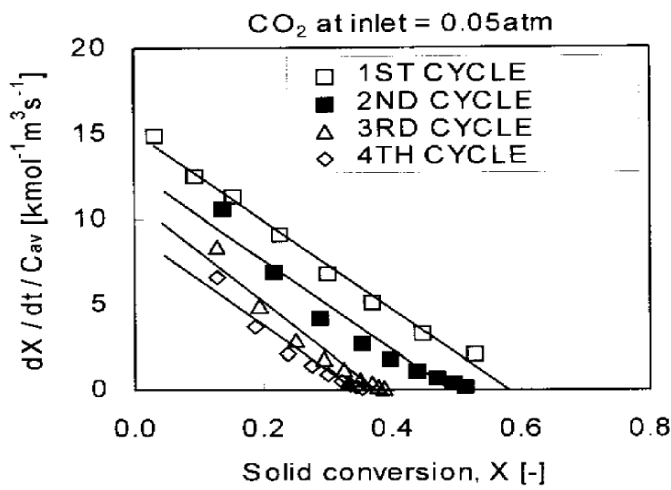


Figure 4.1. Change in Conversion Rate, adapted from Shimizu et al. (1999, 66)

Furthermore, by utilizing the reaction kinetics and equation above, and by assuming complete mixing of solids in the reactor, for two different reactor heights taking into consideration the required height for heat recovery. They resulted to Figure 4.2, where it is clearly seen that even with low maximum conversion of 0.1 the CO_2 removal is still high, in the order of 83%.

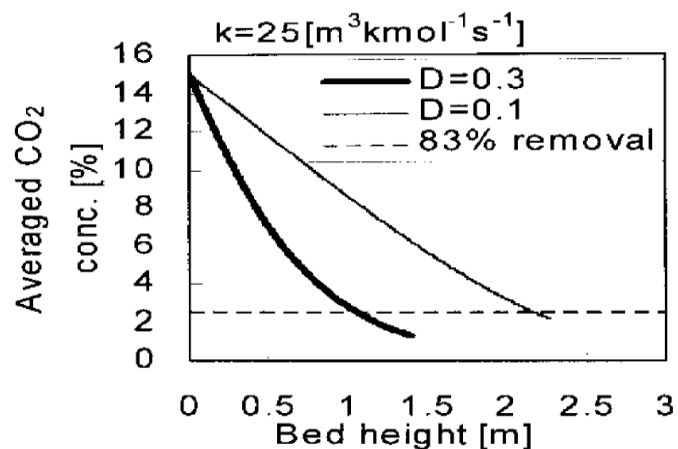


Figure 4.2. CO_2 concentration profile in the carbonator, adapted from Shimizu et al. (1999, 67)

4.2 CaL Model by Alonso et al. (2009).

Alonso et al. (2009) developed a model coded in matlab environment for the process diagram shown in Figure 4.3. As it can be seen from the figure, the model is composed of two interconnected CFB reactors, where solids circulation of CaO and CaCO₃ is occurring. The main objective was to determine various CO₂ capture efficiencies with different solid inventory and solid circulation rates. The efficiency was estimated by the following equation:

$$E_{carb} = \frac{\text{CO}_2 \text{ reacting with CaO in the bed}}{\text{CO}_2 \text{ entering the bed in the flue gas}} \quad (4.3)$$

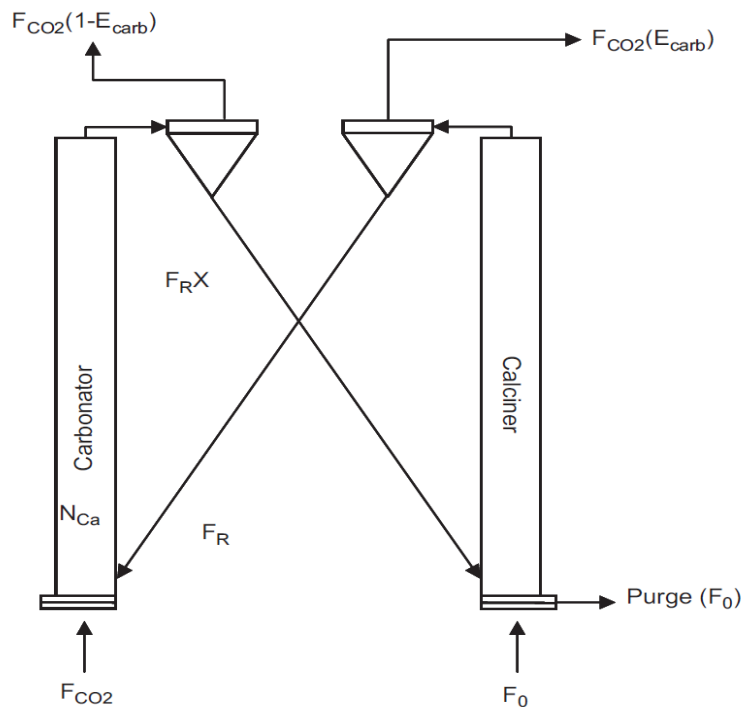


Figure 4.3. Process diagram of Alonso et al (2009, 884). modeling of CaL work.

Their main assumptions were perfect mixing of the solids in both reactors, gas plug flow in the carbonator and complete calcination of the particles. The kinetic reactions were optimized for highly cycled particles. In addition, the effects of coal ash and sulphur were not included, however the need of continuous make up flow to purge the

ashes and CaSO₄ were mentioned and reported. Furthermore, the sorbent capacity decay phenomenon was calculated by the maximum conversion equation of Grasa and Abanades (2006):

$$X_N = \frac{1}{\frac{1}{(1 - X_r)} + N k} + X_r \quad (4.4)$$

Kunii and Levenspiel (1990) stated the importance for accurate knowledge of the hydrodynamics in circulated fluidized beds, in order to ascertain the circulation rate of the solids, the total mass of CaO in the reactor, and the gas-solid contact conditions and phenomena. Although, in the work of Alonso et al. (2009), the three parameters mentioned above were not measured but rather selected to match industrial scale CFB combustors. Which sets relatively poor hydrodynamic analysis. However, the focus was on proving that the process is ready for scaling up.

In the main results, they demonstrated different CO₂ capturing efficiencies for various solid inventories and solid circulation ratios, as shown in the Figure 4.4. They saw that high efficiencies could be achieved when the solid-to-CO₂ ratio is increasing or by escalation of the solid inventory in the reactors. In addition, they concluded that the calcium looping process is definitely an efficient system, but extra care is needed in the above parameters, as they can as well contribute to deficient performance, when the values selected are inappropriate.

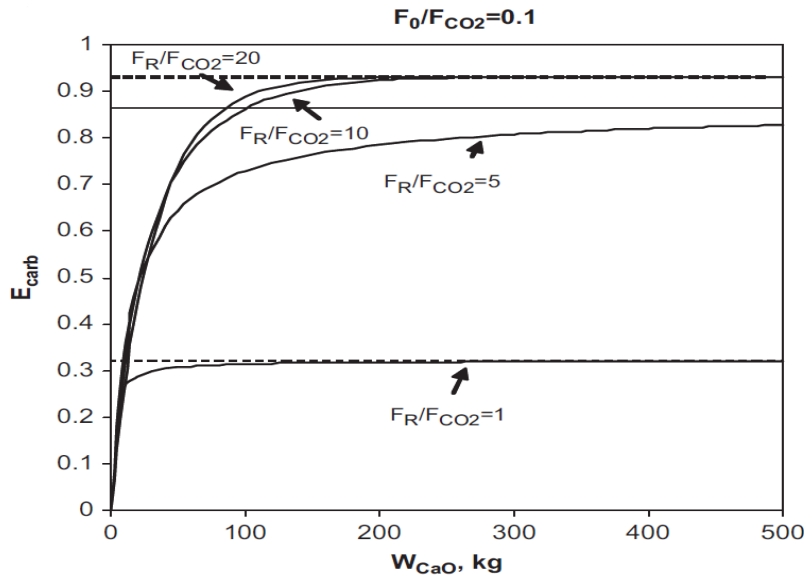


Figure 4.4. CO₂ Capture efficiency as a function of solid inventory, for different solid-to-CO₂ ratios, adapted from Alonso et al. (2009, 888).

4.3 CaL Model by Romano (2012).

In 2012 Romano published his work on CaL modelling. The goal was to demonstrate various capture efficiencies, when the reactor is operating in different conditions (Solid inventory, solid-to-gas ratios). The freeboard, core-annulus model adapted from Kunii and Levenspiel (1990) was implemented in Matlab environment and his work included higher approximations of the hydrodynamics and reaction kinetics of the process compared to the current at the time researches. The specific K-L model was chosen because it can provide accurate estimation of solid formulation and distribution across the height of the CFB vessel.

The remarkable of the article-model was that the effects of coal ash and sulphur were taken into consideration. This was actually the first attempt in the CaL process modelling history, and results of it were demonstrated. Despite the fact that, the effects of sulphur and ash were neglected by many investigators at the time, its importance on sorbent deactivation is considerable high. In both reactors, SO₂ can react with CaCO₃ and CaO, in direct and indirect sulphation respectively, and the formed CaSO₄ not only

is consuming the active sorbent but also causes blockage of the active pores. (Grasa et al. 2008b)

The model assumptions were uniform temperature in the CFB riser, negligible gas side mass transfer resistance, perfect mixing of the fragments, uniform fragment dimension and homogeneous superficial velocity. Most of the assumptions were justified by the fact that in fast fluidization regime and in CFB reactors excellent heat transfer, perfect gas-solid contact, vigorous solid mixing and high solids recirculation rates are prevailing. However, the assumption of uniform particle dimension is not one hundred percent accurate because of particles collision, agglomeration and sintering, and should be removed in cases where data and behavior of a specific reactor are available.

The main flows of the modeling process of the specific energy system were included as shown in Figure 4.5. The input values in the Matlab environment were namely, solid inventory (W_s), fraction of the fresh limestone to fraction of CO₂ ratio (F_O/F_{CO_2}), mole flow of CaO from calciner to fraction of CO₂ ratio (F_R/F_{CO_2}), fraction of sulphur flow to fraction of CO₂ ratio (F_S/F_{CO_2}), mole flow of ash to mole flow of CO₂ (F_{ash}/F_{CO_2}), volume of the gas in ($V_{g,in}$), concentration of CO₂ in ($C_{CO_2,in}$), Height of the reactor (H_t), superficial gas velocity (u_0), particle mean size (d_p) and pressure of the reactor (p). The specific parameters were used for the sensitive analysis and results demonstration.

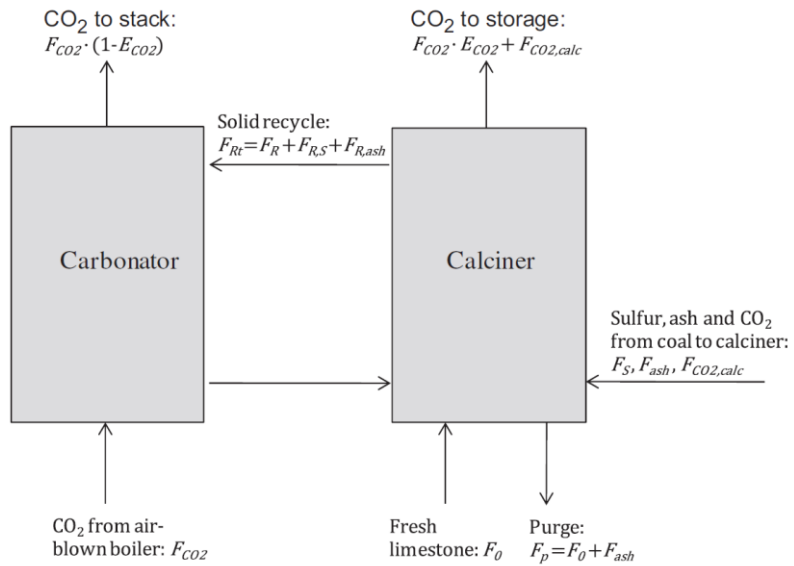


Figure 4.5. Main flows of the model, adapted from Romano (2012, 262)

In his results, various figures were demonstrated, showing how sensitive or not is the system to changes of the parameters mentioned in the previous paragraph. In the frame of this report for simplicity and importance acknowledgement, only Figure 4.6 is being included, from where the main results can be observed. The capture efficiency seems to increase with solid inventory escalation, as was shown in the previous two CaL modeling works analyzed. Furthermore, fresh limestone and CaO in the system were increasing the efficiency. Concluding, efficiency drop caused by sulphur and ash was noticed.

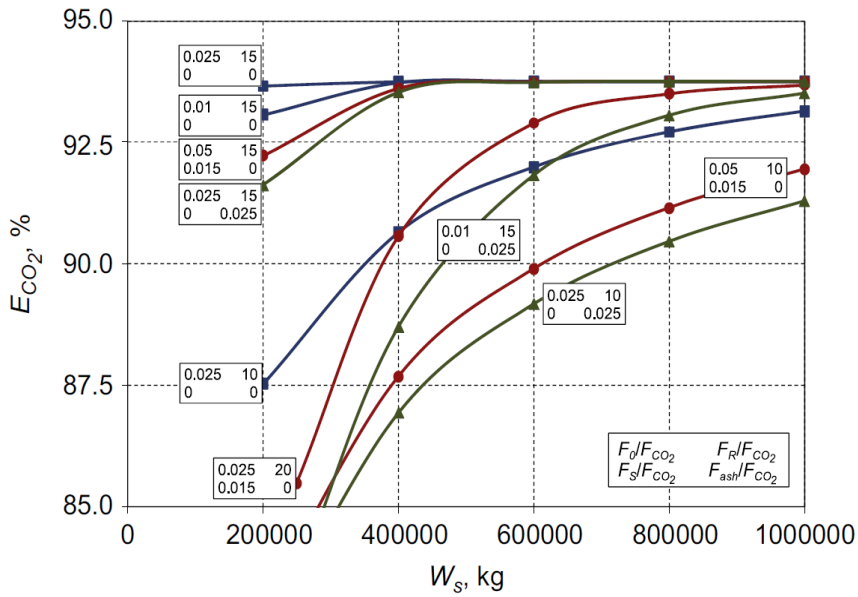


Figure 4.6. CO₂ capture efficiency vs solid inventory, for different fraction ratios between sulphur, ash, fresh limestone and CaO to fraction of CO₂, adapted from Romano (2012).

4.4 CaL Model by Jaakko Ylätalo et al. (2012-2014)

4.4.1 Article Published on 1D CaL Model, by J. Ylätalo et al. (2012)

In 2012, Jaakko Ylätalo published his work on a dynamic 1D model of calcium looping process. The aim of the model was to validate a laboratory scale reactor of 30 kW situated at INCAR-CSIC, Oviedo, Spain. The validation process included comparison of the temperature profile and capture efficiency in the carbonator, between the experimental data and the simulated. Furthermore, the model was built in Matlab/Simulink environment compiled with in house C codes. In comparison with the other works presented in this report, Ylätalo's model was able to perform unsteady mass and energy conservation equations for each time step, under specific gas-solid concentrations and temperature for the both fluidized bed reactors interconnected together. In addition, it provided calculations of incomplete mixing, which offers extra detail analysis of physical phenomena and further accuracy.

The 30 kW test rig situated in Spain consists of two circulating fluidized bed reactors with diameter of 0.1 m and height of 6.5 m. The operating temperature of the carbonator

is close at 650 °C and in the calciner at 700-800 °C. Further and accurate description of the specific test rig is provided by Alonso et al. (2010). Furthermore, the comparison between the experimental and simulated results were taken by selecting measurements from the test rig while it operated and remained at steady state for a longer period of time. The results between the cases showed excellent agreement, as shown in Figure 4.7 and Figure 4.8. The capture efficiency was increasing with inventory escalation as expected. However, the temperature profile agreement was not so accurate, with overestimation of it in the lower bed. This occurred because in the test rig the cooling of the reactor was performed by removing the insulation, which was not simulated in the model. Although, the predicted simulated higher temperature in the lower bed, better agrees with realistic industrial scale operations, because most of the active solid is situated in the bottom of the carbonator.

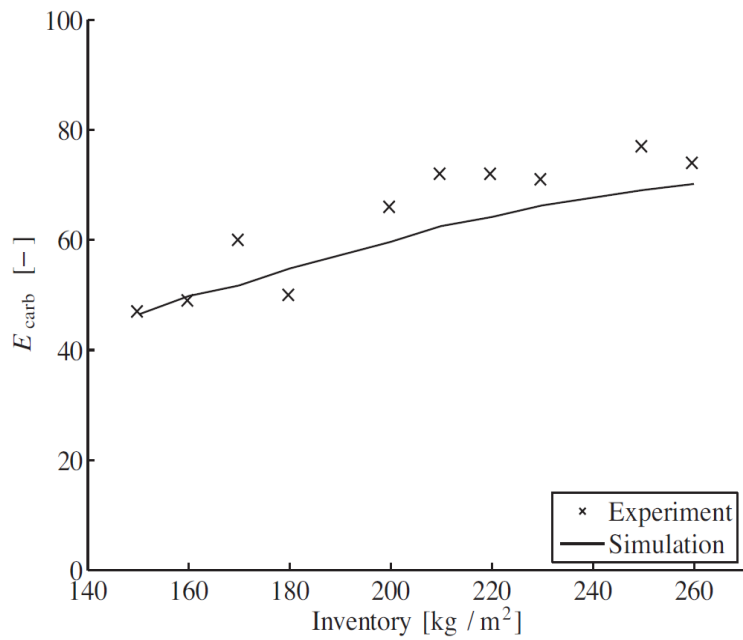


Figure 4.7. Capture efficiency vs Inventory and validation of it with experimental results.
Adapted from J. Ylätalo et al. (2012, 134).

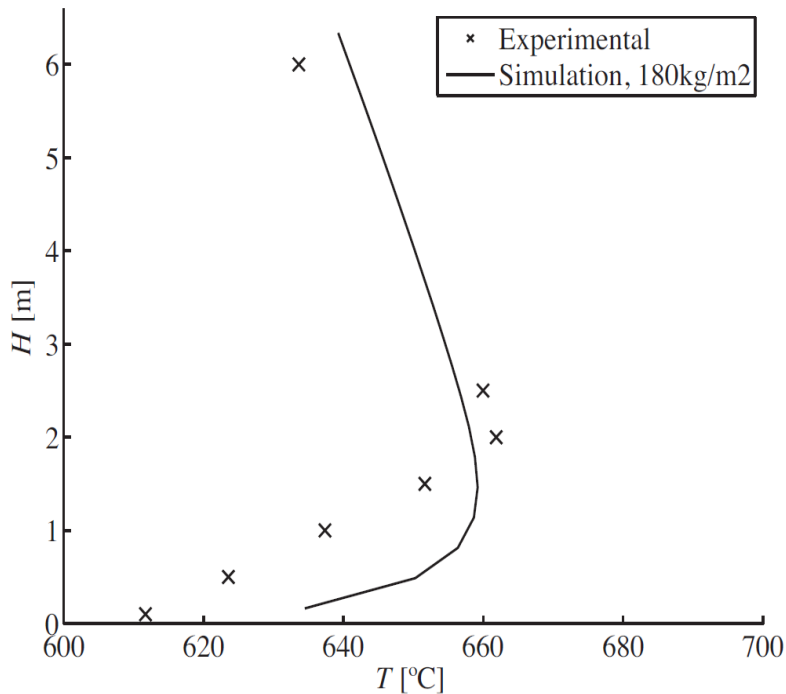


Figure 4.8. Reactor Height vs Temperature in comparison with experimental data. Adapted from J. Ylätalo et al. (2012).

4.4.2 Article Published for the Oxy Combustion Calciner Model, by J. Ylätalo et. al. (2013)

Continuing reporting the work done by J. Ylätalo et al. In 2013 they modelled and published an oxy-combustion calciner for the post-combustion calcium looping process. The aim of the article was the verification and study of a 1.7 MW pilot plant by two different modelling approaches, 1D model process and 3D calciner model. In addition, the oxy-combustion burner was chosen with the purpose of creating pure CO₂ gas stream, suitable for storage.

For the 1D model process, same approach was followed as from his work in 2012. The reactors were discretized, using finite volume method, into 1D cells. Central difference or upwind scheme was implemented for the spatial derivatives. Mass and energy were dynamically solved for each domain. And all the time dependent equations were finally calculated using the ODE explicit fixed-step in the Simulink/Matlab environment.

The 3D calciner was modelled with CFB3D model code. A code which can handle governing balance equation in combination with empirical equations. Myohanen K. (2011) stated that the code is written in Fortran-95 language and it was initially developed to simulate industrial scale CFB units, but it can further perform as a tool of reactor configuration, troubleshooting and risk assessment studies for existing CFB reactors.

In Figure 4.9, the frame of the 3D steady state calciner is being presented. The boiler was modelled by applying finite volume method, in order to discretize and optimize various balance equations in their steady state. In addition, upwind differencing scheme and Gauss-Seidel method was implemented, with purpose of solving the balance equations of total gas, total solids, energy, fuel reactions and species, sorbent reactions and species and homogeneous reactions. Furthermore, sub models simulating the return leg and external heat exchanger were included.

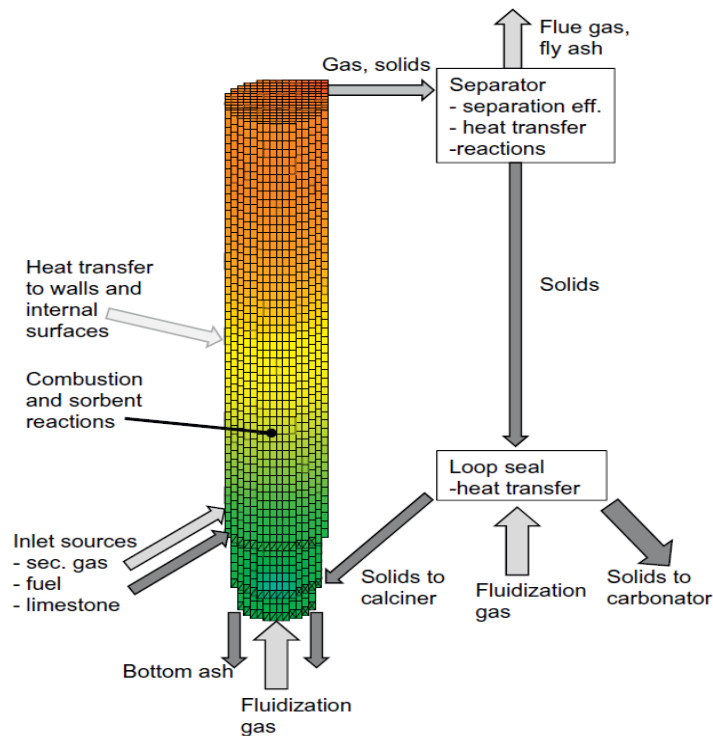


Figure 4.9. 3D steady state frame calciner model with the circulation system. Adapted from J. Ylätalo et al. (2013, 773).

The comparison between the models resulted to the Figure 4.10. The outcome from both simulations varied between 5 °C to 10 °C, which was totally accepted. The small differences between the methods developed from the fact that the CFB3D is capable of performing denser mesh calculations, with considerable extra physical phenomena and more initial variables included. In addition, from the temperature profile it is observed that lower values are obtained in the bottom of the calciner, because of the cold flow upcoming from the carbonators. Escalating in height, the temperature increases due to fuel input and combustion of it, which afterwards will gradually decrease as a result of the endothermic reaction of calcination. Furthermore, from the CO₂ and CaCO₃ representative mol and mass fraction profiles, it is recognized that the calcination reaction is very fast when the temperature attains 890-900 °C ,and more specifically in the first 4 meters of the reactor.

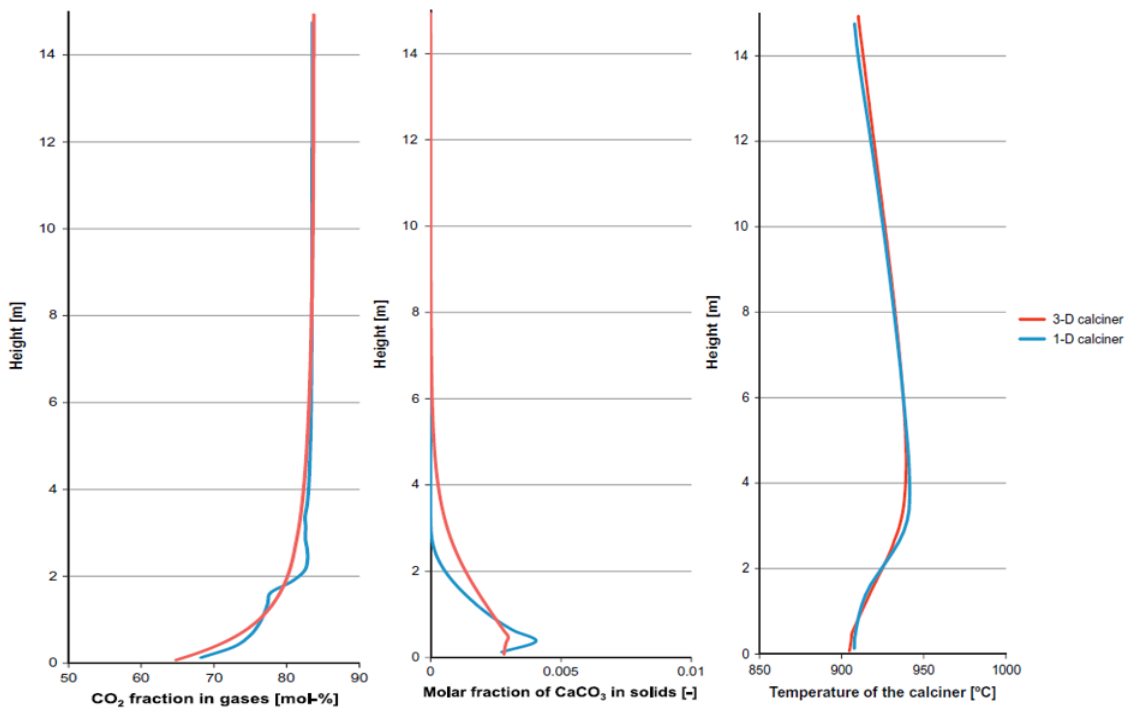


Figure 4.10. Temperature, CO₂ and CaCO₃ profiles across the height of the reactor, comparing the 1D with the 3D results. Adapted from J. Ylätalo et al. (2013 ,775-777).

4.4.3 Article Published for a Model-based Scale-up Study of the CaL by J. Ylätalo et. al. (2014)

Extending the studies from J. Ylätalo et al. In 2014 they published a 1D scale up model study for the calcium looping process. The aim of the report was to demonstrate an industrial scale model for the calcium looping process. The selected thermal power of the model was at 250 MW and the power plant layout can be seen from the Figure 4.11 below. The dimensions of the plant were selected for less financial risk, although based on their CFB experience further scaling of it was considered feasible and realistic pilot plants could make their appearance in the near future. In addition, the 1D model used for the study was an enhanced version of the previous model used in 2012 and 2013 articles, including new material fractions like CaSO_4 , ash, capture of sulfur and heat transfer in the solids from the return leg.

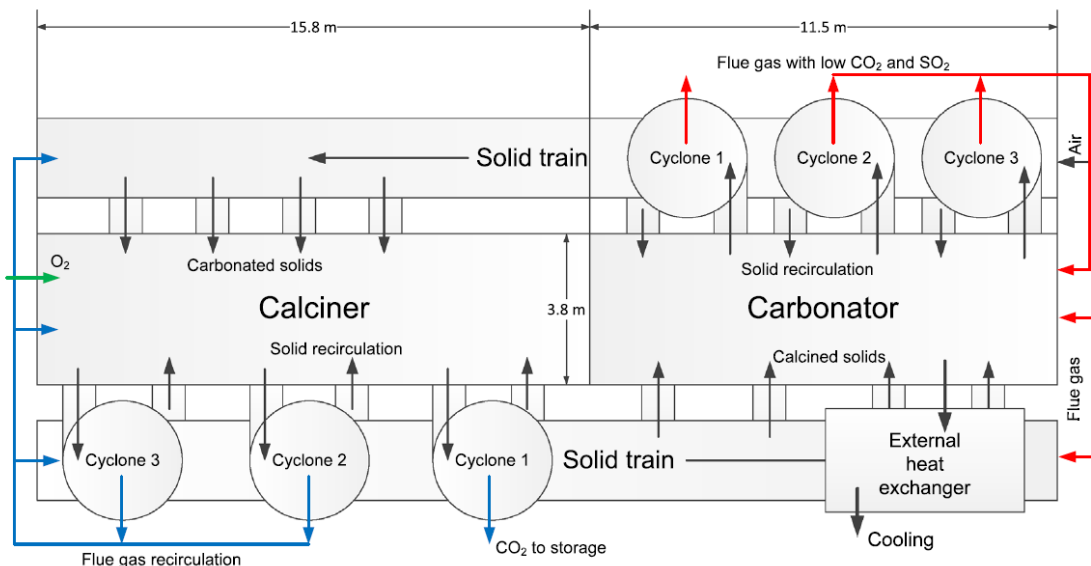


Figure 4.11. Concept power plant layout of large CaL unit, adapted from J. Ylätalo et al. (2014, 332).

The results included various reactor profile outcomes, from solid volume fraction, temperature, CaCO_3 , CO_2 fractions. However, in the frame of this report, the carbonation and thermal efficiency compared to different load scenarios are on the main interest. In the Figure 4.12, it can be observed how the thermal power load in relation

with flue gas flow can influence the efficiency of the unit. The thermal and carbonation efficiency seems to remain high in the range of 82 percent and above even in low power and flue gas loading. This proves that the calcium looping system can run independently from the CO₂ flue gas source (example, cement plant) and operate as a back-up power plant. In addition, the results proved that the successful operation of the CaL unit, heavily depends on the heat transfer layout and cooling mechanism of the high temperature solids transferred from the calciner to carbonator.

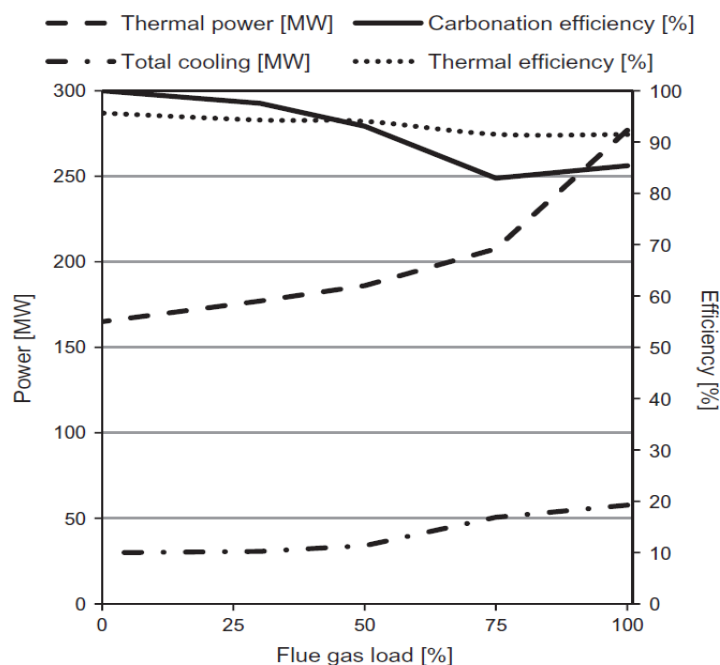


Figure 4.12. Power and flue gas load relation in comparison with thermal and carbonation efficiency. Adapted from J. Ylätalo et al. (2014, 335).

4.4 CaL Model by Spinelli et al. (2018)

Spinelli et al. (2018) developed a 1D steady state model for the calculation of an entrained flow carbonator. The analysis was focused on two different reactor types, namely the high velocity gooseneck-type reactor and a lower velocity downflow reactor. Their main analysis aimed to determine CO₂ capture efficiency and various reactor design parameters discussed below. The equation 4.5 represents the capture efficiency, where $m_{co2,in}$ is the flow rate of carbon dioxide in the inlet of the carbonator, $m_{g,in}$ serves as the gas flow rate at the inlet and m_g is the gas flow rate.

$$E_{CO_2} = \frac{\dot{m}_{g,in} - \dot{m}_g}{\dot{m}_{CO_2,in}} \quad (4.5)$$

The main model assumptions included, calculated gas phase under ideal gas equation of state. Void fraction always higher than 0.98, as the reactor is operating in pneumatic transport with dilute suspension, where particle to particle interactions are neglected. Mass and momentum diffusion across the axial height of the reactor are ignored. Homogeneous solid temperature throughout the particle structure. Concluding, simple fluid-dynamic approach was implemented, mainly because of lack of experimental data from similar studies.

A finite difference method was implemented in Matlab workspace to solve all the mass, momentum and energy balances along the 1D axial height of the reactor, in order to determine the cross-sectional values of the temperature, velocity and chemical structure. In addition, presenting all the equation taken for the specific model is out of the scope of the report. However, one remarkable mention is that the sorbent conversion rate was calculated by the random pore equation proposed by Grasa et al. (2009):

$$\frac{dX}{dt} = \frac{k_s S}{1 - \varepsilon_p} (1 - X) \sqrt{1 - \psi * \ln(1 - X)} (C_{CO_2} - C_{CO_2,eq}) \quad (4.5)$$

where k_s serves as the intrinsic kinetic constant of carbonation reaction, ε_p represents the particle porosity, S is the available surface area of the particle for reaction and ψ serves as structural parameter for a particle. The specific equation was selected because the small mean particle size can justify the neglected diffusion-controlled particle conversion. The proposed equation in this case can yield improved approximation compared to previous famous published equations, for instance by Bhatia and Perlmutter (1983) or Shimizu et al. (1999).

In their main results included that sorbent capacity X_{max} and solid to gas ratio are the main parameters of determining the efficiency of the system. The Figure 4.13 represents the carbon dioxide capture efficiencies under X_{max} equal to 20%, inlet temperature of 600 degrees Celsius and no solid recycle back in the carbonator. In addition, it can be observed that for the gooseneck reactor type, high CO₂ capture efficiencies can be achieved under certain operating conditions. Higher solid to gas ratios and cooler

reactors can yield higher efficiency values, due to the fact that when the temperature of solids and gas are lower in the inlet, the slow carbonation kinetics before the chemical equilibrium are reached further gradually in time.

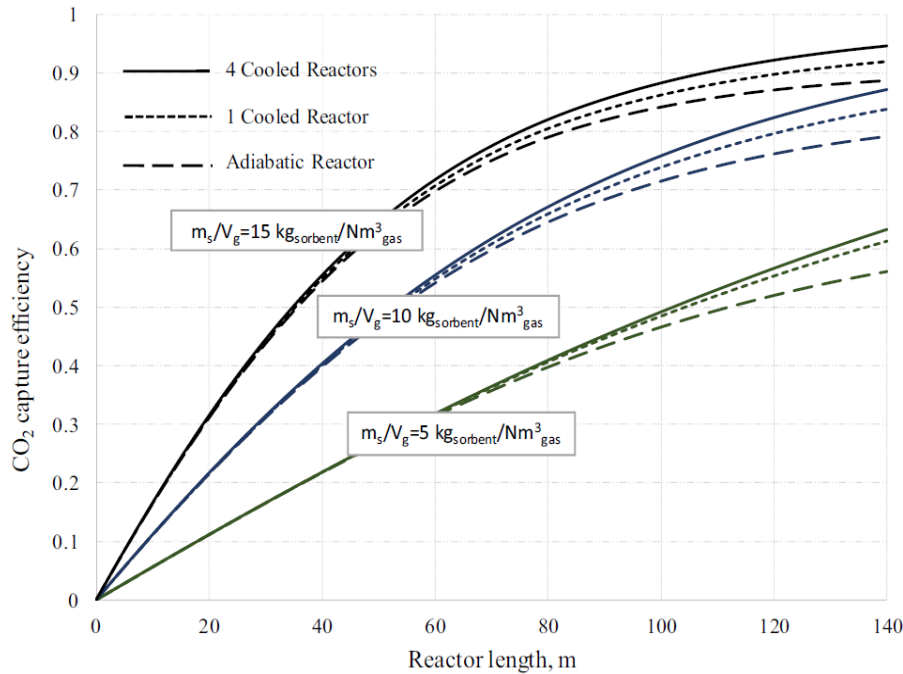


Figure 4.13. CO₂ Capture efficiencies vs gooseneck reactor lenght, for different solid to gas ratio and cooled reactors, adapted from Spinelli et al. (2018, 107).

Furthermore, it can be pointed out that the four cooled reactor and one cooled reactor gooseneck type are performing greater than the adiabatic, however for technoeconomical reasons, due to expensive waterwall cooler reactor, the adiabatic is considered to be a finer choice. In addition, Figure 4.14 was demonstrated, were sensitive analysis performed for recirculation of the solids back in the carbonator inlet. It evaluated that the performance of the reactor was increased, because the Ca particles are still active and away from the X_{max} of 20% at the first two loops, thus 'reusing' them can save wasted material, and furthermore the solid to gas ratio is increasing as if they used carbonated solids from the calciner.

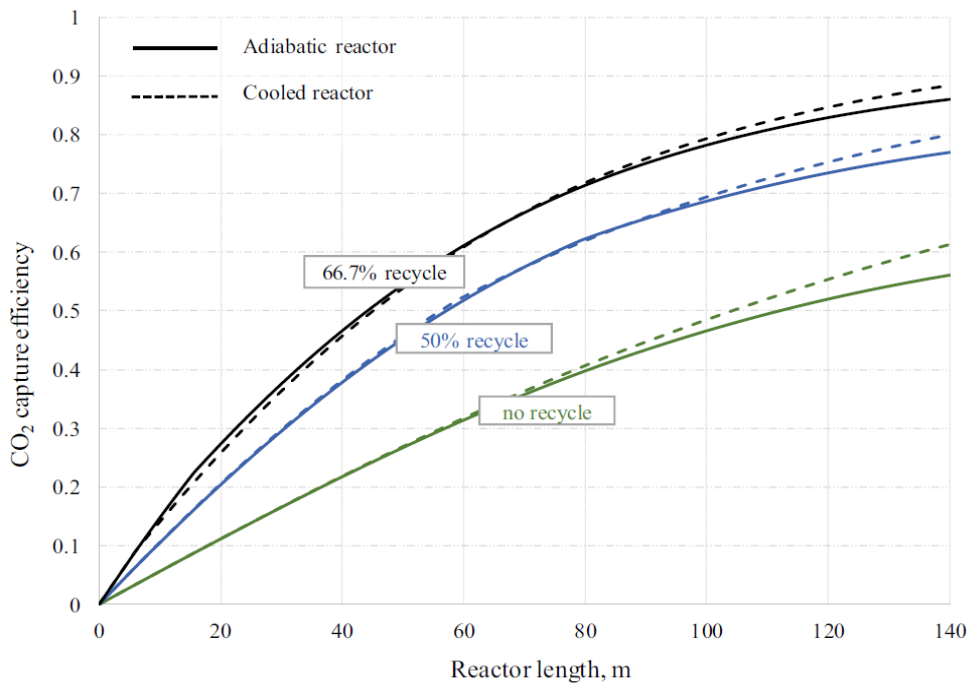


Figure 4.14. CO₂ Capture efficiency vs reactor length under different solid circulation rates, adapted from Spinelli et al. (2018, 111).

4.5 Acknowledgements Upon Current State of CaL Modelling

After historically reviewing various articles and researchers, the calcium looping process modelling seems to have achieved a remarkable state of accuracy in comparison with the phenomena that are actually able to be simulated. From the beginning of the concept and modelling of it (Shimizu et al. 1999), the behavior of the system was gradually becoming clearer to the CaL researching community. Concepts like BFB or CFB as reactor, hydrodynamics, maximum carrying capacity of the sorbent, effects of coal and ash in the system and behavior of the carbonation-calcination loop reaction in the sorbent activity were advancing throughout the years, and the high efficiency of the system was proved by numerous investigators. However, the absence of an industrial scale CaL unit for further experimental results and validation of them, has caused doubts and variations on how the unit will actually operate in this scale, under different operating conditions.

5. DESCRIPTION OF THE ONE-DIMENSIONAL MODEL FOR ENTRAINED FLOW CALCIUM LOOPING PROCESS

The aim of the chapter is to provide detail description of the model assembled for the specific report. First, the CLEANER project with its configurations and processes is being addressed and further explanation of the system is discussed. In addition, the 1D model code is being described in some logical extend. Concluding, solid, gas and energy balances implemented in code level, are explained by demonstrating the representative equations and analyzing the combustion, gasification and sorbent reactions.

5.1 CLEANER Process Description

In the frame of this work, a one-dimensional calcium looping process is being modelled for the CLEANER project (Vernasca Pilot Plant). The emphasis is upon the hydrodynamic behavior of the system, analyzing the solid-gas mixing nature in pneumatic transport regime with respect in choking phenomenon and slip velocity. The carbonator and calciner are both circulating fluidized beds with a unique gooseneck configuration as shown in Figure 5.1. The specific configuration was chosen from previous studies and delivered to the current as a way to increase the residence time of the solids in the reactor and concede higher efficiencies on carbon dioxide capture. Furthermore, important dimensions and hydrodynamic operating conditions are been demonstrated in Table 5.1 and in bullet points below.

- Dilute phase, pneumatic transport regime
- Pneumatic conveying of individual particles
- No particle to particle interactions
- Low mean particle size of $d_p = 20 \mu\text{m}$
- Fragmentation of particles due to sintering from the carbonator-calcination loops
- Void fraction always higher than 98 %
- High solid to gas ratio at carbonator ($\sim 10 \text{ kg/Nm}^3$)

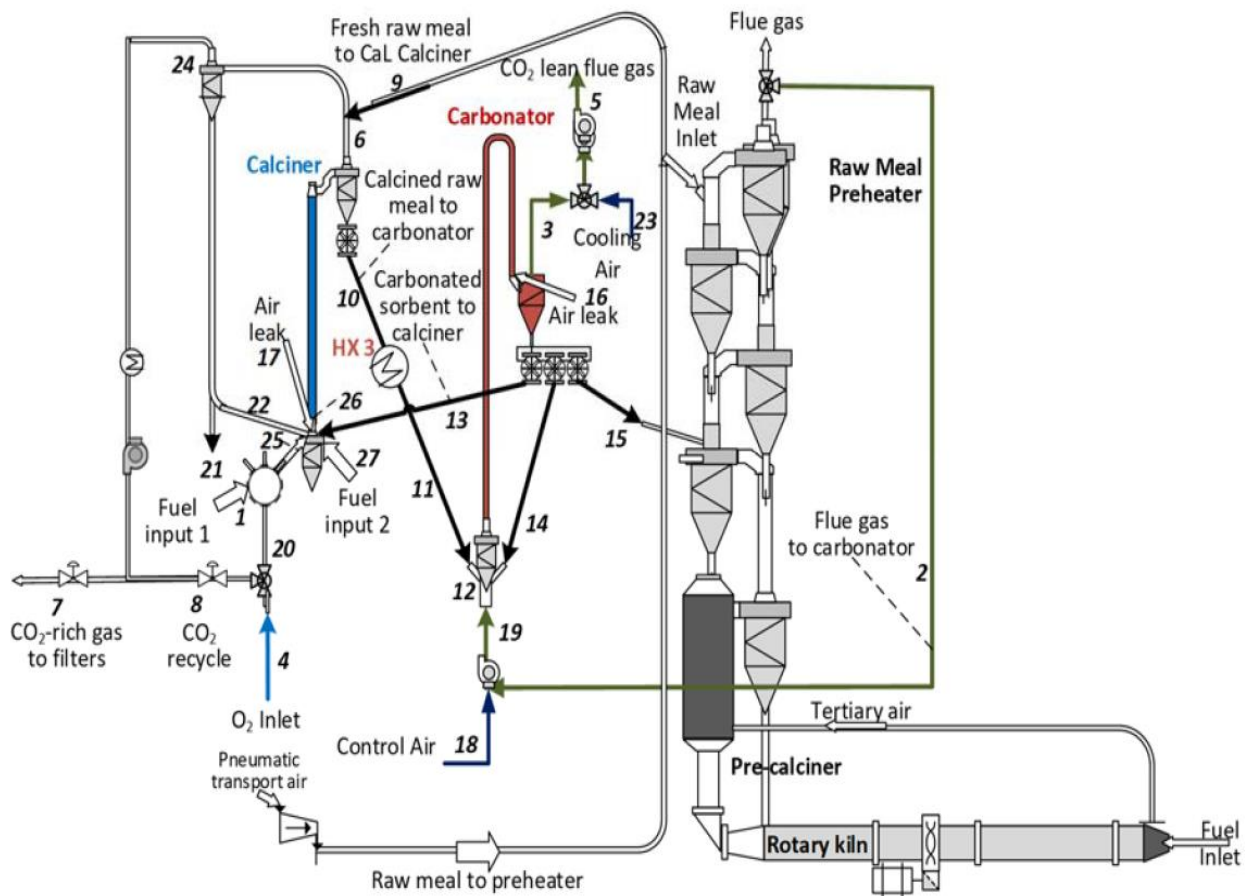


Figure 5.1. Process Schematic of the CLEANER (Vernasca Pilot Plant) project.

Table 5.1. Dimensions of calciner and carbonator for the Vernasca Pilot Plant

	Riser		Downcomer	
	Length [m]	Diameter Inner [m]	Length [m]	Diameter Inner [m]
Calciner	24.8	0.65	16.5	0.65
Carbonator	61.9	0.264	41.6	0.346

As shown in Figure 5.1 the process description includes two interconnected circulating fluidized bed reactors, the calciner and carbonator. Flue gases upcoming from a stationary cement kiln are fed into the carbonator, where the exothermic carbonation reaction (Equation 2.1) is utilized for CO₂ capture purposes. After the carbonator, some fraction of the CaCO₃ solids is circulated back in the absorber in order to increase the usage of the active sorbent and achieve higher efficiencies, and some fraction of CaCO₃ is being transferred in the regenerator, where the solids are heated up to 920 degrees Celsius and the endothermic calcination reaction (Equation 2.5) takes off with the purpose of achieving high CO₂ concentration flue gas in the calciner outlet, which can further be transferred for sequestration and storage of it. The remaining calcined raw meal is then being transferred to the carbonator, where the carbonation/calcination loop is closing.

The high concentration CO₂ flue gas in the calciner is mainly achieved by oxy-combusting heavy fuel oil in two different fuel feed points (#1, #27). The oxidant introduced in the first burner is a mixture of O₂(#4) and CO₂(#8) cooled by radiation and natural convection through the pipe and recirculated back to the system with additional technoeconomical purposes. The first combustor is then producing high temperature (1000 degree Celsius approximately) flue gas, which is being introduced in the calciner inlet for combusting the second fuel feed (#27).

Spinelli et al. (2018) stated and proved that a gooseneck CFB type reactor is the most optimal choice from economical and capture efficiency prospective, regarding the calcium looping process with cement kiln as stationary flue gas source (See chapter 4.4). In this work, both CFB reactors are considered to have gooseneck configuration, operating in pneumatic transport regime. The specific shape allows extend residence time of the solids inside the reactor which proved to achieve higher CO₂ capture efficiencies. In addition, the pneumatic regime and circulation provides excellent solid-gas mixture interactions and reactions, which adds in the performance of the system.

5.2 Overall Model Framework

The 1D model code used is a modified version of J. Ylätalo's et al. (2014) model described in the previous chapter. However, necessary modulations were implemented in code level to achieve the proper hydrodynamics representing the pneumatic transport and gooseneck shape, with the upcoming pressure drop. Roughly, the 1D model code was built in Matlab/Simulink environment, in combination within house C-codes for the proper numerical calculations. Finite volume method was used for the reactor's discretization, and central difference method for the solution of the spatial derivatives. Mass and energy were dynamically calculated per each volume element, and ODE explicit fixed step was finally used in Simulink level to adjust all the time dependent equations. The overall model framework implemented in the work is being presented below, as shown in Figure 5.2

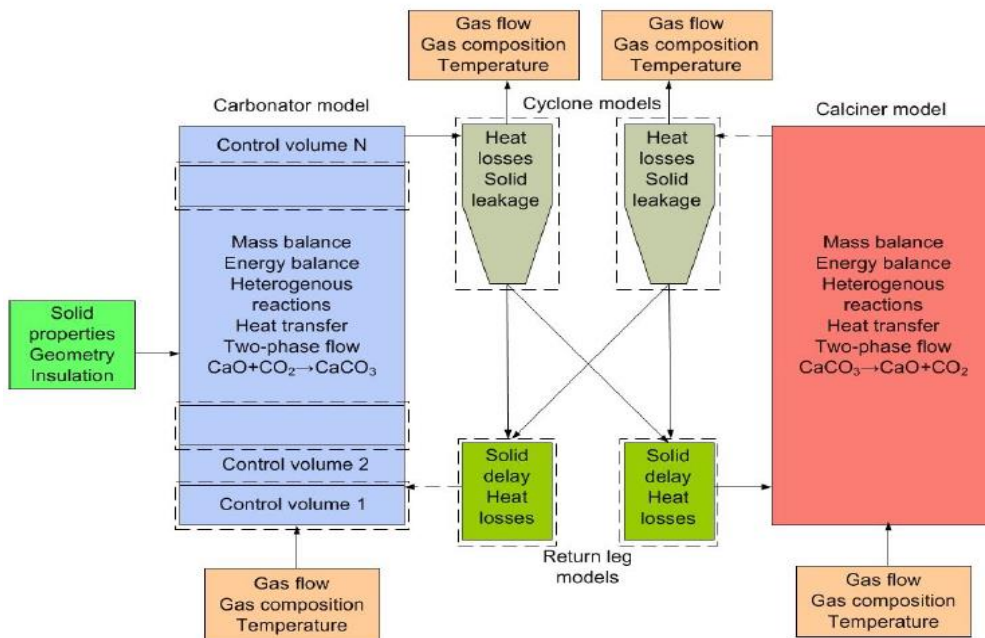


Figure 5.2. 1D Entrained Flow Calcium Looping Process model overall framework.

The assumptions selected for the 1D model were mainly based on the pneumatic transport regime nature (Chapter 3.4). The slip velocity was assumed to have equal values with the terminal velocity, voidage is always equal or greater than 98%, density profile was set to have constant value across the reactor length, which signifies that the voidage and solid flux will follow as well with constant numbers and small fluctuations

in the pressure across the length of the reactor will occur with only one minor pressure drop in the bend of the gooseneck. Concluding, all particles are entrainable, which indicates the disappearance of the dense phase in the bottom of the bed.

5.3 Discretization of Reactor Model

The gooseneck reactor shape was handled by spatially discretizing the riser and downcomer into 1D control volumes, Figure 5.3. The 1D control volumes included, mass and energy perfect balance across the reactor length, and from one domain boundary to the next one. Furthermore, core and wall layers are separately calculated per each control volume. The size of the freeboard and sloped area can freely be chosen and represent any industrial scale circulating fluidized bed reactor. In addition, density, pressure, solids (for instance, CaCO_3 , CaO or ash) and gas (for instance CO_2 , N_2 , H_2O , O_2) were estimated per each mesh cell, providing resulting profiles across the reactor length.

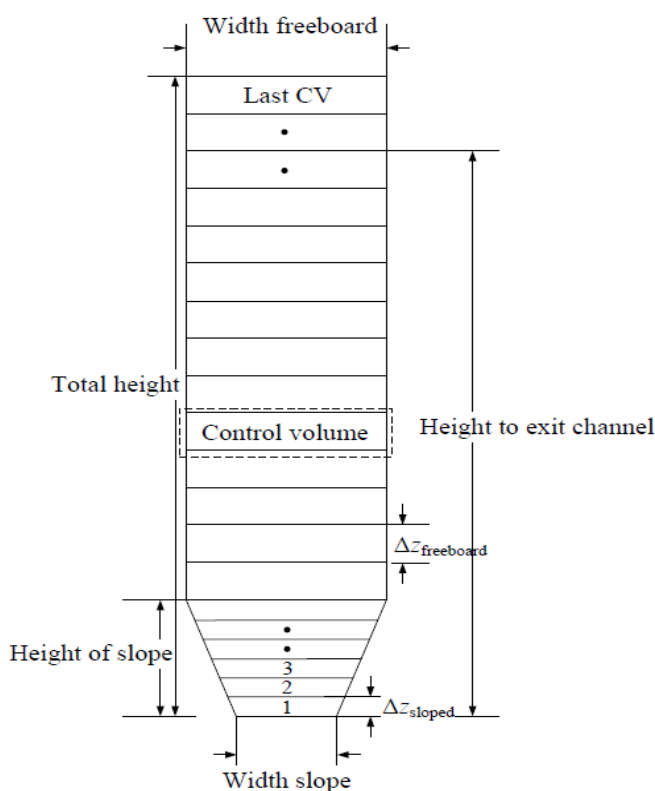


Figure 5.3. Discretization and dimensioning of the gooseneck reactor model.

Because of the gooseneck shape nature, obviously the above discretization does not represent the whole reactor and creates challenges on how the shape can be illustrated in model level. The discretization was finally accomplished by combining two of the reactor models shown in Figure 5.3. The first one is representing the riser of the reactor's shape and the hydrodynamics were set to match the pneumatic transport regime with constant density profile across the height. The second part is describing the downcomer section of the reactor, and the hydrodynamics were configured to match the same as the riser part with additional opposite gravity.

5.4 Mass Balance

To achieve steady solid state in the code, the total mass balance of the reactor, the mass balance of each control volume separately and the wall layers are dynamically being calculated during simulation. In addition, the fraction of CaCO_3 , CaO , ash and CaSO_4 is being measured and the following mass to gas (example, $\text{CaCO}_3 \text{ (s)} \rightarrow \text{CO}_2 \text{ (g)} + \text{CaO} \text{ (s)}$) reactions are estimated and added or subtracted to the balance equations.

The total mass balance, as shown in dynamic Equation 5.1, contain all the solid material introduced to the code (reactor), and the overall mass subtraction, included the reaction gains or losses.

$$\frac{dm_s}{dt} = \sum q_{m,s,in} - \sum q_{m,s,out} + \sum r_s \quad (5.1)$$

where $q_{m,s,in}$ (kg/s) represents the total solid mass flow rate in the reactor, $q_{m,s,out}$ is the total mass flow rate out of the reactor, m_s serves as the overall mass concentration in the system and finally r_s is the total change of solid to gas or the opposite, due to heterogeneous chemical reactions (carbonation, calcination, sulphation). In simulation level, the upcoming mass flow rate can be either the makeup flow, circulation mass flow rate, flow from the other reactor or fuel mass flow (ash).

In addition, the mass balance for one control volume is being calculated similarly as shown in Equation 5.1, however the mass flow rates, heterogeneous reactions and mass

concentration were calculated in domain volume level, Equation 5.2. Figure 5.4 describes all the variables and their flows included in one mesh cell. Furthermore, as mentioned in chapter 5.2, the single control volume was discretized by using finite volume method and first order upwind scheme.

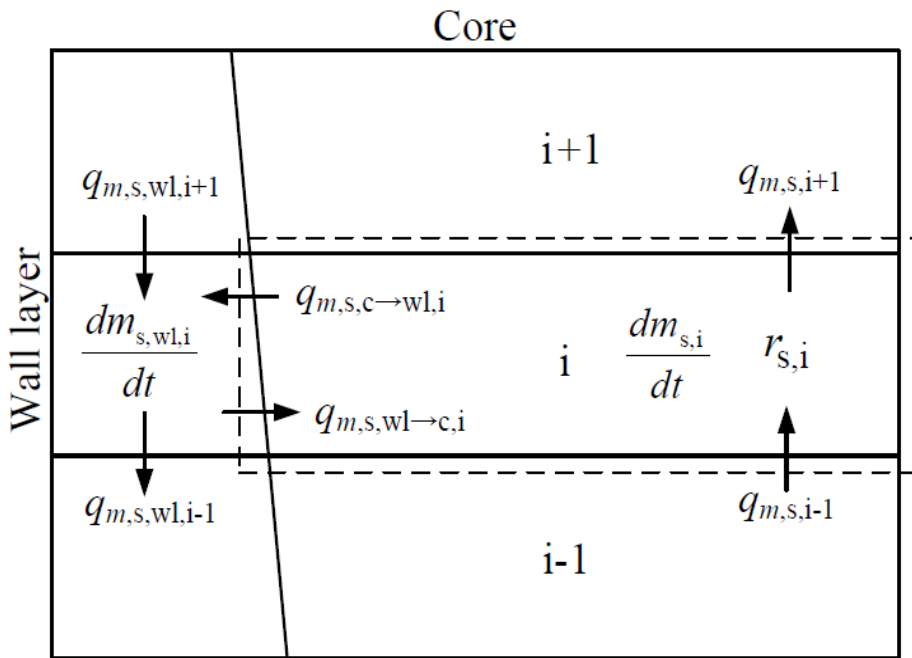


Figure 5.4. Mass balance flows and variables for a single mesh cell.

Equation 5.3 represents the mass flow rate incoming in the mesh cell, which is the sum of the mass flow rate from wall layer to the core and the mass flow rate from the previous mesh cell to the current. Equation 5.4 represents the mass flow rate outgoing from the control volume, which is the sum of the mass flow rate from the reactor core to the wall layer and the mass flow rate leaving from the current control volume to the next one.

$$\frac{dm_{s,i}}{dt} = \sum q_{m,s,in,i} - \sum q_{m,s,out,i} + r_{s,i} \quad (5.2)$$

$$\sum q_{m,s,in,i} = q_{m,s,i-1} + q_{m,s,wl \rightarrow c,i} \quad (5.3)$$

$$\sum q_{m,s,out,i} = q_{m,s,i+1} + q_{m,s,c \rightarrow wl,i} \quad (5.4)$$

The vertical distribution of solid material, or the density across the length of the reactor was calculated by the Equation 5.5. As discussed previously and explained in chapter 3.4, the density profile in pneumatic transport regime can safely be assumed constant. Thus, a simple average density taken by dividing the total mass concentration with the total volume of the reactor can be utilized, and further included in the calculation of the mass flow rate, Equation 5.6.

$$\rho_{av} = \frac{m_s}{V_{tot}} \quad (5.5)$$

$$qm_{cir} = k (U - u_t) A \rho_{av} \quad (5.6)$$

Where qm_{cir} (kg/s) represents the mass flow rate in the control volume, U (m/s) serves as the gas velocity, u_t (m/s) is the terminal velocity and A (m^2) is the cross-sectional area of the domain. The k serves as a control coefficient set by the user, in order to achieve steady state conditions in desirable operating conditions. In addition, the subtraction of terminal from gas velocity is due to the fact that the slip velocity was assumed to be equal to terminal, thus it can be replaced in the equation above and as a total represent the solid velocity. In this point is important to signalize that the solid velocity can safely be assumed equal to gas velocity, because the terminal is way smaller compared to the other two. However, for less assumptions and higher hydrodynamic accuracy the terminal velocity was included in the equation.

5.5 Gas Mass Balance

The gas mass balance Equation 5.7 was derived and formulated by the help of Figure 5.5. Where, it can be observed that for one control volume and for the whole reactor in consequence, the mass flow rate out is equal to the mass flow rate in from the previous cell, included primary or secondary air feeds in addition with the gas produced from the heterogeneous reactions inside the volume level. Primary airs can be any gas feed from

outside source, for instance the cement kiln flue gas which is utilized in our project. As for the secondary airs, is mostly used to simulate air leaks in the system, or secondary airs intentionally fed in the reactor for smoother fuel combustion.

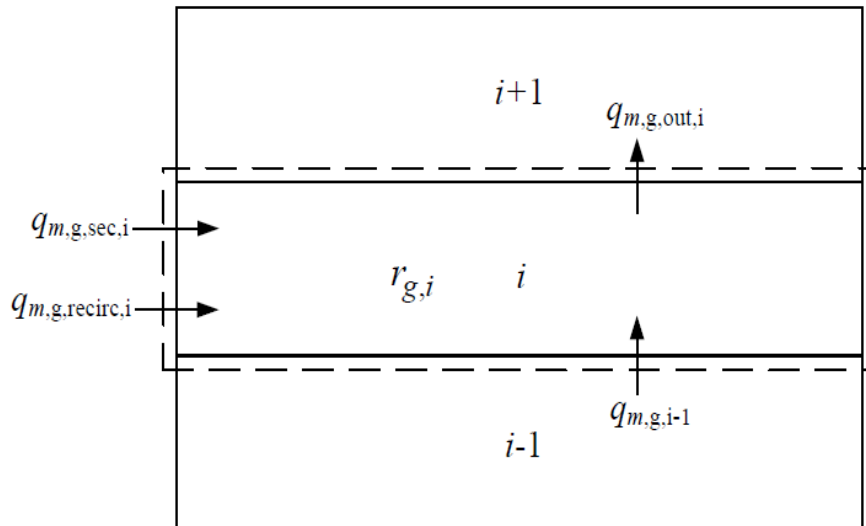


Figure 5.5. Gas mass balance flows and variables for a single mesh cell

$$\begin{aligned}
 \frac{dm_{g,i}}{dt} &= \sum q_{m,g,in,i} - q_{m,g,out,i} + r_{g,i} \Rightarrow \\
 \Rightarrow q_{m,g,out,i} &= \sum q_{m,g,in,i} + r_{g,i} \Rightarrow \\
 \Rightarrow q_{m,g,out,i} &= q_{m,g,i-1} + q_{m,g,sec,i} + q_{m,g,recirc,i} \tag{5.7}
 \end{aligned}$$

In the equation above the gas mass change in time is considered to be zero, because its change rate compared to solid is neglected due to high density difference between the chemical substances (solid density \gg gas density).

5.6 Energy Balance

The importance of an accurate energy balance in calcium looping process and in consequence in our project, is justified by the fact that the steady operation temperature difference between the reactors is crucial for the carbonation-calcination reactions. Thus, precisely predicting the temperature flow between the absorber and regenerator are on the main concern. Furthermore, by considering wall layer and core separately and by assuming full mixing between solids and gas at constant temperature ($T_{solid,i} = T_{gas,i}$), the energy change rate in time for one control volume was formulated as shown in Equation 5.8.

$$\frac{dE_i}{dt} = \sum q_{conv,s} + \sum q_{conv,g} + \sum q_{disp} + \sum q_{ht} + \sum q_{chem} \quad (5.8)$$

where $q_{conv,s}$ [J/s] represents the convective flows of solid, $q_{conv,g}$ is the convective flow of gas, q_{disp} serves as the dispersion between gas-solid, q_{ht} is the representative heat transfer and q_{chem} represents the chemical reactions. The equation is further discretized and solution of each component explained above is occurring. However, demonstration of the full solution is out of the scope of this report. For further information of the energy balance as well for the mass described in previously chapters, one can turn into J. Ylätalo's (2013) dissertation.

5.7 Combustion – Gasification

The combustion model used in the code utilizes the ultimate analysis (C,N,H,S,O) of the fuel and then by proposed correlations from Myöhänen (2011), is separating the volatile, char, ash and moisture release, as shown in the overall model framework at Figure 5.6. In addition, the lower heating value is being calculated from the current calculations and then is compared with the theoretical LHV (manually inputted by the user) with the purpose of evaluating the formation enthalpy of volatiles, in order to keep the energy balance steady. Furthermore, correction of the value is being performed in required cases.

The volatile release reaction handling is based on De-Souza Santos (2010) correlation

$$r_{g,vol,i} = m_{g,vol,i} k_{g,vol,i} \frac{1}{T_i^d} C_{vol,i}^a C_{O2,i}^2 C_{x,i}^c \quad (5.9)$$

where a,b,c,d are empirical coefficients, $m_{g,vol,i}$ serves as the mass of gas in domain, $k_{g,vol,i}$ is the reactions kinetic coefficient and $C_{vol,i}^a$, $C_{x,i}^c$ and $C_{O2,i}^b$ are the representative molar concentration of the volatiles, gas species participating in the reaction and oxygen.

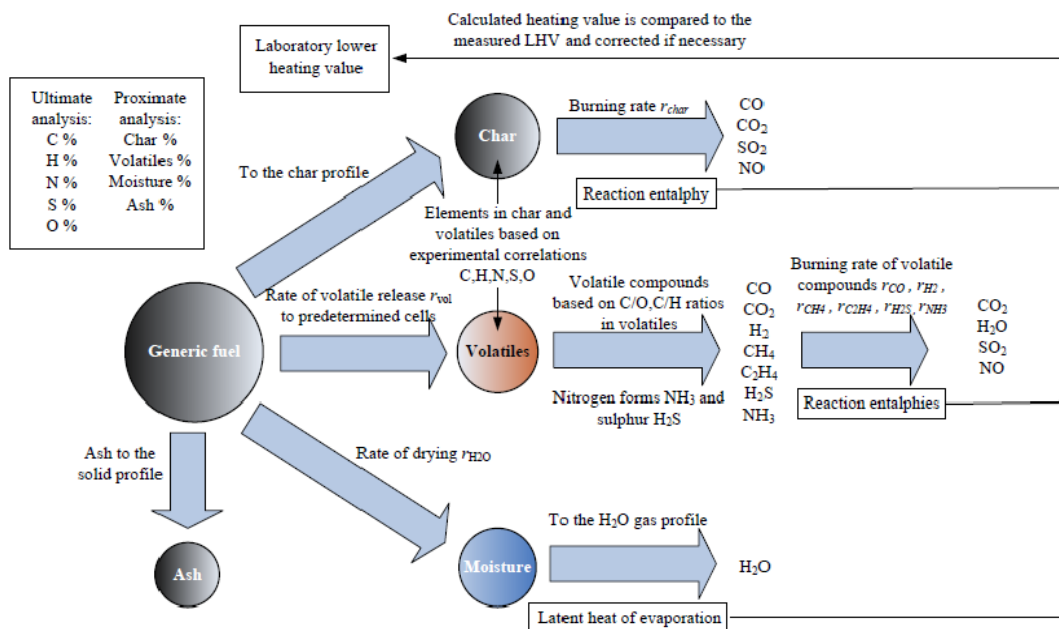
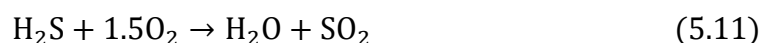
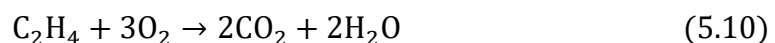
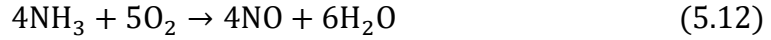


Figure 5.6. Overall schematic of the combustion model, adapted from Sepponen (2017, 56)

In the frame of the CLEANER project, due to heavy oil fuel employed, the combustion model was configured to release zero char, leaving a high percentage of volatile release, with moisture and ash. The volatiles mainly included ethene (C_2H_4), hydrogen sulphide (H_2S) and ammonia (NH_3). In addition, because of the high fraction (95-98 %) of ethene introduced in the volatile release, the fuel is mainly discharging H_2O , CO_2 after the gas combustion reactions, as shown in Equation 5.10. Of course, small percentages of SO_2 are formed in consequence from Equation 5.11, and some NO from the Equation 5.12.





The 1D model included the gasification reactions of Boudouard, water-gas, ethane formation, water-gas shift and steam methane formation. However, due to zero char release the first three reactions are negligible, because they are formed during the char reaction. In consequence, steam methane formation (Equation 5.13) and water-gas shift (Equation 5.14) are the main gasification reactions utilized for the specific fuel feature. Adding, the formation of methane from the volatiles was nearly to zero, thus the influence of it was nearly negligible as well. Concluding, all in all water-gas shift reaction can be considered as the main gasification reaction effecting the simulation and code.



The reaction rate employed in code level for the water-gas shift was based on Gomez-Barea and Leckner (2010) correlation

$$r_{wgs} = a_{wgs} 2.78 \exp\left(-\frac{1515.46}{T}\right) \left[C_{\text{CO}} C_{\text{H}_2\text{O}} - \frac{C_{\text{CO}} C_{\text{H}_2\text{O}}}{0.0265 \exp\left(\frac{8956}{T}\right)} \right] \quad (5.15)$$

where $C_{\text{H}_2\text{O}}$ serves as the molar concentration of water vapor (mol/m^3), and C_{CO} is the molar concentration of carbon. In consequence, a_{wgs} stands for 1D model user control parameter (coefficient), which is configured according the case with some freedom from the user, in order to operate the code at desirable condition.

5.8 Sorbent reactions

The sorbent reactions included in the code were calcination, carbonation, direct sulphation and desulphation. Calcination and carbonation are extensively discussed in previous chapters (Chapter 2 and 4). As for sulphation and desulphation, there

importance regarding the active sorbent can be found in chapter 4.3, were the first try of modelling the sulphur capture by CaCO₃ was done by Romano (2012). Coming back to our work, all the sorbent reaction rates (kg/s) implemented in the 1D model code level are demonstrated in the Table 5.1 below. Furthermore, explanation of each variable can be found in Table 5.2.

Table 5.1. Sorbent Reaction Rates Equations applied in 1D model for entrained flow CaL

Calcination, Fang et al. (2009).	$r_{calc} = m_{s,i} k_{calc} W_{CaCO_3}^{\frac{2}{3}} (C_{CO_2,eq} - C_{CO_2})$
Carbonation, Shimizu et al. (1999), Alonso et al. (2009).	$r_{carb,i} = m_{s,i} k_{carb,i} (W_{max} - W_{CaCO_3,i}) (C_{CO_2,i} - C_{CO_2,eq})$
Sulphation, de-Souza Santos (2010).	$r_{sulf,i} = m_{s,i} W_{CaCO_3} k_{sulf,i} w_{SO_2,i} w_{O_2,i}$
Direct sulphation, Myöhänen (2011)	$r_{dirs,i} = a_{dirs,i} m_{s,i} W_{CaCO_3} \exp\left(-\frac{3031}{T}\right) C_{SO_2}^a C_{CO_2}^b C_{O_2}^c A_{mO,CaCO_3} M_{CaCO_3}$
Desulphation, Myöhänen (2011)	$r_{desu,i} = a_{desu,i} m_{s,i} W_{CaSO_4} \exp\left(-\frac{10000}{T}\right) C_{CO} A_{mO,CaSO_4} M_{CaSO_4}$

Table 5.2. Explanation of each variable used in the sorbent reaction rate equations.

k_{calc} , k_{carb} , k_{sulf}	kinetic coefficient for calcination ($\text{m}^3/(\text{kmol s})$), carbonation ($\text{m}^3/(\text{kmol s})$) and sulphation (1/s)
W_{max} , W_{CaCO_3} , W_{CaSO_4} , w_{SO_2} , w_{O_2} (-)	Maximum content of CaCO_3 in the solids, content of CaCO_3 , content of CaSO_4 , SO_2 and O_2
$C_{\text{CO}_2,\text{eq}}$, C_{CO_2} , C_{CO} , C_{SO_2} , C_{O_2} (-)	Equilibrium molar concentration of CO_2 approximated by Silcox et al (1989) (Equation 2.2, Chapter 2.1.1), molar concentration of CO_2 , CO , SO_2 and O_2 .
$A_{\text{mO,CaCO}_3}$, $A_{\text{mO,CaSO}_4}$	Default reaction surface of CaCO_3 (kg/mol), Default reaction surface of CaSO_4 (m^2/kg)
M_{CaCO_3} , M_{CaSO_4}	Molar mass of CaCO_3 and CaSO_4 (kg/mol)
$\alpha_{dirs,i}$, $\alpha_{desu,i}$	control parameters (coefficient) set by the user.

5.9 Boundary Conditions

The importance of the solids balance exchange flow between the reactors and temperature control was mentioned from various researchers (example, J Ylätalo 2012, 135). Achieving the proper temperatures for carbonation and calcination in the relative reactors and maintain the flow balance and constant operation in time, were of the main importance. In addition, due to the reason that the entrained flow 1D model is an interconnected energy system with high sensitivity to different flow rates, the optimal boundaries were selected as shown in Table 5.3 below, based on maximum sorbent capacity of 40 % (X_{max}) and solids recirculation back to carbonator of 20%.

Table 5.3. Selected Boundary Conditions for the entrained flow CaL 1D-Model (Reference case A)

Gas flow entering the calciner (Gas from combustor + air leak)	$(\#25 + \#17) = 1.125 \text{ [kg/s]}$
Raw meal entering the calciner (make up flow + solids from combustor)	$(\#22 + \#25) = 0.849 \text{ [kg/s]}$
Gas flow entering the carbonator	$(\#19) = 0.377 \text{ [kg/s]}$
Flow from calciner to carbonator	$(\#11) = 1.463 \text{ [kg/s]}$
Flow from carbonator to calciner	$(\#13) = 1.034 \text{ [kg/s]}$
Solids purge	$(\#15) = 0.508 \text{ [kg/s]}$
Temperature of solids entering the carbonator	$T = 690 \text{ [}^{\circ}\text{C]}$

6. CALCULATIONS

The purpose of this chapter is to review the results taken from the entrained flow CaL 1D model done for the CLEANER process, for the reference case A boundaries mainly. The chapter begins with the model verification (Chapter 6.1) where results from the 1D model are compared with previous works, with the ambition of verifying that the model works in the proper conditions. In addition, in chapter 6.2 important results are being graphically illustrated and analyzed. Furthermore, for chapter 6.3 a sensitive analysis regarding the kinetic coefficient used in the carbonation reaction was performed. In chapter 6.4, the choking velocity data is being evaluated with the purpose of reassuring that the pneumatic transport will be maintained across the length of the reactor. Finally, chapter 6.5 includes the comparison of all four cases evaluated and simulated from the 1D-Model.

6.1 Model Verification

The verification process includes results from the 1D-CLEANER model developed in the current project in comparison with the solid, gas and energy balances performed and delivered from the previous deliverable (D2.3) for the same pilot plant configuration. Mass flow rates, solid species concentration, gas species concentration and temperature at inlet and outlet, were contrasted with the purpose of demonstrating the accuracy of the 1D-model. In addition, an overall comparison of the main points is being demonstrated below. Table 6.1 contains the results and comparison of the carbonator solids and in Table 6.2 the carbonator gas species are being evaluated. Furthermore, Table 6.3 represents the solids at calciner and Table 6.4 the gas species at calciner.

Table 6.1. Solid Species Comparison in Carbonator.

Solids IN, Carbonator						
	q_m [kg/s]	T [°C]	CaO [w%]	CaCO ₃ [w%]	CaSO ₄ [w%]	Ash [w%]
D2.3	1.848	600.0	55.3	13.6	0.5	30.6
1D Model	1.846	612.7	54.8	14.4	0.3	30.5
Solids OUT, Carbonator						
	q_m [kg/s]	T [°C]	CaO [w%]	CaCO ₃ [w%]	CaSO ₄ [w%]	Ash [w%]
D2.3	1.928	717.5	47.8	22.4	0.5	29.3
1D Model	1.917	719.7	48.4	22.0	0.3	29.4

Table 6.2. Gas Species Comparison in Carbonator.

Gas IN, Carbonator						
	q_m [kg/s]	T [°C]	CO ₂ [vol %]	O ₂ [vol %]	N ₂ [vol%]	H ₂ O [vol%]
D2.3	0,377	600.0	20.0	9.5	67.1	2.6
1D Model	0.377	612.7	19.8	9.7	67.5	3.0
Gas OUT, Carbonator						
	q_m [kg/s]	T [°C]	CO ₂ [vol %]	O ₂ [vol %]	N ₂ [vol%]	H ₂ O [vol%]
D2.3	0.333	717.5	5.1	12.3	78.9	2.8
1D Model	0.343	719.7	7.2	10.4	79.1	3.3

Table 6.3. Solid Species Comparison in Calciner

Solids IN, Calciner						
	q_m [kg/s]	T [°C]	CaO [w%]	CaCO ₃ [w%]	CaSO ₄ [w%]	Ash [w%]
D2.3	1.883	1171.2	32.0	41.0	0.3	26,6
1D Model	1.873	1012.6	33.2	39.7	0.2	26,9
Solids OUT, Calciner						
	q_m [kg/s]	T [°C]	CaO [w%]	CaCO ₃ [w%]	CaSO ₄ [w%]	Ash [w%]
D2.3	1.628	920.0	57.3	11,3	0.5	30,9
1D Model	1.632	879.3	56.8	12,1	0.3	30,8

Table 6.4. Gas Species Comparison in Calciner

Gas IN, Calciner						
	q_m [kg/s]	T [°C]	CO ₂ [vol %]	O ₂ [vol %]	N ₂ [vol%]	H ₂ O [vol%]
D2.3	1.162	1171.2	57.8	4.7	14.6	17.6
1D Model	1.200	1012.6	56.5	5.7	14.6	21.9
Gas OUT, Calciner						
	q_m [kg/s]	T [°C]	CO ₂ [vol %]	O ₂ [vol %]	N ₂ [vol%]	H ₂ O [vol%]
D2.3	1.420	920.0	64.3	4.0	12.4	18.1
1D Model	1.410	879.3	63.8	2.0	12.8	21.3

In the carbonator the comparison analysis showed decent accuracy with differences less than 2.1 %. Mass flow rates, temperatures, solid species concentration and gas species concentration fluctuated the same way with minor concentration disparities. Pointing out, the mixing temperature at the carbonator inlet was measured at 612.7 °C from the 1D model, with comparison of 600.0 °C from the deliverable. The difference is not major, although it can be observed that the CO₂ volumetric % concentration at carbonator outlet diverse in the two cases, where the deliverable shows less concentration (5.1 %) and the 1D model higher (7.2 %). This is occurring, because the

cooler inlet temperatures selected for the deliverable favor the carbonation reaction, creating higher capture at the reactor.

In the calciner the comparison evaluation likewise showed satisfying accuracy with disparities less than 4.3 % in mass flow rates, solid species and gas species concentration. However, the temperature comparison displayed different value ranges. This occurred, due to the fact that the fuel used in the 1D model was not the exact representation of the heavy oil fuel asked from the report. Due to challenges with the 1D model representing fuel without char release, the volatile generation was not precise as well. The solution was to simulate a volatile release with the same C/H ratio of the real fuel volatiles. In addition, the results showed same temperature behavior, with abrupt increase at the bottom of the calciner at ranges of higher than 1000 °C, and gradual temperature decrease along the length of the calciner, due to the endothermic calcination reaction until temperatures of 900 °C approximately at the outlet.

Concluding, the differences between the point cases were minor, and verification can theoretically be assumed. However, direct comparison of the cases is not complete 100 % correct, since the model is providing 1D results and the deliverable reported 0D energy, gas and mass balances. Although, in an interconnected system like the one it was built in the current 1D model, where the reactors are exchanging solids in balance, keeping that flow balance and appropriate temperature difference between the reactors are on the main importance. Thus, if the solid, gas mass flows and the concentration of them are evaluated in the same value range, a satisfying model verification can be achieved for the moment, with the current previous work results available.

6.2 1D Model Results

The motivation upon this chapter is to give a generic idea of the main results taken from the 1D model for entrained flow in calcium looping process under the CLEANER project. The results from the 1D model included four different cases with and without air leak at the end of the carbonator reactor. However, in the current report only reference case A with air leak at the end of the carbonator is being analyzed and priority results are clarified.

6.2.1 Temperature Profile

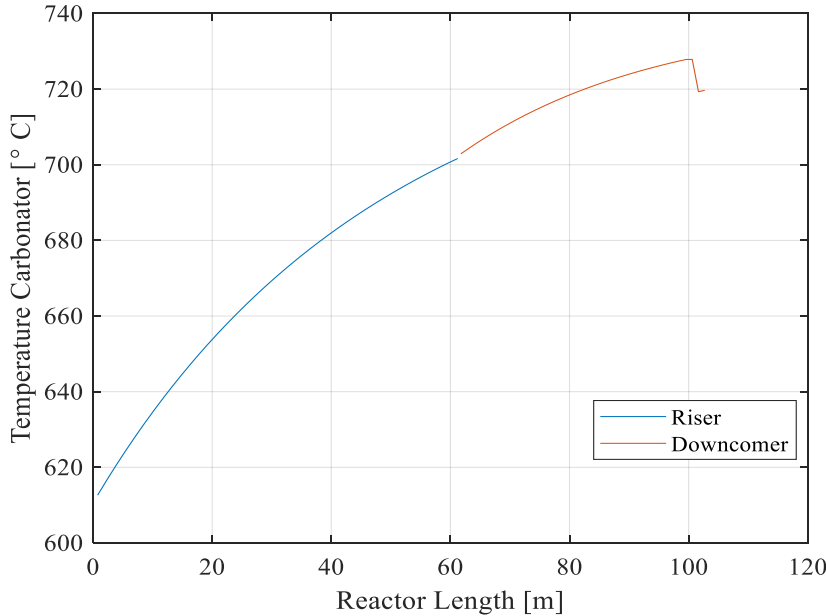


Figure 6.1. Carbonator Temperature Profile [°C] vs Reactor Length [m]

Figure 6.1, represents the temperature at carbonator across the reactor length, where the carbonator inlet temperature or mixing temperature of solids recirculating back to carbonator, cooled solids from calciner and flue gas coming from the cement source, was calculated based on 0D equations performed in a subsystem mixer model implemented in Simulink side. For the reference case A, the mixing temperature was at 612.7 °C which was continuously increasing in the carbonator until 719.7 °C, due to the exothermic carbonation reaction releasing heat to the reactor. In addition, it can be observed a small abrupt decrease of the temperature at the end of the reactor, due to the air leak simulated at the site. Furthermore, at the gooseneck height (61.5 m) the temperature profile starts to behave slightly different (still increasing although), this is occurring because the dimensions of the configuration are changing from the riser to downcomer with increasing inner diameter of the reactor.

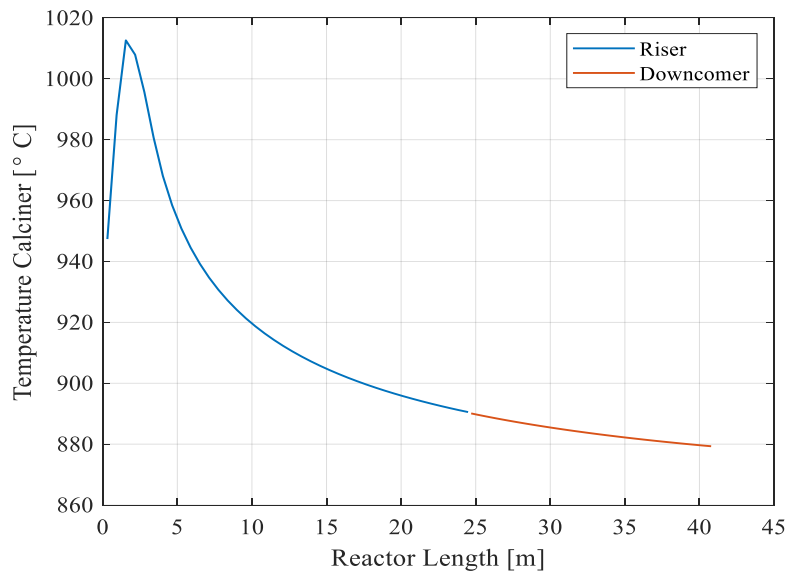


Figure 6.2. Temperature Profile at Calciner [°C] vs Reactor Length [m].

The CLEANER configuration performs combustion of two fuel feeds. One done in an external combustion before the calciner and one at the bottom of the calciner. However, the 1D model used for the process was not able to perform two separately combustions. Thus, the solution was to use the upcoming stream (Solid species, gas species and temperature) after the first combustion from the calculation performed in the previous deliverable as boundary inlet at the calciner.

The results (Figure 6.2) revealed remarkable temperature increase higher than 1000 °C at the bottom of the calciner due to the combustion of the second fuel feed at the site. After the combustion the temperature gradually decreases approximately at 900 °C, due to the endothermic calcination reaction absorbing heat from the system.

6.2.2 Solids Concentration Profile

The solids concentration [kg/m^3] at carbonator and calciner reactor are maintained constant throughout the reactor's height, in order to accurately represent and simulate the desired pneumatic transport phenomena and configuration of the system. From the

Figure 6.3 and Figure 6.4, it can be observed that the equation (Equation 5.5) implemented in code level is successfully maintaining the desired constant solids concentration.

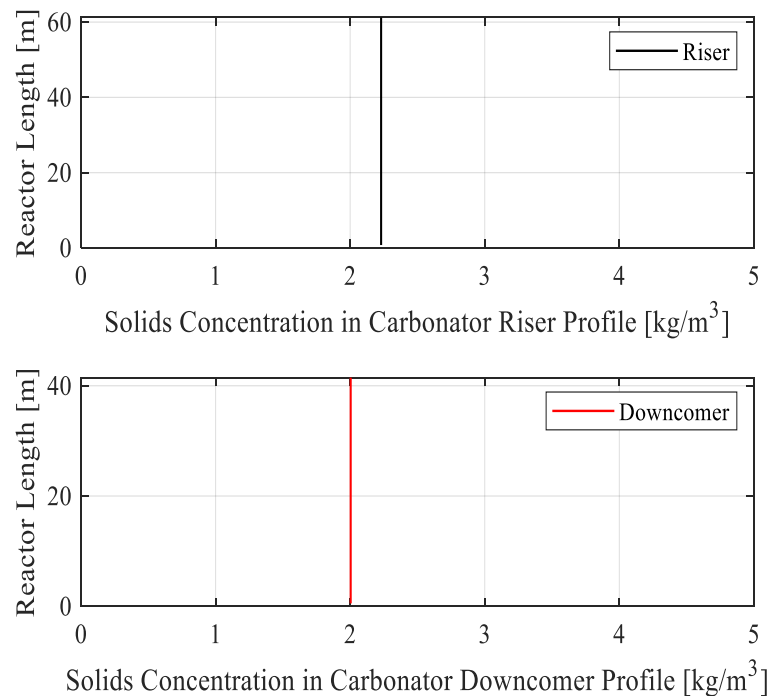


Figure 6.3. Solids Concentration at Carbonator [kg/m³] vs Reactor Length [m]

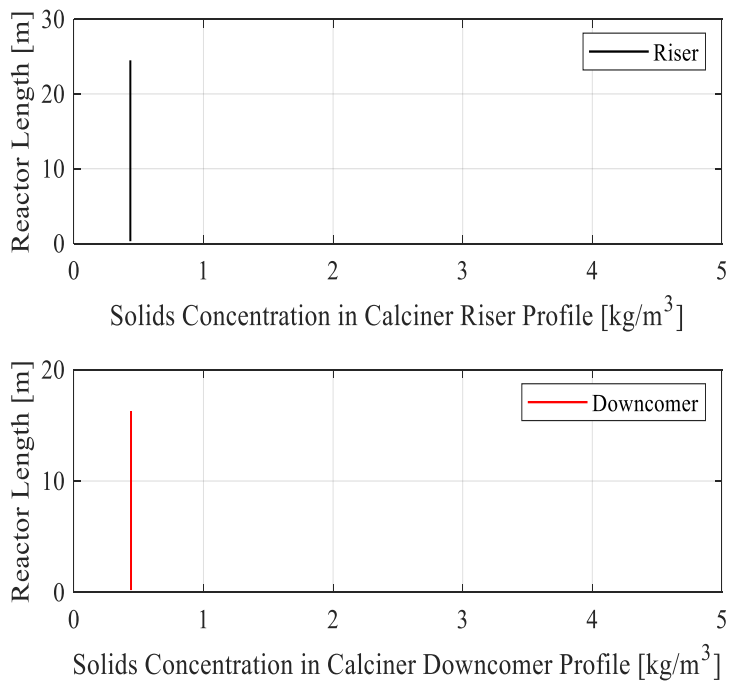


Figure 6.4. Solids Concentration in Calciner [kg/m^3] vs Reactor Length [m]

6.2.3 Carbonation-Calcination Reactions Rate

The carbonation and calcination reactions rate were calculated based on the correlations presented in the Table 5.1 and Table 5.2. The carbonation reaction as shown in Figure 6.5 below is decreasing across the length of the absorber. Mainly, this occurred because the CO_2 concentration likewise decreased. Secondly, the temperature across the length is increasing and approaching the equilibrium curve of Silcox et al (1989), which was demonstrated in Figure 2.3 of the chapter 2.1.1, which makes the reaction less effective. Thus, higher carbonation reaction rate is expected at the bottom of the carbonator, where temperatures are cooler and CO_2 concentration higher. Furthermore, in the gooseneck site at 61 meters a small jump of the reaction occurred. The increased inner diameter after the gooseneck bend mathematically created less concentration of solids per m^3 as it can be seen from Figure 6.3 as well, thus the minor jump occurred since the reaction depends on the CaCO_3 concentration per m^3 . Concluding, the carbonation reaction is also being affected by the calcination-carbonation loops number and how much active is the sorbent undergoing the reaction (See Chapter 2.2).

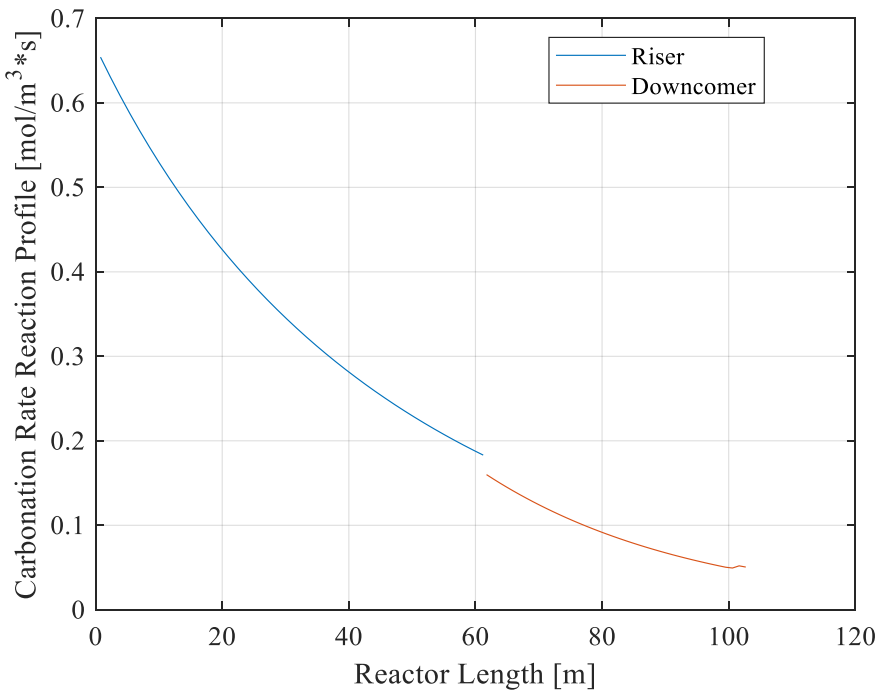


Figure 6.5. Carbonation Rate Reaction [mol/m³ s] vs Reactor Length [m]

The calcination reaction rate as it can be examined from the Figure 6.6 is abruptly increasing in the bottom of the calciner where the temperature as well rises in high values of higher than 1000 °C, due to the second fuel feed combustion. First, the high temperature at the point favors the equilibrium curve at the calcination side, which creates high calcination reaction rate at the point. Secondly, the high concentration of CaCO₃ solids at the inlet of the calciner support the calcination reaction likewise. Furthermore, the reaction decreases as the endothermy of it, absorbs heat from the system and its effectiveness reduces across the length, with the additional CaCO₃ weight fraction loss.

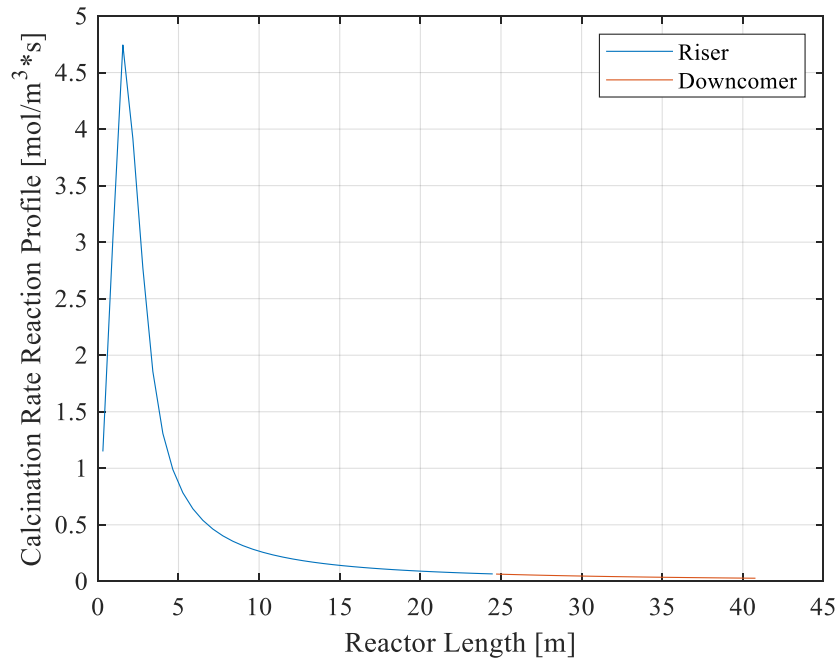


Figure 6.6. Calcination Rate Reaction [mol/m³ s] vs Reaction Length [m].

6.2.4 Fluidizing Gas Velocity

The gas fluidizing velocity was calculated in C code level by the Equation 6.1, shown below. Where R [kJ/kmol K] is the universal constant for ideal gas law, $A_{et,i}$ [m²] serves as the cross sectional area at the top edge of the control volume, $A_{el,i}$ [m²] represents the cross sectional area at the lower edge of the control volume, $M_{g,i}$ [kg/kmol] is the total molar mass of the flue gas at the domain, p [Pa] is the pressure at the control volume and finally $d_{p,i}$ [Pa] represents the solid pressure at the element.

$$U_i = \frac{q_{m,gas,tot,i-1} R (T_i + 273.15)}{\frac{A_{et,i} + A_{el,i}}{2} M_{g,i} (d_{p,i} + p)} \quad (6.1)$$

Figure 6.7 represents the fluidizing gas velocity at the riser of the carbonator. The velocity maintains a constant of 16 m/s across the height of the riser as intended from the volumetric gas flow sent to the carbonator inlet. In addition, from Figure 6.8, the velocity after the gooseneck bend reduced at 9.1 m/s at the downcomer section, firstly

due to the expansion of the inner diameter of the reactor, which contributed with larger values of cross-sectional areas in the Equation 6.1 and secondly due to opposite gravity influencing the hydrodynamics

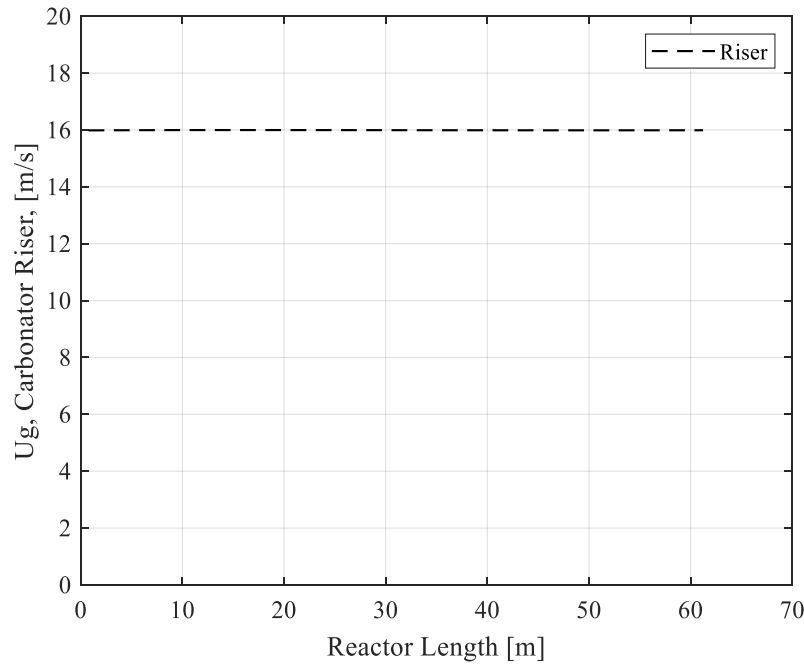


Figure 6.7. Carbonator Riser Fluidizing Gas Velocity [m/s] vs Reactor Length [m]

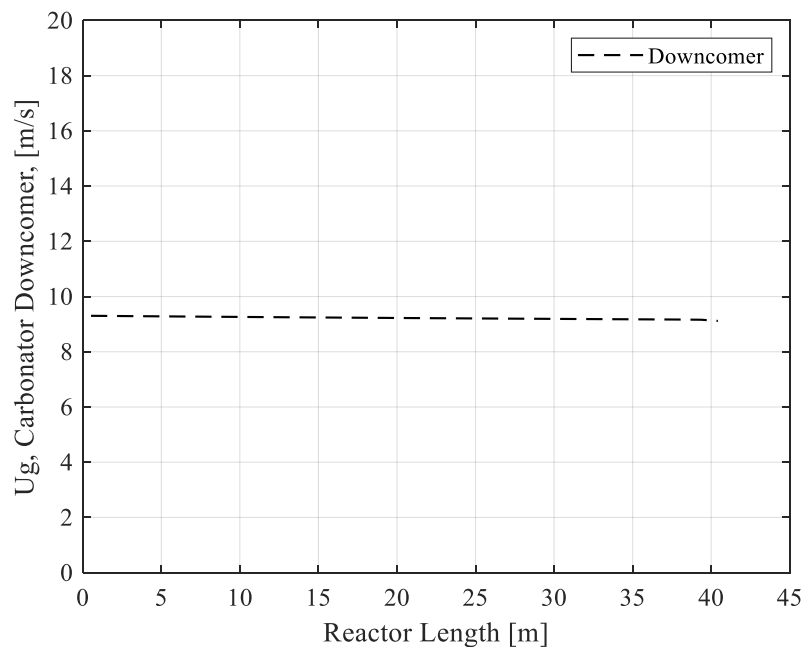


Figure 6.8. Carbonator Downcomer Fluidizing Gas Velocity [m/s] vs Reactor Length [m].

The fluidizing gas velocity in calciner can be studied from the Figure 6.9. The fluidizing velocity increased in the first 3-5 meters for two main reasons. First, due to the large temperature expansion at the bottom of the calciner. Secondly, due to the gas mass flow rate [kg/s] increase, both reasons affect the Equation 6.1 significantly. Furthermore, the velocity maintains constant value of 11.3 m/s and slight decrease of it until 11.1 m/s, resulted from the smooth temperature decrease across the length.

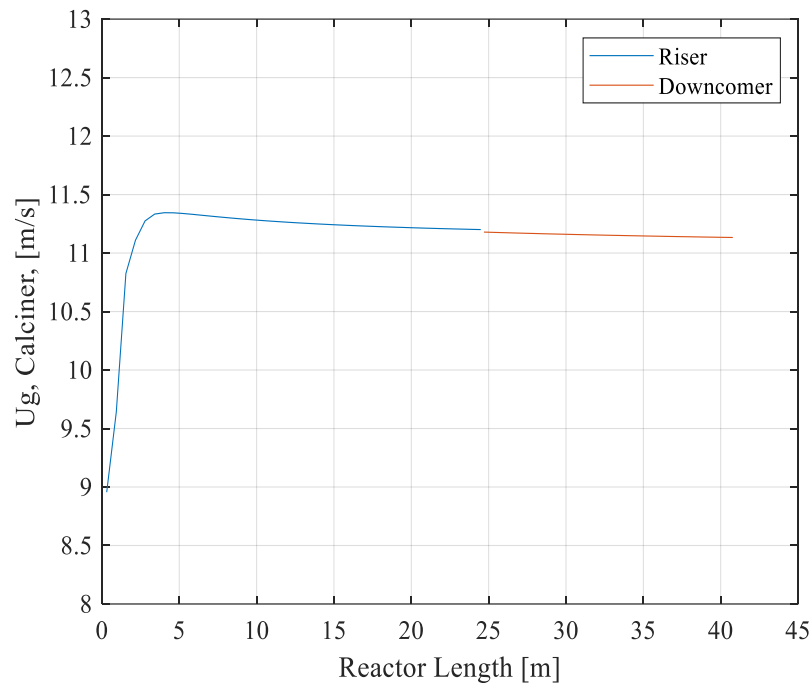


Figure 6.9. Calciner Fluidizing Gas Velocity vs Reactor Height.

Under pneumatic transport regime, as explained in chapter 3.4.2, slip velocity can safely be assumed to be equal with the terminal. In addition, since the terminal velocity in the case is very small mainly because of the low solid bulk density and low mean particle diameter, the solid velocity is almost equal to the gas velocity.

$$\begin{aligned}
 u_g &= u_{solids} + u_{slip} \Rightarrow \\
 \Rightarrow u_g &= u_{solids} + u_{terminal}, \quad \text{where } u_{terminal} \approx 0.005 \frac{m}{s} \Rightarrow \\
 \Rightarrow u_g &\approx u_{solids} \tag{6.2}
 \end{aligned}$$

6.2.5 Solids (CaCO_3 , CaO) Profile

The solids mass fraction derivative of CaCO_3 in code level was calculated as shown in Equation 6.3. Where $\text{CaCO}_3_{\text{cir}}$ represents the solid fraction coming inside the control volume from the circulation, $\text{CaCO}_3_{\text{wl}}$ serves as the fraction ‘transferred’ from the wall layer to the core of the reactor in domain level, $\text{CaCO}_3_{\text{in}}$ is the fraction from the previous control volume, $\text{CaCO}_3_{\text{out}}$ is the fraction exiting the current control volume, CaCO_3_{r} is the source fraction obtained by the carbonation, calcination and direct sulphation reactions, S_r is the total reaction affecting the solids and finally $m_{s,i}$ represents the total mass of the control volume. In addition, the derivative of the solid fraction for CaO and gas fractions of CO_2 , O_2 , N_2 and H_2O are being calculated with the same equation logic. For simplicity and compression of the thesis, the equation derivatives of the mentioned are not presented in the current report.

$$\begin{aligned} dX\text{CaCO}_3,i \\ = \frac{\text{CaCO}_3_{\text{cir}} + \text{CaCO}_3_{\text{wl}} + \text{CaCO}_3_{\text{in}} - \text{CaCO}_3_{\text{out}} + \text{CaCO}_3_{\text{r}} - X\text{CaCO}_3,i * S_r}{m_{s,i}} \end{aligned} \quad (6.3)$$

In the results for the reference case A as shown in Figure 6.10, the CaCO_3 mass fraction in the carbonator increases across the length from 14.4 % to 22.0 % due to the carbonation reaction absorbing CO_2 and in consequence CaO material carbonates into CaCO_3 . On the other hand, the CaO mass fraction decreases from 54.8 % to 48.4 % due to the same reason mentioned above.

Figure 6.11 represents the solid fraction at the calciner, where with comparison from the carbonator, the calcination reaction increases the CaO fraction and decreases the CaCO_3 releasing CO_2 to the system. Furthermore, from the profiles it can be observed that most of the calcination reaction is occurring at the bottom of the calciner due to higher temperatures and CaCO_3 concentration at the site.

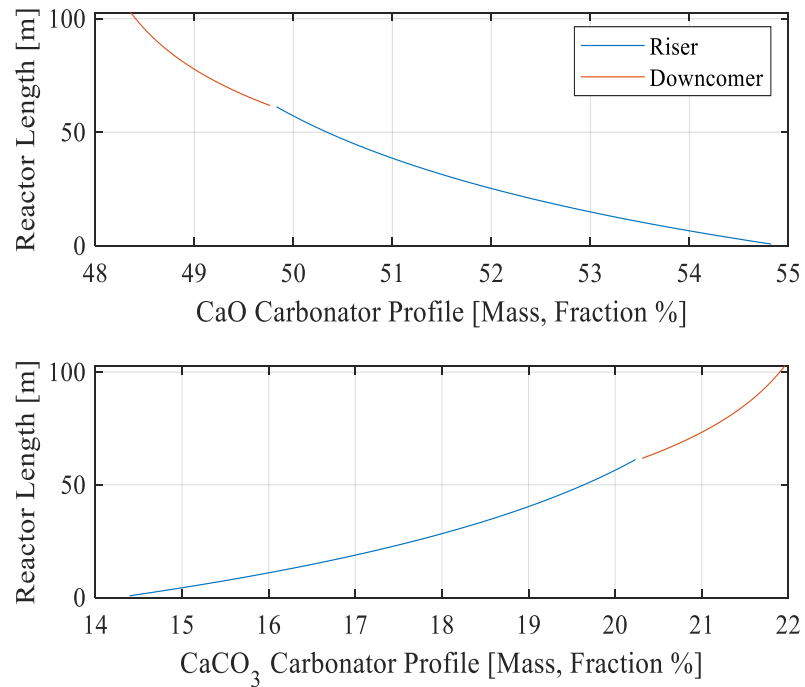


Figure 6.10. CaCO₃ and CaO Carbonator Mass Fractions [%] vs Reactor Length [m].

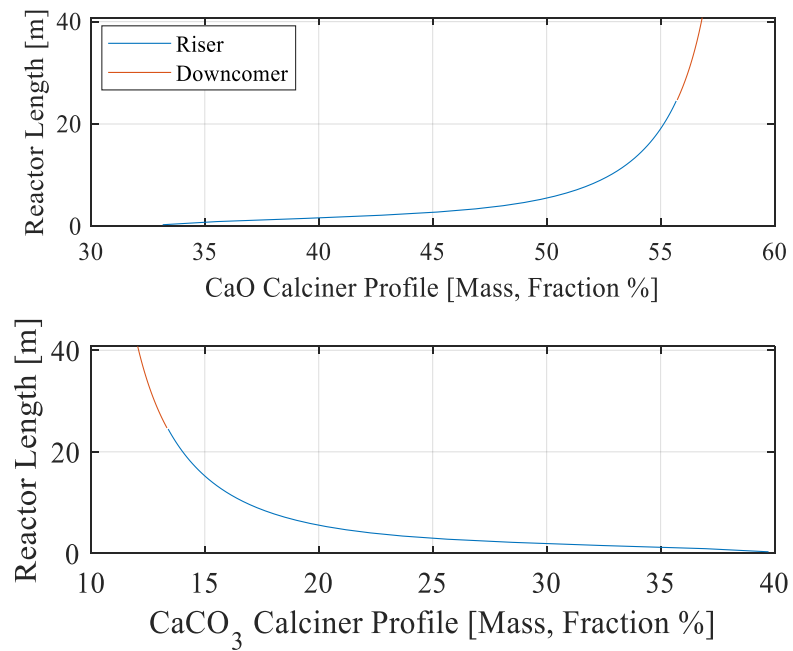


Figure 6.11. CaCO₃ and CaO Calciner Mass Fractions [%] vs Reactor Length [m].

6.2.6 Flue Gas Profiles (CO_2 , O_2 , H_2O , N_2)

Figure 6.12 represents the main flue gas species in molar fraction of percentage existing in the carbonator. In addition, due to no combustion of fuel in the specific reactor, four main gas species were taken into consideration. From the graph below, it can be observed that the CO_2 % molar gradually decreases across the length, because of the carbonation reaction. The abrupt decrease of the gas species in percentage molar concentration in the end of the reactor occurred due to the simulated air leak. The O_2 and H_2O concentration [kg/m^3] increased, however in the graph since the N_2 % concentration mathematically occupies the 78 % of the incoming air, the O_2 and H_2O percentage molar concentration will decrease.

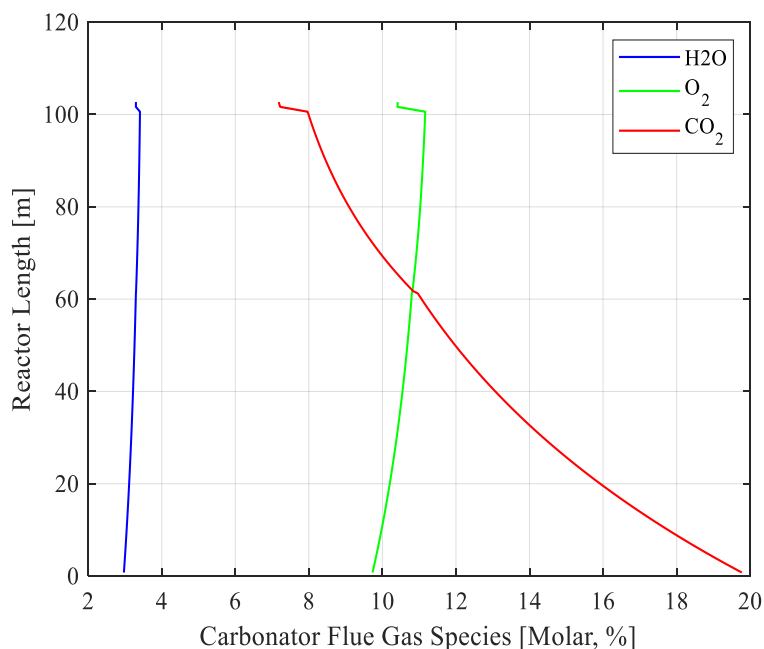


Figure 6.12. Carbonator Flue Gas Species vs Reactor Length.

For the calciner, as shown in Figure 6.13, the CO_2 increased from 56.5 % to 63.8 % in the first 5 to 10 meters of the reactor, due to the combustion and calcination reactions mainly and effectively reacting at the site. In addition, after the 20 meters, CO_2 molar % concentration remains close to constant values until the end of the reactor, due to the deficiency of the calcination reaction. In addition, O_2 is decreased due to the consumption of it for full burning in the combustor. N_2 and H_2O remain constant

throughout the height, with minor fluctuation in the bottom, due to the air leak. Concluding, all the combustion reactions included and taken place in the code level are explained in the chapter 5.7. In addition, exact percentages of the solids and gas species in the inlet and outlet of the reactor can be seen from chapter 6.1 where the verification of the model was implemented.

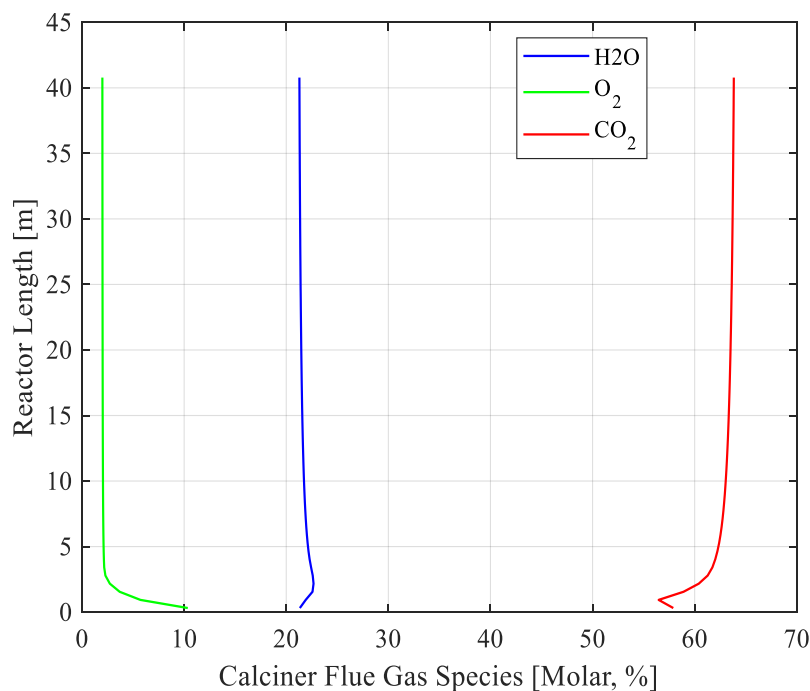


Figure 6.13. Calciner Flue Gas Species vs Reactor Length

6.3 Sensitive Analysis in Kinetic Coefficient of Carbonation.

As explained in chapter 5.8 the carbonation reaction rate was taken by the adjusted correlation adapted from Shimizu et al. (1999) and Alonso et al. (2009) (Table 5.1). In addition, the equation includes kinetic coefficient (k_{carb}) which can be selected from the user to match the desired operation. Under the entrained flow CaL 1D-Model the coefficient was adjusted at value of $24 \text{ [m}^3/(\text{kmol s})$ for the reference case A, to match the predicting operation of the Vernasca pilot plant and finally achieve accurate temperature, solids and gas profiles across the length of the reactor.

The motivation upon this chapter is to demonstrate the sensitive analysis done and why the specific kinetic coefficient was selected. Furthermore, temperature and CO₂

concentration profile are also being analyzed for different k_{carb} values ranging from 20 to 100, with the purpose of understanding how the specific carbonation reaction rate equation behaves under the entrained flow CaL 1D Model.

Figure 6.14 demonstrates the temperature variation with different k_{carb} values, as well Figure 6.15 displays the CO₂ vol [%] concentration profile ranging. The temperature indicated increased values with higher escalation of k_{carb} numbers. This mainly occurred because with higher kinetic coefficient the exothermic carbonation reaction inside the reactor will likewise increase, releasing heat in the system. Furthermore, from Figure 6.15, it can be displayed that the CO₂ vol (%) concentration profile decreased with higher kinetic coefficient, due to the increased carbonation reaction rate absorbing carbon dioxide. Added, from both figures it can be observed that after k_{carb} value of 60, the carbonation reaction rate becomes faster in the first 40 meters of the reactor length and after a slower reaction occurs until the end of the reactor. This primarily occurred because the higher carbonation rate will consume most of the active sorbent in the first meters.

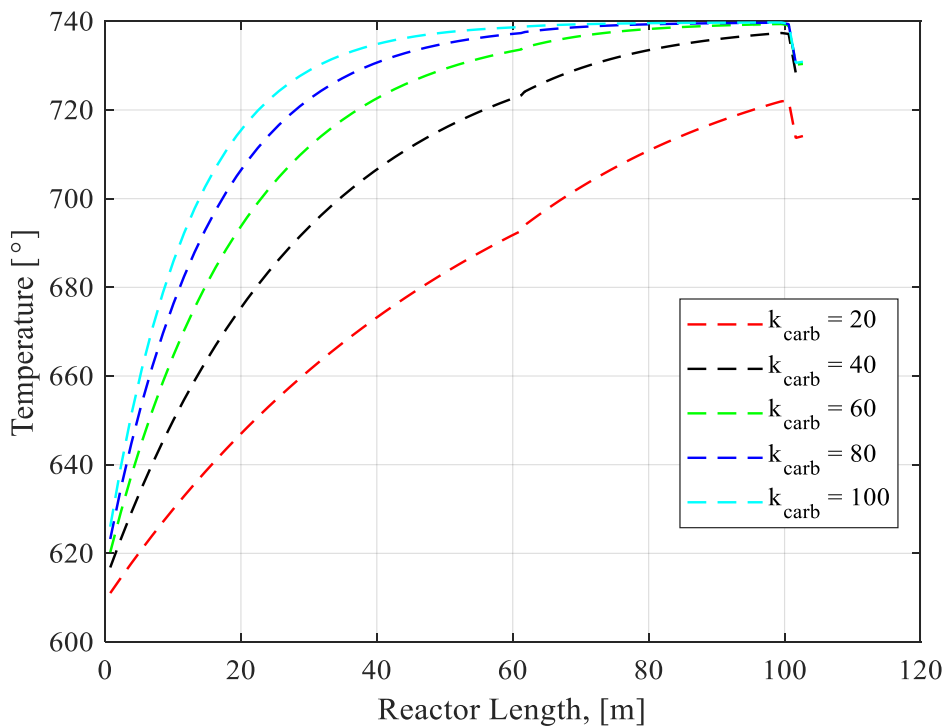


Figure 6.14. Temperature [°C] variation with different kinetic coefficient [$\text{m}^3/(\text{kmol s})$] values

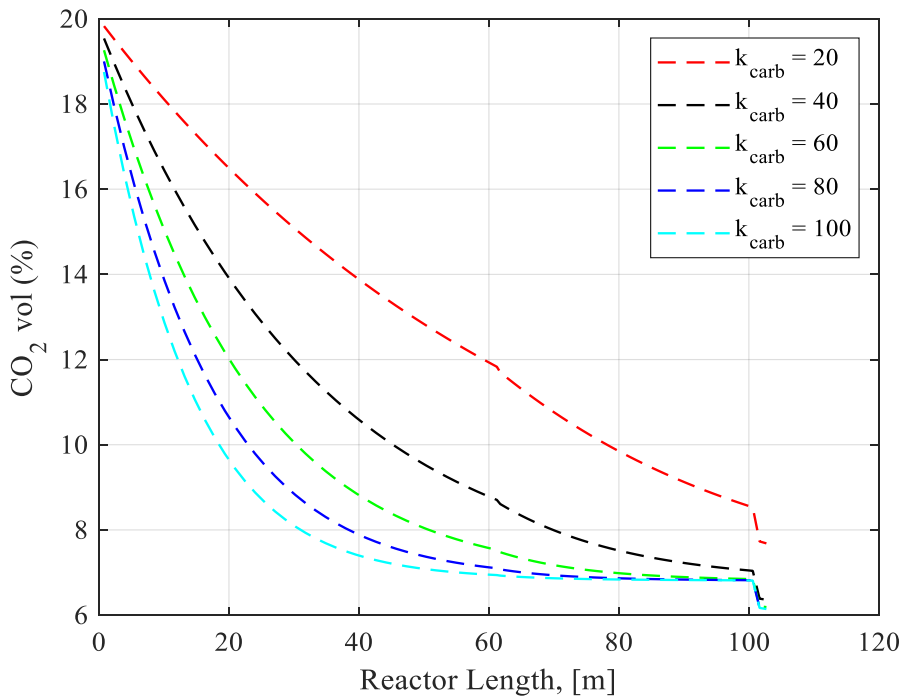


Figure 6.15. CO₂ vol (%) profiles with different kinetic coefficient [m³/(kmol s)] values.

6.4 Pilot Plant Operation with Air Leakage and without

During the pilot plant operation, air leaks in the carbonator are expected or are likely to occur in different lengths. First, in the beginning of the reactor due to the joints. Secondly, in the measurement holes along the length of the reactor, and lastly in the outlet of the reactor due to the lower pressure existence at the point. In the boundaries of this simulation and report, the outlet leakage of 0.036 kg/s was simulated, evaluated and further analyzed.

6.4.1 Temperature Differences

The temperature evaluation showed slight reduction of the temperature across the length of the reactor, during operation with air leak, as shown in Figure 6.16. The decreased temperature is explained due to the cold income flow of the environmental temperature, of usually 25 °C, which deescalated the fundamental conservation equations of mass and energy.

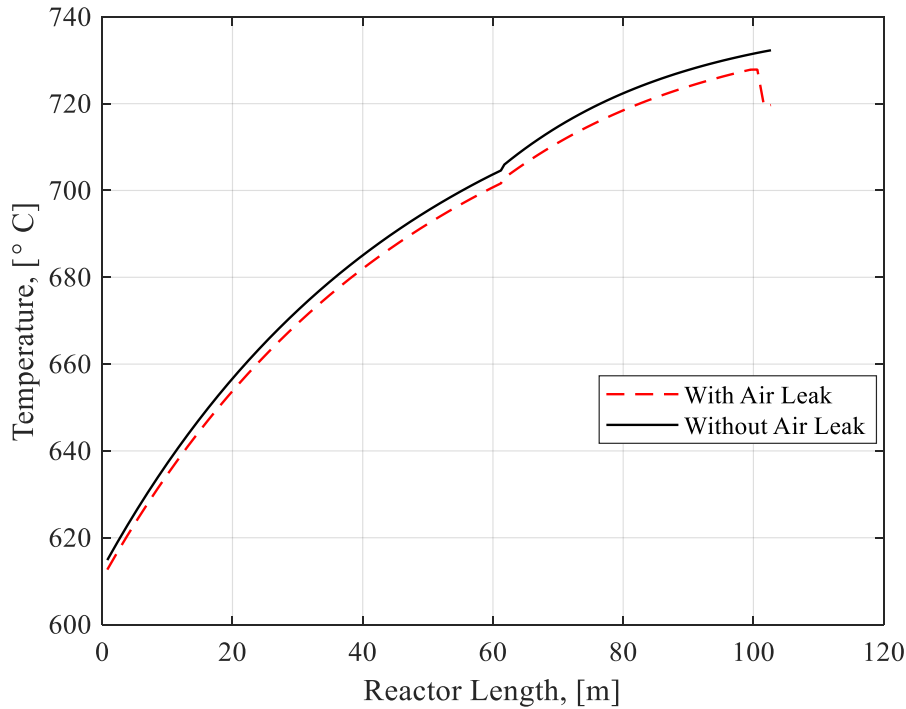


Figure 6.16. Temperature profile comparison between air or without air leakage during pilot plant operation.

6.4.2 CO₂ Capture Efficiency

The CO₂ capture efficiency was calculated by the Equation 6.4, demonstrated below. Where $qm_{CO_2,in}$ [kg/s] is the mass flow rate of carbon dioxide in the first element and $qm_{CO_2,out}$ [kg/s] serves as the mass flow rate of CO₂ in the outlet. In the results, as shown in Figure 6.15 the CO₂ capture efficiency with air leak showed slight reduction, likewise with temperature. The additional incoming air contained large molar fraction of O₂ and N₂ mainly, which affected the total volumetric percentage fraction of CO₂ existing in the reactor. Thus, with lower fraction of carbon dioxide, the total mass flow rate of it decreased and in consequence negatively affected the overall CO₂ capture efficiency.

$$CO_{2,capture,eff} = \frac{qm_{CO_2,in} - qm_{CO_2,out}}{qm_{CO_2,in}} \quad (6.4)$$

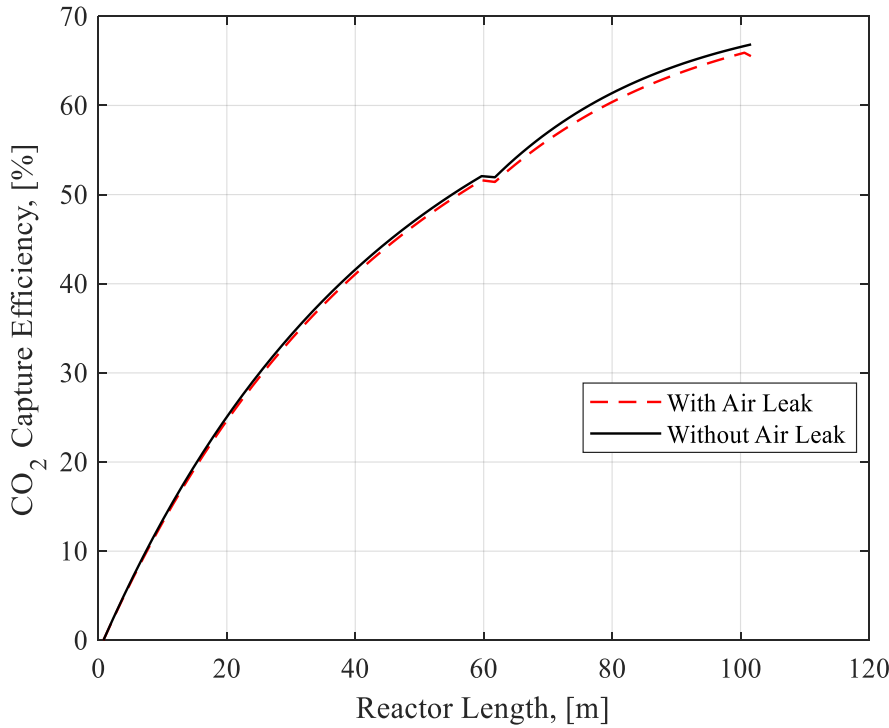


Figure 6.17. CO₂ Capture efficiency profile comparison with air and without air leakage during pilot plant operation.

6.5 Choking Velocity

In this chapter the choking velocity is being demonstrated and further analyzed, for comparison purposes with the fluidizing flue gas velocity, in order to reassure that the pneumatic transport is maintained across the length of the reactors. In addition, many correlations exist to calculate the specific variable, but most of the equations were formulated based on the researcher's specific design he/she was working on. Thus, selecting choking velocity correlation needs to be done with appropriate knowledge and understanding of your system's hydrodynamic operation and structural design. In addition, after comparing various correlations, the velocity was finally calculated based on Punwani (1976) Equation (6.5) and (6.6), which were proven to give the largest and best matching numbers compared to other authors.

$$\frac{u_{g,ch}}{\varepsilon_{g,ch}} - u_t = \frac{\frac{\dot{m}_s}{A}}{\rho_s (1 - \varepsilon_{g,ch})} \quad (6.5)$$

$$\rho_g^{0.77} = \frac{2250 D (\varepsilon_{g,ch}^{-4.7} - 1)}{\left(\frac{u_{g,ch}}{\varepsilon_{g,ch}} - u_t\right)^2} \quad (6.6)$$

Where $u_{g,ch}$ [m/s] serves as the choking velocity, $\varepsilon_{g,ch}$ [-] as the voidage where choking occurs, u_t [m/s] represents the terminal velocity, m_s [kg/s] is the mass flow rate of solids, ρ_s [kg/m³] is the density of the solids, A [m²] represents the cross sectional area, ρ_g [kg/m³] is the gas density and D [m] serves as the inner diameter of the reactor.

The calculations were done in a separately matlab environment model, in which the values of the mass flow rate, density of gas and length of the reactor for each control volume were loaded from the 1D model results. All the other variables were selected based on the same values that were implemented in the main code likewise. In addition, the Equations (6.5) and (6.6) were both formulated to represent the equality of choking velocity and based on selected error difference between $u_{g,ch,1,1}$ and $u_{g,ch,1,2}$ for $\varepsilon_{g,ch}$ loops, the code was converged at $u_{g,ch,1,1}$ equal to $u_{g,ch,1,2}$ at appropriate voidage and desired error difference. In addition, the results for the reference case A are demonstrated below.

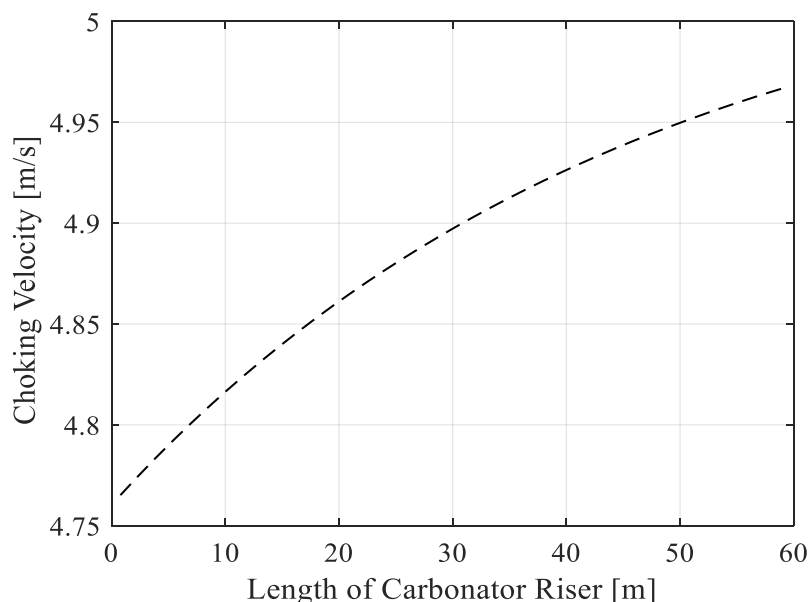


Figure 6.18. Length of Carbonator Riser vs Choking Velocity

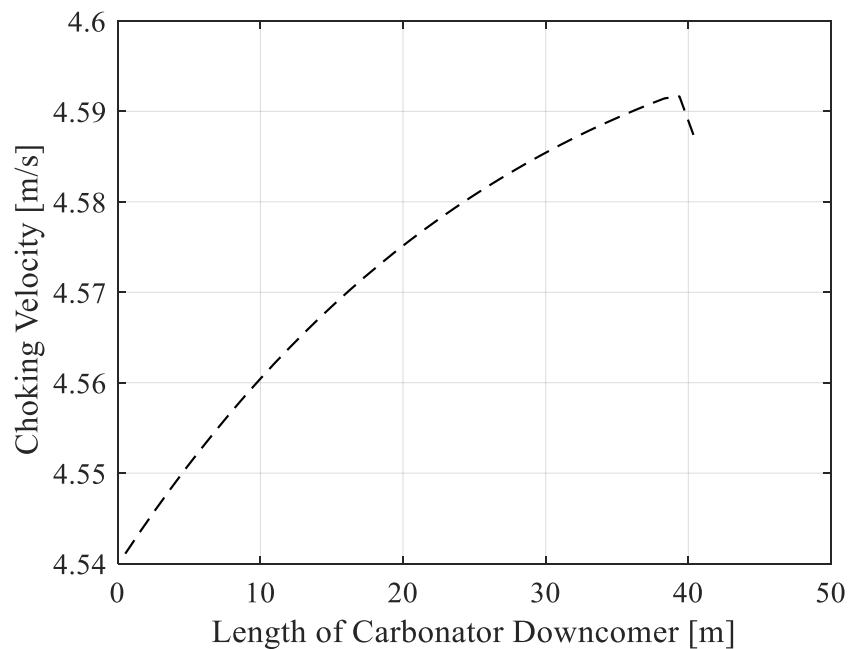


Figure 6.19. Length of Carbonator Downcomer vs Choking Velocity

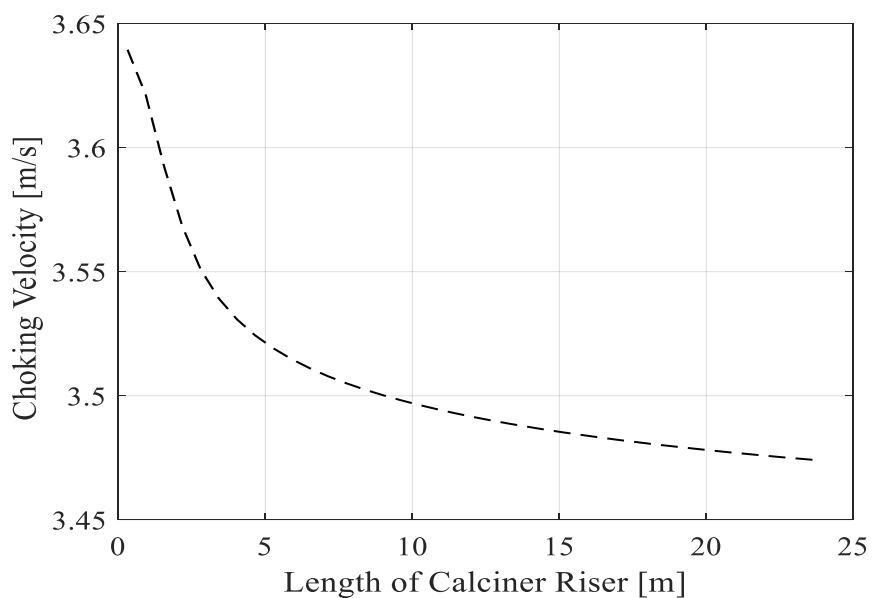


Figure 6.20. Length of Calciner Riser vs Choking Velocity

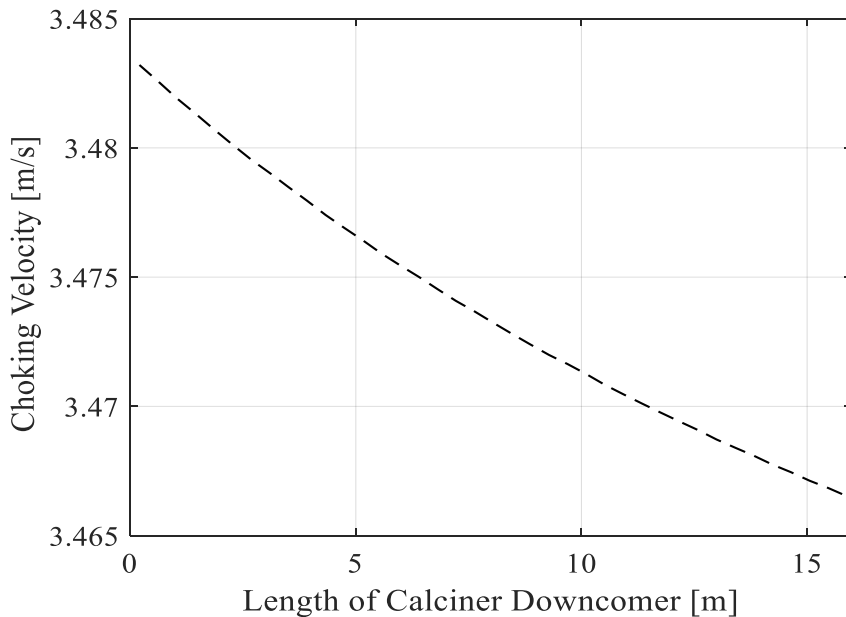


Figure 6.21. Length of Calciner Downcomer vs Choking velocity

Figure 6.18 and Figure 6.19 represent the choking velocity at the riser and downcomer of the carbonator respectively. In addition, the choking velocity at the carbonator is gradually increased from the bottom of the reactor to the end of the riser. This occurred because the carbonation reaction absorbs carbon dioxide and the concentration of solids inside the reactor increased creating higher mass flow rate, which impacts the Equations (6.5, 6.6). In addition, the velocity in the gooseneck section abruptly dropped from 4.9 m/s to 4.5 m/s due to the large diameter expansion of the system's configuration. The inner diameter of the downcomer increases, creating more space for the solids to travel in pneumatic transport, thus the possibility of accumulation choking to occur decreases.

Figure 6.20 and Figure 6.21 represent the choking velocity at the riser and downcomer of the calciner respectively. Where the choking velocity sharply decreased in the first 5 meters of the calciner and then gradual decline was developed until the end of the calciner. The abrupt decrease in the beginning is caused due to the fast calcination reaction happening at the bottom of the reactor. Calcium carbonate solids are releasing CO₂ species, and the concentration of solids in the system is decreasing, in consequence accumulation choking probability occurrence likewise.

Concluding, the choking velocity evaluated by implemented Punwani's (1976) correlation, compared to Figure 6.7 , Figure 6.8 and Figure 6.9 where the fluidizing gas velocity across the length was demonstrated, showed that the pneumatic transport will safely be maintained in the reactors, for the specific operational condition of the reference case A with air leakage at the end of the carbonator.

6.6 Comparison Between the Four Different Cases.

The motivation upon this chapter is to analyze and demonstrate all four cases evaluated from the entrained flow 1D-model developed in this project and compare various results. The important boundary conditions and differences between the cases are showed in Table 6.5. In Figure 6.22, the carbon dioxide capture efficiency across the length of the carbonator reactor is being displayed. In addition, Table 6.6 demonstrates the cases results of the power in the calciner reactor, CO₂ capture efficiency and mass flow rate at the carbonator outlet.

Table 6.5. Boundary Conditions variations between cases

Case	A	B	C	D
X _{max} [%]	40	20	40	20
Recirculation of solids back to Carbonator [%]	20	40	20	40
q _{mf} [kg/s]	0.038	0.038	0.042	0.042
Make-up flow [kg/s]	0.812	0.812	1.194	1.194
Temperature of solids from calciner to carbonator. [°C]	690	700	690	700

Table 6.6. Power at the calciner, mass flow rate of solids and CO₂ capture efficiency at the carbonator outlet, 1D-model results for each case.

Case	A	B	C	D
Power [KW]	2418.6	2450.2	3104.1	3131.7
q _m [kg/s]	1.92	2.52	2.24	2.95
CO ₂ capture [n-%]	65.46	45.96	69.96	46.93

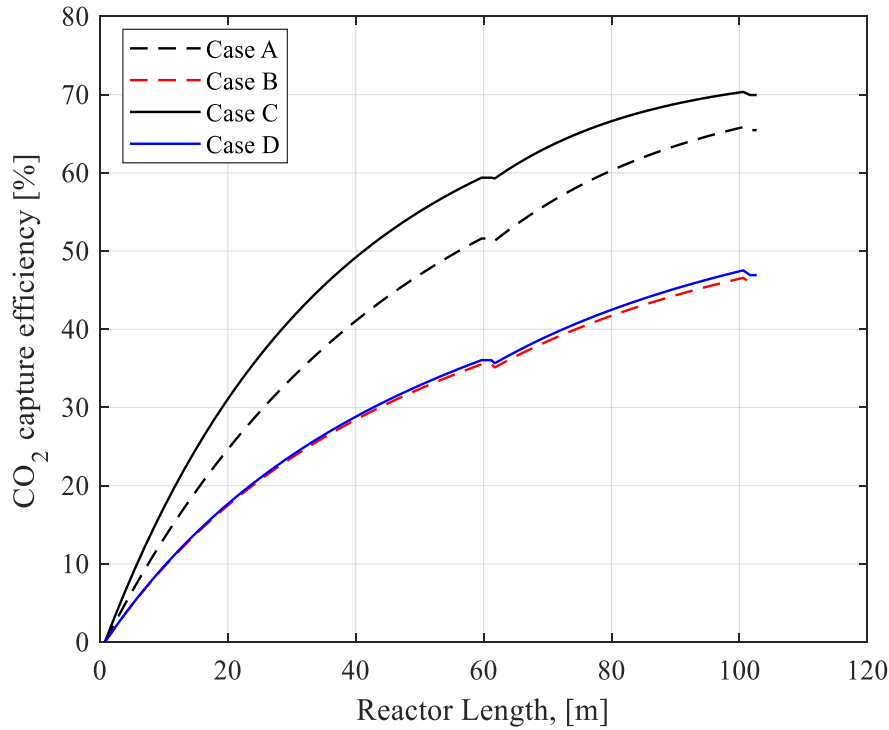


Figure 6.22. CO₂ capture efficiency in all four cases across the length of the carbonator reactor.

From the values and variables displayed in Figure 6.20 and Table 6.6, it can be analyzed and observed that the maximum CO₂ capture efficiency was achieved at case C, where the sorbent capacity (X_{max}) was at 40 [%] and the solid circulation back to carbonator at 20 [%] with slight higher combustion at the second feed. First, the high sorbent capacity showed higher capture efficiencies, which indicates the significance of maintaining active sorbent existing in the reactor, by constantly introducing fresh limestone in the system. Secondly, as the recirculation of solids increased the efficiency decreased. This mainly occurred because of the higher existence of carbonated solids in the reactor inlet, which results in lower quantity of active calcium oxide able to absorb CO₂ under the carbonation reaction boundaries. For further theoretical explanation upon the raw material behavior under calcination-carbonation reactions loop, one can see chapter 2.2. Concluding, the extra fuel feed at the secondary point favored the CaL process, although the technoeconomical prospective must be further evaluated.

7. DISCUSSION

The objective of this report was to build a 1D case model for the CLEANER-process, which included carbon capture by utilizing the calcium looping process. The model was aimed to have interconnected calciner and carbonator reactors, where the solids can flow between them in dynamic balance. Furthermore, the main study was to evaluate and demonstrate accurate CO₂, CaCO₃ and CaO concentration profiles across the length of the reactor and to determine whether or not the pneumatic transport and entrainment of solids is maintained in the reactors, by calculating the choking velocity.

The 1D model showed satisfying accuracy compared with previous values from works done for the CLEANER-process, as shown in chapter 6.1 where the model verification was implemented. The desired accuracy not only proved that the CO₂, CaCO₃, CaO, carbonation rate and calcination rate profiles are trusty, but as well that the 1D model modified and updated can successfully simulate the pneumatic transport regime and the desired dynamic solid exchange between the interconnected reactors. However, the CO₂ capture efficiency was slightly off compared to the D2.3 because of the selected model parameters needed to accurate represent the boundary conditions (mass flow rate, make up flow, etc.).

The CO₂ concentration profiles (Figure 6.12) in the carbonator, showed a CO₂ vol [%] of 19.8 % at the inlet and a CO₂ vol [%] of 7.2 % at the outlet, which difference indicated that the carbonation reaction (Table 5.1) effectively utilized across the reactor length. Furthermore, as expected the CaCO₃ mass [%] at the inlet increased from 14.4 % to 22 %, as the CaO absorbed the carbon dioxide in the carbonator. In the calciner as showed in Figure 6.13, the CO₂ vol [%] of 56.5 % in the reactor inlet, increased until 63.8 % at the outlet, which shows the effectiveness of the calcination reaction across the length of the reactor, with decreased CaCO₃ mass [%] of 39.7 % in the inlet until 12.1 % in the outlet.

From the calcination and carbonation reaction rate (Table 5.1) profiles, the importance of the temperature and concentration of CaCO₃ and CO₂ at the point was analyzed. In the carbonation reaction profile, the increase in the CaCO₃ solids and decrease of CO₂ across the length, contributed with gradual effectiveness decrease of the carbonation

reaction as shown in Figure 6.5. In addition, the expansion of the inner diameter after the gooseneck further decreased the reaction rate as the solids concentration per m³ decreased. Furthermore, in the calcination reaction profile as shown in Figure 6.6 , the abrupt temperature increase in the bottom of the riser together with the large CaCO₃ concentration at the site, contributed with large calcination reaction rates at the inlet of the calciner and gradual decrease of it across the length, as the endothermic reaction reduces the temperature.

During simulations, results of the pilot plant with false air introduction at the end of the carbonator and without air leakage, were taken and further evaluated. The results displayed slight reduction of the temperature, while the pilot plant operated with air leakage, due to the cold income flow of 25 °C. In addition, the excess O₂ and N₂ concentration of the incoming air, negatively contributed to the volumetric percentage concentration of CO₂, and slight decline of the overall CO₂ capture efficiency was indicated.

The fluidizing gas velocity in the carbonator riser showed a constant value of 16 m/s across the length of it. However, after the gooseneck bend the velocity decreases at 9.1 m/s due to the expansion of the inner diameter of the reactor from 0.264 [m] to 0.346 [m]. The velocity reduction in general can be caused due to the pressure increase in the carbonators downcomer, change in the total molar mass of the gas, change in mass flow rate or change in temperature. Although, in the specific case the cross-sectional area variation before and after the gooseneck bend was the main reason why the velocity dropped. Furthermore, the fluidizing gas velocity at calciner was evaluated at 9.0 m/s in the calciner inlet with sharply increase at 11.3 m/s after the first 3 to 5 meters, which value remained almost constant until the end of the reactor. In consequence, after the fluidizing gas velocity calculations in both reactors, the choking type ‘A’ accumulation velocity evaluation across the length of the reactors, showed that the pneumatic transport regime will safely be maintained.

Finally, after demonstration and comparison of the four different cases evaluated in the process. The CO₂ capture efficiency at the case C showed the largest number. The main reasons were the sorbent capacity which evaluated at 40 [%] and the lower solid internal recirculation of carbonated material back in the reactor’s inlet.

8. CONCLUSION

This work was done under the LUT University for the CLEANER project. The main objective of the work was to build a 1D-Model simulating the entrained flow in the pneumatic transport regime under the calcium looping process with two interconnected reactors dynamically exchanging solids. In addition, the model aimed to accurately predict the CO₂ and CaCO₃ profiles across the length of the reactors and determine whether or not the choking velocity allows the constant operation of the reactors in pneumatic transport regime.

Literature review of chapter 2,3 and 4 was finally utilized to modify and update the 1D model handled from previous J. Ylätalo (2014) and S. Sepponen (2017) works. Pneumatic transport, entrainment of the solids in the specific regime and representation of the unique gooseneck design configuration of the Vernasca pilot plant (Figure 5.1) were the main modelling targets, together with the simulation of accurate CO₂, CaO and CaCO₃ profiles and the choking velocity ‘checking’, which were all successfully achieved.

The 1D-Model resulted to satisfying agreement with previous works done for the same configuration. In addition, the sorbent capacity and solid internal recirculation back to carbonator were proven of main importance regarding the efficiency of the pilot plant and in general for the CaL process. Concluding, studies were made in the expected air leak at the end of the carbonator, which resulted to slight reduction of the overall efficiency of the system and reduction of the operational temperature at the carbonator.

Finally, extra fuel feed at the secondary point was proven to slightly increase the carbon dioxide capture efficiency. However, further and future works and studies are needed to evaluate and analyze it from the technoeconomical prospective.

REFERENCES

- Arundel, P., Bibb, S. and Boothroyd, R. (1971). Dispersed density distribution and extent of agglomeration in a polydisperse fine particle suspension flowing turbulently upwards in a duet. *Powder Technology*, 4(6), pp.302-312.
- Alonso, M., Rodríguez, N., González, B., Grasa, G., Murillo, R. and Abanades, J. (2010). Carbon dioxide capture from combustion flue gases with a calcium oxide chemical loop. Experimental results and process development. *International Journal of Greenhouse Gas Control*, 4(2), pp.167-173.
- Alonso, M., Rodríguez, N., Grasa, G. and Abanades, J. (2009). Modelling of a fluidized bed carbonator reactor to capture CO₂ from a combustion flue gas. *Chemical Engineering Science*, 64(5), pp.883-891.
- Avidan, A. and Yerushalmi, J. (1982). Bed expansion in high velocity fluidization. *Powder Technology*, 32(2), pp.223-232.
- Bai, D.; Issangya, A. S.; Grace, J. R. A Novel Method for Determination of Choking Velocities. *Powder Technol.* 1998, 97, 95.
- Basu, P. and Fraser, S. (1991). *Circulating fluidized bed boilers*. Boston: Butterworth-Heinemann.
- Bhatia, S.K., Perlmutter, D.D., 1983. Effect of the product layer on the kinetics of the CO₂-lime reaction. *AIChE Journal* 29, 79-86.
- Bi, H. T.; Grace, J. R.; Zhu, J. X. Types of Choking in Vertical Pneumatic Systems. *Int. J. Multiphase Flow* 1993, 19 (6), 1077.
- Bi, H. T.; Fan, L. S. Regime Transition in Gas-Solid Circulating Fluidized Beds. *AIChE Annual Meeing*, Los Angeles, Nov 17-22, 1991; Paper 101e.
- Crowe, C. T. (2006). *Multiphase flow handbook*. Boca Raton, FL, CRC Press.
- De-Souza Santos, M. (2010). *Solid fuels combustion and gasification*. CRC Press. ISBN 9781420047493.
- D. Geldart, (1986), *Gas Fluidization Technology*. Great Britain. John Wiley & Sons.
- Fang, F., Li, Z.-S., and Cai, N.-S. (2009). Experiment and modeling of CO₂ capture from flue gases at high temperature in a fluidized bed reactor with Ca-based sorbents. *Energy & Fuels*, 23, pp. 207-216.
- Freeman, B., Hao, P., Baker, R., Kniep, J., Chen, E., Ding, J., Zhang, Y. and Rochelle, G. (2014). Hybrid Membrane-absorption CO₂ Capture Process. *Energy Procedia*, 63, pp.605-613.
- F.A. Zenz and D.F. Othmer, *Fluidization*, Van Nostrand Reinhold, New York, 1956.

Gómez-Barea, A. and Leckner, B. (2010) 'Modeling of biomass gasification in fluidized bed', *Progress in Energy and Combustion Science*, 36(4), pp. 444–509. doi: 10.1016/j.pecs.2009.12.002.

Grasa, G. and Abanades, J. (2006). CO₂Capture Capacity of CaO in Long Series of Carbonation/Calcination Cycles. *Industrial & Engineering Chemistry Research*, 45(26), pp.8846-8851.

Grasa, G., Alonso, M. and Abanades, J. (2008b). Sulfation of CaO Particles in a Carbonation/Calcination Loop to Capture CO₂. *Industrial & Engineering Chemistry Research*, 47(5), pp.1630-1635.

Johne, R. (1966). Einfluß der Konzentration einer monodispersen Suspension auf die Sinkgeschwindigkeit ihrer Teilchen. *Chemie Ingenieur Technik - CIT*, 38(4), pp.428-430.

Koglin, B. (1971). Statistische Verteilung der Sedimentationsgeschwindigkeit in niedrig konzentrierten Suspensionen. *Chemie Ingenieur Technik - CIT*, 43(13), pp.761-764.

Klinzing, G., Rizk, F., Marcus, R. and Leung, L. (2010). *Pneumatic Conveying of Solids*. Dordrecht: Springer Science+Business Media B.V.

Kunii, D. and Levenspiel, O. (1991). *Fluidization engineering*. Boston: Butterworth-Heinemann.

Li Y. and M. Kwauk, in *Fluidization III*, J.R. Grace and J. Matsen, eds., p. 537, Plenum, New York, 1980.

Markewitz P., Bongartz R. (2015) Carbon Capture Technologies. In: Kuckshinrichs W., Hake JF. (eds) Carbon Capture, Storage and Use. Springer, Cham. doi: https://doi.org/10.1007/978-3-319-11943-4_2

Matsen, J. (1982). Mechanisms of choking and entrainment. *Powder Technology*, 32(1), pp.21-33.

Matteo R., et al. (2018). *Heat and mass balances of the demonstration plant under relevant operating conditions to support the design of the demonstration plant*. WP2-Deliverable D2.3.

Myöhänen, K. and Hyppänen, T. (2011). A Three-Dimensional Model Frame for Modelling Combustion and Gasification in Circulating Fluidized Bed Furnaces. *International Journal of Chemical Reactor Engineering*, 9(1).

Myöhänen, K. (2011). *Modelling of Combustion and Sorbent Reactions in Three-Dimensional Flow Environment of a Circulating Fluidized Bed Furnace*. LUT PhD Dissertation. [Online] Available at : <http://lutpub.lut.fi/handle/10024/72463>, pp. 65-108.

Pfeifer, C. (2013) 'Sorbent-enhanced gasification', in *Fluidized bed technologies for near-zero emission combustion and gasification*. Woodhead Publishing, pp. 971–1001. doi: 10.1533/9780857098801.4.971.

- Punwani, D.V., Modi, M.V., Tarman, P.B., 1976. Generalized correlation for estimating choking velocity in vertical solids tranport, in: International Powder and Bulk Solids Handling and Processing Conference. Chicago.
- Rautiainen, A., Stewart, G., Poikolainen, V. and Sarkomaa, P. (1999). An experimental study of vertical pneumatic conveying. *Powder Technology*, 104(2), pp.139-150.
- Romano, M. (2012). Modeling the carbonator of a Ca-looping process for CO₂ capture from power plant flue gas. *Chemical Engineering Science*, 69(1), pp.257-269.
- Sánchez-Biezma, A., Paniagua, J., Diaz, L., Lorenzo, M., Alvarez, J., Martínez, D., Arias, B., Diego, M.E., and Abanades, J.C. (2013). Testing postcombustion CO₂ capture with CaO in a 1.7 MWt pilot faciltiy. *Energy Procedia*, 37, pp. 1-8.
- Sankar, S. and Smith, T. (1986). Slip velocities in pneumatic transport part I. *Powder Technology*, 47(2), pp.167-177.
- Sankar, S. and Smith, T. (1986). Slip velocities in pneumatic transport part II. *Powder Technology*, 47(2), pp.179-194.
- Soo, S., Trezek, G., Dimick, R. and Hohnstreiter, G. (1964). Concentration and Mass Flow Distrbutions in a Gas-Solid Suspension. *Industrial & Engineering Chemistry Fundamentals*, 3(2), pp.98-106.
- Sepponen, S. (2017). A Development and Application of a One-Dimensional Model for a Sorbent-Enhanced CFB Gasifier. LUT Master's Thesis. [Online]. Available at : <http://lutpub.lut.fi/handle/10024/144109>
- Silcox, G., Kramlich, J., and Pershing, W. (1989). A mathematical model for the flash calcination of dispersed CaCO₃ and Ca (OH)₂ particles. *Industrial & Engineering Chemistry Research*, 28, pp. 155-160.
- Spinelli, M., Martínez, I. and Romano, M. (2018). One-dimensional model of entrained-flow carbonator for CO₂ capture in cement kilns by Calcium looping process. *Chemical Engineering Science*, 191, pp.100-114.
- Shimizu, T., Hirama, T., Hosoda, H., Kitano, K., Inagaki, M. and Tejima, K. (1999). A Twin Fluid-Bed Reactor for Removal of CO₂ from Combustion Processes. *Chemical Engineering Research and Design*, 77(1), pp.62-68.
- Valverde, J. (2013). Ca-based synthetic materials with enhanced CO₂capture efficiency. *J. Mater. Chem. A*, 1(3), pp.447-468.
- Wang, J. and Anthony, E. (2005). On the Decay Behavior of the CO₂Absorption Capacity of CaO-Based Sorbents. *Industrial & Engineering Chemistry Research*, 44(3), pp.627-629.
- Wen, C. and Hashinger, R. (1960). Elutriation of solid particles from a dense-phase fluidized bed. *AIChE Journal*, 6(2), pp.220-226.

Xu, G., Nomura, K., Gao, S., Kato, K., 2001. More fundamentals of dilute suspension collapse and choking for vertical conveying systems. *AIChE J.* 47, 2177–2196. doi:10.1002/aic.690471006

Yang, W. C. Criteria for Choking in Vertical Pneumatic Conveying Lines. *Powder Technol.* 1983, 35, 143.

Yang, W. C. Incipient Fast Fluidization Boundary and Operational Map for Circulating Fluidized Bed Systems. In *Circulating Fluidized Bed Technology IV*; Avidan, A. A., Ed.; *AIChE*: New York, 1993; p 62.

Yang, W.C., 2004. “Choking” revisited. *Ind. Eng. Chem. Res.* 43, 5496–5506. doi:10.1021/ie0307479

Yerushalmi, J. and Cankurt, N. (1979). Further studies of the regimes of fluidization. *Powder Technology*, 24(2), pp.187-205.

Yerushalmi, J., Turner, D. and Squires, A. (1976). The Fast-Fluidized Bed. *Industrial & Engineering Chemistry Process Design and Development*, 15(1), pp.47-53.

Yerushalmi, J., and N.T. Cankurt. High velocity fluidized beds *Chemtech*, 8, 564 (1978).

Yousfi, Y.; Gau, G. Aerodynamics of the Vertical Flow of Concentrated Gas-Solid Suspensions. Flow Regimes and Aerodynamic Stability. *Chem. Eng. Sci.* 1974, 29, 1939 (in French).

Ylätalo, J., Parkkinen, J., Ritvanen, J., Tynjälä, T. and Hyppänen, T. (2013). Modeling of the oxy-combustion calciner in the post-combustion calcium looping process. *Fuel*, 113, pp.770-779.

Ylätalo, J., Ritvanen, J., Arias, B., Tynjälä, T. and Hyppänen, T. (2012). 1-Dimensional modelling and simulation of the calcium looping process. *International Journal of Greenhouse Gas Control*, 9, pp.130-135.

Ylätalo, J., Ritvanen, J., Tynjälä, T. and Hyppänen, T. (2014). Model based scale-up study of the calcium looping process. *Fuel*, 115, pp.329-337.

Ylätalo, J. (2013) *Model Based Analysis of the Post- Combustion Calcium Looping Process for Carbon Dioxide Capture*. LUT PhD Dissertation [Online] Available at: <http://lutpub.lut.fi/handle/10024/93929>.

Zhao, L., Menzer, R., Riensche, E., Blum, L. and Stolten, D. (2009). Concepts and investment cost analyses of multi-stage membrane systems used in post-combustion processes. *Energy Procedia*, 1(1), pp.269-278.

Zenker, P.: Staub-Reinhalt, Luft 32, 1 (1972)

Zheng, L., (2011). *Oxy-fuel Combustion for Power Generation and Carbon Dioxide (CO₂) capture*. Woodhead Publishing Series in Energy: Number 17. page 1.